

## Patient-Specific Cardiovascular Flows Using Particle Image-Based Velocimetry

Wu, X.

**DOI**

[10.4233/uuid:0b338c84-db73-4dc2-8622-a111735ef33a](https://doi.org/10.4233/uuid:0b338c84-db73-4dc2-8622-a111735ef33a)

**Publication date**

2024

**Document Version**

Final published version

**Citation (APA)**

Wu, X. (2024). *Patient-Specific Cardiovascular Flows Using Particle Image-Based Velocimetry*. [Dissertation (TU Delft), Delft University of Technology]. <https://doi.org/10.4233/uuid:0b338c84-db73-4dc2-8622-a111735ef33a>

**Important note**

To cite this publication, please use the final published version (if applicable). Please check the document version above.

**Copyright**

Other than for strictly personal use, it is not permitted to download, forward or distribute the text or part of it, without the consent of the author(s) and/or copyright holder(s), unless the work is under an open content license such as Creative Commons.

**Takedown policy**

Please contact us and provide details if you believe this document breaches copyrights. We will remove access to the work immediately and investigate your claim.

# **PATIENT-SPECIFIC CARDIOVASCULAR FLOWS**

USING PARTICLE IMAGE-BASED VELOCIMETRY



**PATIENT-SPECIFIC CARDIOVASCULAR FLOWS**  
USING PARTICLE IMAGE-BASED VELOCIMETRY

**Dissertation**

for the purpose of obtaining the degree of doctor  
at Delft University of Technology,  
by the authority of the Rector Magnificus Prof. dr. ir. T.H.J.J. van der Hagen,  
chair of the Board of Doctorates,  
to be defended publicly  
on Monday 23 September, 2024 at 15.00 hours

by

**Xiaolin Wu**

Master of Science in Safety Engineering,  
Dalian University of Technology, Dalian, China,  
born in Hunan, China.

This dissertation has been approved by the promotors

Composition of the doctoral committee:

Rector Magnificus,	chairperson
Prof. Dr. Dipl.-Ing. S. Kenjereš,	Delft University of Technology, Promotor
Prof. Dr. H. J. Lamb, MD,	Leiden University Medical Center, Promotor

*Independent members:*

Prof. Dr. B. Rieger,	Delft University of Technology
Prof. Dr. Ir. P. Segers,	Ghent University, Belgium
Dr. S. Celi,	FTGM/University of Pisa, Italy
Dr. N. Bhattacharya,	Delft University of Technology

*Reserve members:*

Prof. Dr. Ir. R. van Ommen,	Delft University of Technology
-----------------------------	--------------------------------



*Keywords:* In vitro experiments, Particle Image Velocimetry, Lagrangian Particle Tracking, Intracranial aneurysm, Left ventricle, Aorta

*Printed by:* Ridderprint

*Front & Back:* Visualization of the particle tracks in a patient-specific thoracic aorta

Copyright © 2024 by X. Wu

ISBN 978-94-6506-369-0

An electronic version of this dissertation is available at  
<http://repository.tudelft.nl/>.

# CONTENTS

<b>Summary</b>	<b>ix</b>
<b>Samenvatting</b>	<b>x</b>
<b>1 Introduction</b>	<b>1</b>
1.1 Cardiovascular System . . . . .	1
1.2 Cardiovascular Diseases and Hemodynamics . . . . .	1
1.2.1 Hemodynamics and Atherosclerosis . . . . .	2
1.2.2 Hemodynamics and Aneurysms . . . . .	2
1.2.3 Hemodynamics and Heart Dysfunction . . . . .	3
1.3 Blood Flow Measurement . . . . .	3
1.3.1 Clinical Flow Assessment . . . . .	3
1.3.2 Computational Fluid Dynamics (CFD) . . . . .	4
1.3.3 <i>In vitro</i> Particle Image-based Experiments . . . . .	5
1.4 Particle Image-based Velocimetry . . . . .	6
1.4.1 Particle Image Velocimetry . . . . .	6
1.4.2 Lagrangian Particle Tracking . . . . .	10
1.4.3 Comparison of the Particle Image-based Techniques . . . . .	13
1.5 Objective and Outline . . . . .	15
1.5.1 Objective . . . . .	15
1.5.2 Outline . . . . .	15
<b>2 Multimodality Study of a Patient-specific Intracranial Aneurysm</b>	<b>19</b>
2.1 Introduction . . . . .	21
2.2 Methods . . . . .	22
2.2.1 PC-MRI Setup . . . . .	22
2.2.2 Preparations for <i>In vitro</i> and <i>In silico</i> Models . . . . .	22
2.2.3 PIV Setup . . . . .	23
2.2.4 CFD Simulations . . . . .	26
2.2.5 Calculation of Wall Shear Stress . . . . .	26
2.3 Results . . . . .	27
2.3.1 Comparison of Flow Patterns . . . . .	27
2.3.2 Comparison of Velocity Field . . . . .	27
2.3.3 Comparison of Vorticity . . . . .	29
2.3.4 Comparison of Wall Shear Stress . . . . .	32
2.4 Discussion . . . . .	33
2.5 Conclusion . . . . .	35

<b>3</b>	<b>Shake-the-Box in a Left Ventricle Model</b>	<b>45</b>
3.1	Introduction . . . . .	47
3.2	Methods . . . . .	48
3.2.1	Experimental Setup . . . . .	48
3.2.2	Data Acquisition and Shake-the-Box Analysis . . . . .	49
3.2.3	Instantaneous Pressure Field. . . . .	50
3.2.4	3D POD Analysis. . . . .	51
3.3	Results and Discussion . . . . .	52
3.3.1	General Intraventricular Flow Features . . . . .	52
3.3.2	4D Relative Pressure Field . . . . .	52
3.3.3	POD Analysis . . . . .	55
3.3.4	Energy Contribution of POD Modes . . . . .	57
3.3.5	Limitations. . . . .	58
3.4	Conclusions. . . . .	58
<b>4</b>	<b>Wall Deformation and Flow Analysis in a Patient-specific Compliant Aorta Model</b>	<b>67</b>
4.1	Introduction . . . . .	69
4.2	Material and Methods. . . . .	70
4.2.1	Compliant Aorta Model . . . . .	70
4.2.2	Experimental Setup . . . . .	71
4.2.3	Data Acquisition and Shake-the-Box Analysis . . . . .	72
4.2.4	Post-processing . . . . .	73
4.3	Results . . . . .	74
4.3.1	Particle Tracks . . . . .	74
4.3.2	Aortic Wall Deformation . . . . .	74
4.3.3	Flow Patterns . . . . .	75
4.3.4	WSS, TAWSS, and OSI . . . . .	76
4.3.5	Comparison with 4D-Flow MRI . . . . .	76
4.4	Discussion . . . . .	77
4.4.1	Aortic Strain and Distensibility. . . . .	78
4.4.2	Flow Patterns and WSS Distribution . . . . .	78
4.4.3	Agreement Between <i>In vitro</i> and <i>In vivo</i> Data . . . . .	78
4.4.4	Limitations. . . . .	79
4.5	Conclusions. . . . .	79
<b>5</b>	<b>Conclusions and Outlook</b>	<b>93</b>
5.1	Conclusions. . . . .	93
5.2	Future Opportunities . . . . .	96
5.2.1	Non-Newtonian Blood Analogues for <i>In vitro</i> Blood Flow Modeling. . . . .	96
5.2.2	Apply POD in Multimodality Study, New Biomarkers Development, and Reduced Order Modeling. . . . .	96
5.2.3	Application of <i>In vitro</i> Compliant Arterial Modeling . . . . .	97
5.2.4	Machine Learning for Blood Flow Modeling . . . . .	97
5.3	Outlook . . . . .	98

---

<b>Acknowledgements</b>	<b>101</b>
<b>Curriculum Vitæ</b>	<b>103</b>
<b>List of Publications</b>	<b>105</b>



# SUMMARY

Cardiovascular diseases (CVDs) are a leading cause of death worldwide. To prevent sudden lethal cardiovascular events, early diagnosis and treatment are crucial. Hemodynamics play a key role in both the development and the management of cardiovascular diseases. In recent decades, physicians and engineers have been working together to understand the interplay between blood flow and various cardiovascular conditions, and to develop flow-based parameters as new biomarkers for clinical guidelines.

Visualizing and quantifying blood flow in opaque moving cavities are challenging. Current *in vivo* medical imaging techniques, such as 4D-Flow magnetic resonance imaging (4D-Flow MRI), are able to provide non-invasive blood flow information in 3D space and time. However, their accuracy is affected by limited spatial and temporal resolutions. Engineering techniques, i.e., computational fluid dynamics (CFD) simulations and *in vitro* optical flow measurements using particle image-based techniques, can offer high spatiotemporal resolution flow information but require improved fidelity to accurately represent the complexities of physiological blood flow for patient-specific treatment.

In the past decades, *in vitro* optical flow measurements were conducted based on simplifications, such as general geometries, steady flow conditions, and rigid walls. To enhance fidelity, *in vitro* system must mimic the physiological conditions as closely as possible. Moreover, *in vitro* optical flow measurements primarily used the 2D technique – planar particle image velocimetry (PIV) and pseudo-3D technique – multiplane Stereoscopic PIV (Stereo-PIV) which resolves the 3D velocity field from a series of 2D planar measurements. Given the inherent 3D nature of cardiovascular flows, using advanced volumetric techniques to obtain highly-resolved 3D velocity fields (often called 4D), is highly beneficial.

In this thesis, we first confirmed the superiority of the volumetric technique over 2D and pseudo-3D techniques in *in vitro* hemodynamic studies by conducting both Tomographic PIV (Tomo-PIV) and multiplane Stereo-PIV measurements on a patient-specific intracranial aneurysm. The obtained flow patterns, velocity, and flow-derived parameters such as vorticity and wall shear stress (WSS) were compared to *in vivo* 4D-Flow MRI and CFD simulation. The comparative results showed that despite having twice the in-plane resolution of Tomo-PIV, the multiplane Stereo-PIV underpredicted the WSS due to its four times lower spatial resolution in the depth direction compared to Tomo-PIV. The voxel sizes in the depth dimension for multiplane Stereo-PIV measurements are limited by the laser sheet thickness (1 mm), resulting in a significant smoothing effect on the velocity gradients and, consequently, WSS.

Next, we applied advanced 4D particle tracking velocimetry (PTV) technique – Shake-the-Box (STB) to the hemodynamic study. Compared to Tomo-PIV, STB has the advantages of resolving fewer ghost particles in the reconstruction, higher positional accuracy, higher spatial resolution with the same seeding density, and less computational time. The STB was performed on a realistic-shaped, compliant left ventricle (LV) phantom with bio-

logical valves. Particle tracks, 4D velocity, and pressure field were resolved. We then conducted a Proper Orthogonal Decomposition (POD) flow analysis based on the obtained velocity field. The STB-resolved flow pattern, velocity, and pressure were validated to those *in vivo* MRI studies in the literature. To our knowledge, this is the first work that provides cardiovascular flow investigation based on STB measurements. Moreover, we demonstrated the potential of POD as an alternative approach to efficiently visualize and analyze the various scale flow structures and their temporal behaviors in the cardiovascular system.

Finally, we put our focus on improving the bio-fidelity of *in vitro* modeling. We manufactured a patient-specific, compliant, and low-cost aorta phantom for *in vitro* optical flow measurement use. By incorporating a physiological flow-providing system and the STB technique, we assessed the aortic wall movements and aortic hemodynamics. The compliant aorta exhibited distensibility and cyclic strain that were within the reported physiological values in the literature. Flow patterns and wall shear stress (WSS) qualitatively also matched with *in vivo* 4D-Flow MRI measurements and similar reported cases in the literature. In summary, this work improved *in vitro* blood flow modeling fidelity by developing a compliant patient-specific artery phantom with physiological wall properties, demonstrating its successful application in particle image-based volumetric flow measurements. This contributes to the availability of high-fidelity experimental cardiovascular flow data for hemodynamic studies as well as for validating medical techniques and computational modeling.

The dissertation ends with a concluding chapter where we highlighted the important findings and the perspective for future works.

# SAMENVATTING

Cardiovasculaire ziekten (CZ) zijn wereldwijd een belangrijke doodsoorzaak. Een vroege diagnose en behandeling zijn cruciaal om plotselinge en dodelijke cardiovasculaire gebeurtenissen te voorkomen. Hemodynamiek speelt een sleutelrol bij zowel de ontwikkeling als het beheren van cardiovasculaire aandoeningen. In de afgelopen decennia werkten artsen en ingenieurs samen om de wisselwerking tussen bloedstroom en verschillende cardiovasculaire aandoeningen te begrijpen, en om op vloeistof stroom gebaseerde parameters te ontwikkelen als nieuwe biomarkers voor klinische richtlijnen.

Het visualiseren en kwantificeren van bloedstroom in doorzichtige bewegende holtes is uitdagend. Huidige *in vivo* beeldvormingstechnieken, zoals 4D-Flow magnetische resonantie beeldvorming (4D-Flow MRI), kunnen niet-invasieve bloedstroominformatie in 3D-ruimte en tijd verschaffen. Hun nauwkeurigheid wordt echter beïnvloed door beperkte resolutie in de ruimte en de tijd. Ingenieurs technieken, zoals computational fluid dynamics (CFD) simulaties en *in vitro* experimenten met op deeltjes gebaseerde technieken, kunnen bloedstroominformatie met een hoge ruimtelijke en temporele resolutie bieden, maar vereisen een verbeterde betrouwbaarheid om de complexiteiten van fysiologische bloedstroom voor patiëntspecifieke behandeling nauwkeurig te vertegenwoordigen.

In de afgelopen decennia werden *in vitro* optische bloedstroommetingen uitgevoerd op basis van vereenvoudigingen, zoals algemene geometrie, constante stroom en stijve wanden. Om de nauwkeurigheid te verbeteren, moeten *in vitro* systemen de fysiologische omstandigheden zo nauwkeurig mogelijk nabootsen. Bovendien gebruikten *in vitro* bloedstroommetingen voornamelijk de 2D-techniek - planaire deeltjesbeeldsnelheidsmeting (PIV) en pseudo-3D-techniek - multiplane Stereoscopische PIV (Stereo-PIV) die het 3D-snelheidsveld oplost van een reeks 2D-planaire metingen. Gezien de inherente 3D-aard van cardiovasculaire stromingen, is het zeer voordelig om geavanceerde volumetrische technieken te gebruiken om 3D-snelheidsvelden (vaak 4D genoemd) met een hoge resolutie te verkrijgen.

In deze scriptie hebben we eerst de superioriteit van de volumetrische techniek ten opzichte van de 2D- of pseudo-3D-techniek bevestigd in *in vitro* hemodynamische studies door zowel Tomografische PIV (Tomo-PIV) als multiplane Stereo-PIV metingen uit te voeren op een intracranieële aneurysma dat specifiek is voor de patiënt. De verkregen stromingspatronen, snelheid en stromingsafgeleide parameters zoals vorticeiteit en wand-schuifspanning (WSS) werden vergeleken met *in vivo* 4D-Flow MRI en CFD-simulatie. De vergelijkende resultaten toonden aan dat de multiplane Stereo-PIV de WSS onderschatte vanwege de lagere ruimtelijke resolutie in de dieptedimensie in vergelijking met Tomo-PIV. De voxelformaten in de dieptedimensie voor multiplane Stereo-PIV metingen worden beperkt door de dikte van het laserscherm (1 mm), wat resulteert in een significant afvallend effect op de snelheidsgradiënten en, bijgevolg, de WSS.

Vervolgens pasten we de geavanceerde 4D-deeltjesvolgsnelheidsmetingstechniek -

Shake-the-Box (STB) toe op de hemodynamische studie. Vergeleken met Tomo-PIV heeft STB de voordelen van het oplossen van minder spookdeeltjes in de reconstructie, hogere positionele nauwkeurigheid, hogere ruimtelijke resolutie met dezelfde zaaddichtheid en minder rekenkundige tijd. De STB werd uitgevoerd op een realistisch gevormde, flexibele linker ventrikel (LV) fantoom met biologische kleppen. Deeltjessporen, 4D-snelheid en drukveld werden opgelost. Vervolgens voerden we een POD-stroomanalyse uit op basis van het verkregen snelheidsveld. Het STB-opgeloste stroompatroon, snelheid en druk werden gevalideerd met die in *in vivo* MRI-studies in de literatuur. Naar ons beste weten is dit het eerste werk dat cardiovasculaire stroomonderzoeken levert op basis van STB-metingen. Bovendien hebben we het potentieel van POD gedemonstreerd als een alternatieve benadering om op efficiënte wijze de verschillende schaalstroomstructuren en hun tijdsafhankelijke gedragingen in het cardiovasculaire systeem te visualiseren en analyseren.

Tot slot hebben we onze focus gericht op het verbeteren van de bio-betrouwbaarheid van *in vitro* modellering. We hebben een patiëntspecifiek, flexibel en goedkoop aortafantom vervaardigd voor gebruik bij *in vitro* optische stroommetingen. Door een fysiologisch stroomvoorzieningssysteem en de STB-techniek te incorporeren, hebben we de bewegingen van de aortawand en de aortahemodynamica beoordeeld. De flexibele aorta vertoonde distensibiliteit en cyclische belasting die binnen de gerapporteerde fysiologische waarden in de literatuur vielen. Stroompatronen en wandschuifspanning (WSS) kwamen ook kwalitatief overeen met *in vivo* 4D-Flow MRI-metingen en vergelijkbare gerapporteerde gevallen in de literatuur. Kortom, dit werk verbeterde de biofideliteit van *in vitro* bloedstroomodellering door de ontwikkeling van een flexibel patiëntspecifiek arterieel fantoom met fysiologische wandkenmerken, waarbij de succesvolle toepassing ervan werd gedemonstreerd in op deeltjes gebaseerde volumetrische stroommetingen. Dit draagt bij aan de beschikbaarheid van experimentele cardiovasculaire stroomgegevens met een hoge nauwkeurigheid voor hemodynamische studies, evenals voor het valideren van medische technieken en computationele modellering.

De dissertatie eindigt met een afsluitend hoofdstuk waarin we de belangrijkste bevindingen en het perspectief voor toekomstig werk benadrukken.

# 1

## INTRODUCTION

### 1.1. CARDIOVASCULAR SYSTEM

The human cardiovascular system is a closed circulatory system that transports important substances such as nutrients, oxygen, and metabolic wastes to the entire body [1]. It consists of a central organ, the heart, along with blood and multiscale vascular networks. Oxygenated blood is pumped by the left ventricle into big arteries, which branch and break into smaller arteries – arterioles, and further into the capillary bed where nutrients and oxygen are exchanged. Deoxygenated blood is then drained from capillaries into venules, veins, and eventually returned to the right heart. Subsequently, the right ventricle pumps the oxygen-deprived blood to the pulmonary artery and to the lung capillaries for absorbing new oxygen.

### 1.2. CARDIOVASCULAR DISEASES AND HEMODYNAMICS

Many people develop diseases in their heart or blood vessels, namely the cardiovascular diseases (CVDs). According to the World Health Organization (WHO) report in 2019, 1/3 of the world's deaths were caused by CVDs [2]. Early diagnosis and treatment of CVDs have become major goals to prevent its epidemic progression. Over the past 20 years, a new research perspective on CVDs has emerged, known as hemodynamics (fluid mechanics of blood flow). Strong association between hemodynamics and CVDs was found: sustained changes of the local hemodynamic environment can stimulate local vessel wall restructuring, leading to atherosclerosis, aneurysm formation and dissections; Abnormal vessel morphologies, in turn, can alter the local blood flow and hemodynamic forces on the arterial wall.

Blood flow regulates the vascular structural remodeling through its interaction with the endothelium. Wall shear stress (WSS) is the tangential force that blood flow exerts on the arterial wall per unit area. Endothelium, the first part of the inner layer of arterial walls, can respond rapidly and sensitively to flow-induced mechanical stimulus, triggering biochemical responses known as mechanotransduction [3]. A certain level of WSS (1~2 Pa) is normal in arteries [4]. Higher or lower WSS can potentially trigger pathologic

responses and aberrant functions of endothelial cells, including endothelium-mediated proinflammatory responses, matrix metalloproteinase activation, cell death, extracellular matrix (ECM) degradation, and vascular remodeling [5].

### 1.2.1. HEMODYNAMICS AND ATHEROSCLEROSIS

Presently, it is well known that low WSS but high oscillatory shear stress flow is linked to a predisposition of atherosclerosis [6]. This characteristic flow disturbance is typical observed at arterial branches, bifurcations, and curvatures, where oscillating vortices are formed due to flow separations, Fig. 1.1. Common sites are the carotid bifurcation and aortic arch. The atherosclerotic lesion can also induce local disturbed flow conditions (low and oscillatory shear stress), which further promotes the growth of atherosclerosis [3]. In contrast, high shear stress, unidirectional and laminar flow regions are atherosclerosis resistant [6].

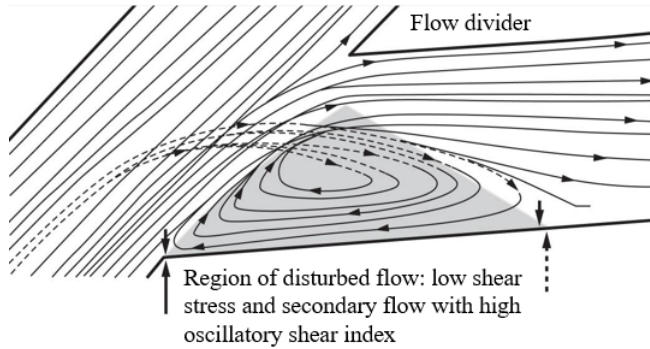


Figure 1.1: Illustration of flow separation at an arterial branch (adapted from [3]).

### 1.2.2. HEMODYNAMICS AND ANEURYSMS

Hemodynamics are also associated with the initiation, growth, and rupture of aneurysms. Abnormally high levels of WSS and positive gradient of WSS lead to local internal elastic lamina loss, media thinning, and bulge formation, which are the earliest signs of aneurysm formation [5], [7], [8]. For aneurysm growth and rupture, both high and low WSS cause ECM degradation, weakening the vessel wall and facilitating pathological progression. Specifically, low shear stress and high oscillatory shear index contribute to ECM degradation by increasing inflammatory markers in the vessel walls [9]–[11]. Regional high shear stress induces ECM degradation by producing matrix metalloproteinase and damaging the internal elastic lamina (the second part of the inner layer of vessel wall) [5].

There are studies trying to find association between flow patterns and aneurysm rupture. For instance, research has shown that blood flow impingement and helical flow dominated type of flow is highly prevalent in ruptured abdominal aortic aneurysms (AAA) [12]. Similarly, disturbed flow patterns, narrow jets, and small jet impingement areas are commonly observed in ruptured cerebral aneurysms [13].

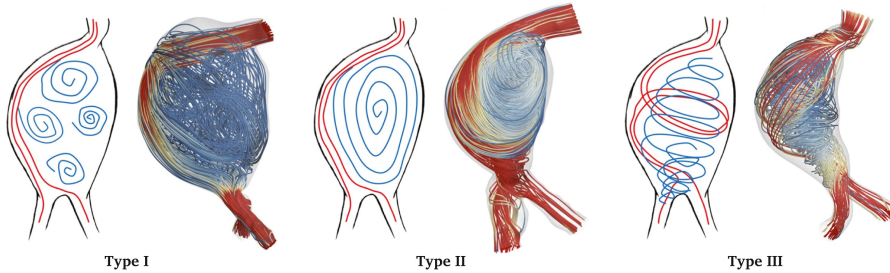


Figure 1.2: Three types of blood flow pattern found in abdominal aortic aneurysms. Type I is a non-helical flow with multiple vortices. Type II is non-helical flow with a dominant single vortex. Type III is helical flow dominated and there is wall impingement as well. Type III flow patterns are associated with an increased risk of aneurysm rupture (adapted from [12]).

### 1.2.3. HEMODYNAMICS AND HEART DYSFUNCTION

Similarly, blood flow dynamics in the left ventricle (LV) is also believed to play an important role in the function and efficiency of LV as a pump [14]–[16]. The LV flow is highly three-dimensional and is rich in vortices. In the early LV filling phase, a vortex ring is formed while blood entering the LV cavity from the atrium. It propagates deeply into the LV and lasts till isovolumic contraction (Fig. 1.3). This diastolic vortex ring formation is optimized naturally for efficient fluid transportation, minimizing momentum and kinetic energy compared to a stable, straight jet. It smoothly redirects the flow already to the outflow tract before the LV ejection [14]. Moreover, it also helps wash out the blood from the LV apical region, preventing possible thrombus formation [15]. Abnormal vortex formation and preservation can result in local ventricular wall shear stress changes or thrombosis formation, which eventually lead to LV remodeling and dysfunction [16].

## 1.3. BLOOD FLOW MEASUREMENT

### 1.3.1. CLINICAL FLOW ASSESSMENT

The common medical imaging techniques for *in vivo* blood flow measurements are ultrasound- and magnetic imaging-based. However, they have limitations in spatial resolution, temporal resolution. High spatial resolution techniques (e.g. intravascular ultrasound) are invasive, which require puncturing blood vessels, resulting in disturbance of the original flow conditions. The few non-invasive methods such as Doppler ultrasound and Phase-contrast magnetic resonance imaging (PC-MRI) are widely used in clinics for assessing blood flow.

Doppler ultrasound quantifies blood velocity in a volume based on the frequency shift of the acoustic waves. Its limitations include challenges in capturing velocities transverse to the ultrasound beam, potential aliasing at lower pulse repetition frequencies, trade-offs between spatial resolution and wide field of view in techniques like color Doppler, angle dependency affecting accuracy, and the inability to pinpoint the origin of velocity signals along the measurement line in continuous wave Doppler [17]–[20].

PC-MRI, commonly referred as 4D-Flow MRI, stands out for its ability to measure

blood flow in a three-dimensional (3D) volume, as well as capturing temporal information of the flow. This capability provides a more comprehensive understanding of blood flow dynamics compared to traditional Doppler ultrasound methods. One important limitation of MRI velocity measurement is the relatively low spatial and temporal resolution. Typically, MRI velocity measurements have the spatial resolution of 1 to 2 mm and a temporal resolution of 25 to 30 ms [21]. This limited spatial resolution may cause underestimation of WSS since WSS calculation is based on the measurement of the shear rate near wall [22]. Another drawback of MRI is that because of the limited temporal resolution, it requires the phase average of hundreds of heart beats to generate sequential flow, which elongates the acquisition time and introducing complications, such as breath-holding to avoid motion-related artefacts.

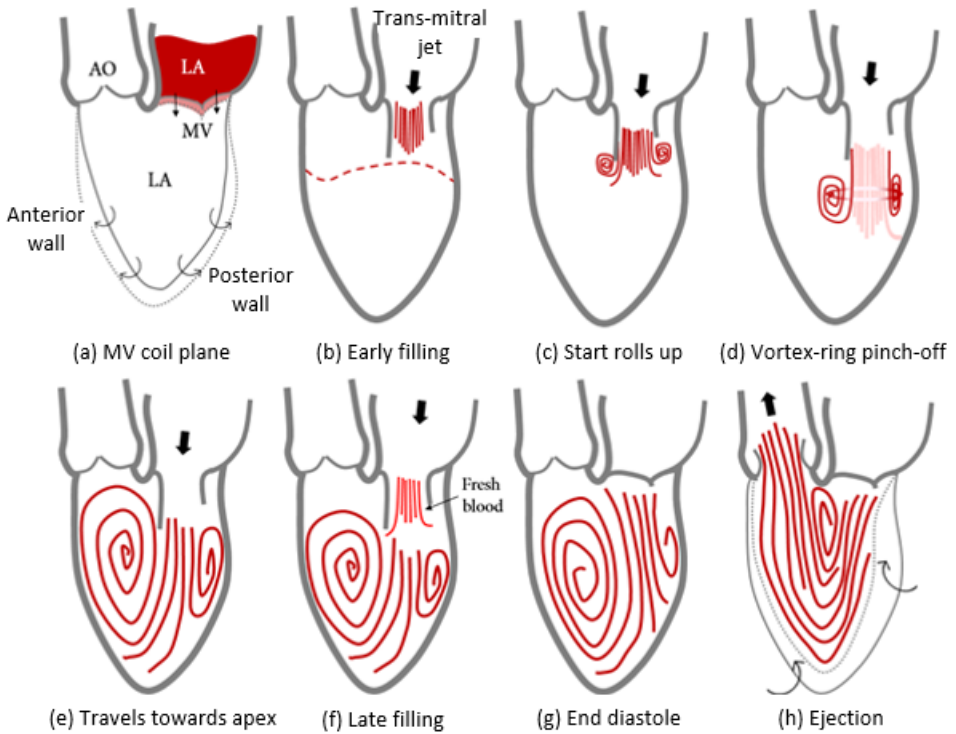


Figure 1.3: Sketch indication of vortex development in the left ventricle during a cardiac cycle (adapted from [23]).

### 1.3.2. COMPUTATIONAL FLUID DYNAMICS (CFD)

Due to the ability of providing non-invasive, high dimensional, and high spatiotemporal resolution data, CFD and *in vitro* particle image-based flow measurements have become complementary modalities to clinical techniques in blood flow assessment. CFD simu-

lates flows by seeking a numerical solution of the governing (Navier-Stokes) equations of fluid flow. The numerical solution requires mathematically defined boundary conditions and discretization of both the flow domain and time. CFD simulations are not only helpful in estimating the effect of variations in patient-specific dimensions such as the vessel geometries, flow boundary conditions, and variations in physiological properties of the individual, but are also helpful in predicting cardiovascular procedure and device success. However, due to strong modeling assumptions and variation of solver choices and settings, the acceptance of numerical approaches remains limited. For instance, in the 2013 CFD rupture challenge [24], CFD results among different groups varied significantly, although the geometry, boundary condition and fluid properties were similar and only the solution strategies were different. Therefore, validation using experimental methods is necessary.

### 1.3.3. *In vitro* PARTICLE IMAGE-BASED EXPERIMENTS

Particle image-based experiments usually are conducted on an *in vitro* setup, including transparent silicone replicas of the blood vessels, pulsatility generators, and blood-mimicking fluid. The flow is measured noninvasively by recording the particle tracers that are seeded in the flow and illuminated by laser. The state-of-the-art particle image-based measurement techniques include high speed Tomographic particle image velocimetry (PIV) and Lagrangian particle tracking (LPT) – Shake-the-Box. These techniques can provide highly-resolved velocity datasets to complement clinical measurements as well as to serve as validation purposes. However, the requirements of good mimicking patient-specific conditions, including physiological accurate models, boundary condition and blood mimicking fluid, makes the *in vitro* experiments highly complex and challenging. In literature, it is clear that the realistic conditions were rarely all achieved, which limits *in vitro* studies as a support of the cardiovascular patient-specific diagnosis. The principle of PIV and LPT techniques will be briefly introduced in the following section.

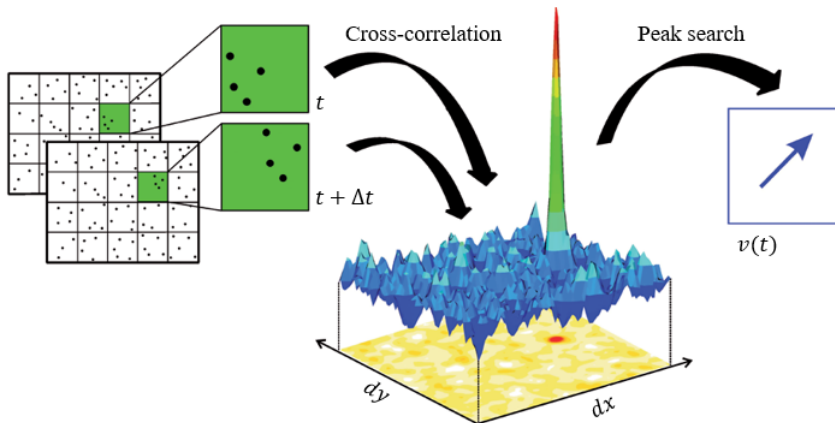


Figure 1.4: Indication of cross-correlation that used in PIV techniques. The highest peak in the correlation window indicates the most probable displacement vector (adapted from [25]).

## 1.4. PARTICLE IMAGE-BASED VELOCIMETRY

### 1.4.1. PARTICLE IMAGE VELOCIMETRY

Particle image velocimetry (PIV) is a class of noninvasive, optical measurement techniques which can visualize and quantify the velocity field within a flow domain [26]. It is based on imaging the motion of particle tracers in the flow. Sufficiently small particles are seeded in the fluid and illuminated by laser. Ideally, the particles can follow the flow faithfully. The scattered or emitted light of particles during subsequent exposures are captured by cameras and recorded in consecutive frames. In order to detect the displacement of the particles between two consecutive frames, the measurement domain is subdivided into interrogation windows and a correlation analysis  $R(s)$  is performed in each one of those windows

$$R(s) = \int I_1(X)I_2(X+s)dX \quad (1.1)$$

$I_1$  and  $I_2$  are the light intensity field of the image plane at time  $t$  and  $t + \Delta t$  respectively, and  $s$  is the separation vector. The peak value of displacement correlation  $R(s)$  reaches a maximum when  $s = d$ , where  $d$  is the particle image displacement. Hence, the velocity  $v$  can be obtained, where  $M$  is the magnification

$$v = \frac{d}{\Delta t} \quad (1.2)$$

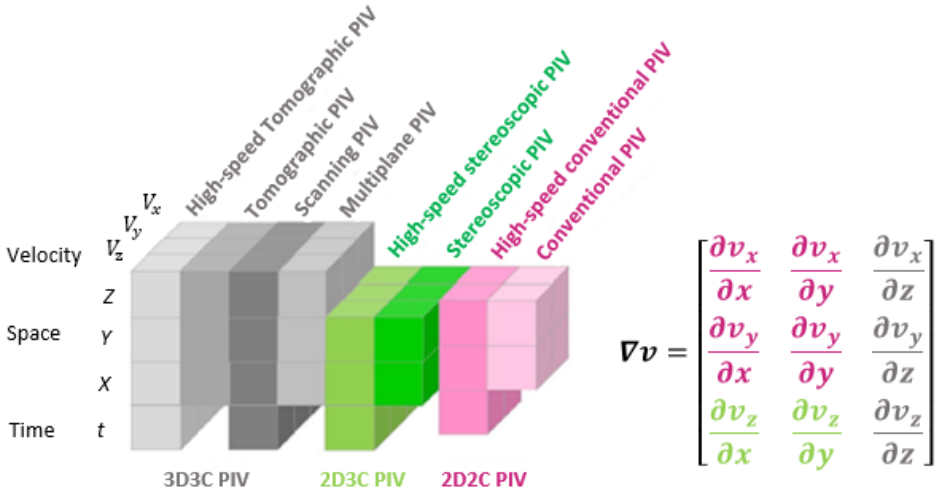


Figure 1.5: PIV techniques based on the number of velocity components measured, dimensions (single plane or the whole domain), and time (single time-step or a complete sequence). The corresponding velocity gradient is shown (adapted from [23]).

With the development of digital cameras and high-power pulsed laser, PIV is now a golden standard technique for fluid velocity measurements. In biomedical applications,

several PIV techniques such as planar PIV and Tomographic PIV are commonly used. Planar PIV is a two dimensional (2D) technique, it measures velocity components in a plane. As Fig. 1.5 shows, both conventional PIV and Stereoscopic PIV are Planar PIV techniques. The difference is that conventional PIV uses one camera and gives only two in-plane velocity components (2C), however Stereoscopic PIV utilizes two cameras viewing an illuminated plane from two different angles, resolving all three velocity components (3C). Planar PIV measurements has been applied in vascular flow investigation [27], [28]. It can offer some insights into the flow characteristics, but important hemodynamic parameters such as the 3D velocity gradient tensor and hence 3D WSS are only accessible with 3D techniques. Some work in this direction has been undertaken through multiplane Stereoscopic PIV, scanning light sheet PIV, holographic PIV, and Tomographic-PIV.

### STEREOSCOPIC PIV

Stereoscopic PIV (Stereo-PIV) is a 2D3C technique, allowing measurements of all three velocity components (3C) in a two-dimensional (2D) plane. It utilizes two cameras recording images of an illuminated plane from two different angles. The 2D2C in-plane velocity is separately computed from each camera first and then is used for reconstruction of the 3C velocity vectors at the world position. In a typical camera setup (Fig. 1.6), the measured  $x$ -components  $V_{1x}$  and  $V_{2x}$  in camera 1 and 2 raw images are given by

$$\begin{aligned} V_{1x} &= V_x \cos \alpha_1 + V_z \sin \alpha_1 \\ V_{2x} &= V_x \cos \alpha_2 + V_z \sin \alpha_2 \end{aligned} \quad (1.3)$$

the  $y$  components of velocity measured by both cameras are identical

$$V_{1y} = V_{2y} = V_y \quad (1.4)$$

where  $V = (V_x, V_y, V_z)$  are the true velocity components in the world coordinate system and the  $z$ -axis here points away from the cameras. Solving the equation above leads to

$$\begin{aligned} V_x &= (V_{1x} \sin \alpha_2 - V_{2x} \sin \alpha_1) / \sin(\alpha_2 - \alpha_1) \\ V_y &= (V_{1y} + V_{2y}) / 2 \\ V_z &= (V_{1x} \cos \alpha_2 - V_{2x} \cos \alpha_1) / \sin(\alpha_2 - \alpha_1) \end{aligned} \quad (1.5)$$

$\alpha_1$  and  $\alpha_2$  are obtained *via* calibration. Moreover, to use above 3C reconstruction, a conversion of the image plane coordinates  $(x, y)$  to the physical world coordinates  $(X, Y)$  is necessary, which can be provided by a single image of co-planar calibration markers. However, to calculate the camera viewing angles, a set of multi-layered images of markers with a known displacement in the depth direction is needed. Therefore, the calibration for Stereo-PIV is done by mapping the markers on a physical plate aligned by a laser sheet to the image plane at a few parallel positions in the depth direction, resulting a polynomial mapping function. The mapping function is firstly used to de-warp the particle images from two separate views into the same coordinate system. In practice, the mapping function needs correction (namely self-calibration) due to the imperfect alignment between the calibration plate and the laser sheet. The misalignment can be determined by cross-correlating the de-warped particle images from the two cameras, producing a disparity map that provides correction for the mapping functions. By iterating

the process, the disparity vectors can typically be minimized to below 0.1 pixel. Based on the de-warped particle images and corrected mapping functions, 2D2C vectors from each camera view are calculated on 2D interrogation windows through cross-correlating two sequential images. The third velocity component is then reconstructed using above equations. The general work flow of Stereo-PIV algorithm is depicted in Fig. 1.7.

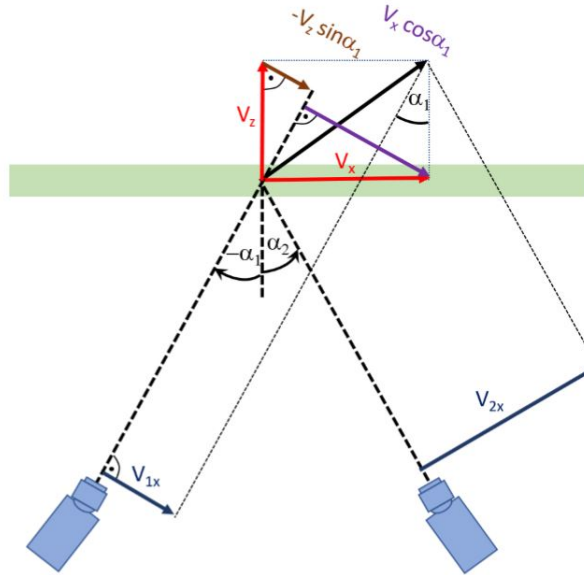


Figure 1.6: Stereoscopic imaging configurations: angular lens displacement with Scheimpflug condition (adapted from LaVision).

Please note that now still only six of the nine components of the velocity gradient tensor (refer to Fig 1.5) are obtained. It can be extended to a full 3D3C system by performing multiplane Stereo-PIV [29], which basically interpolates a set of 2D3C velocity data from multiple planes to the 3D domain, resulting in one 3D3C velocity dataset. An application of the multi-plane Stereo-PIV is presented in Chapter 2 of this thesis.

### TOMOGRAPHIC PIV

Tomographic PIV (Tomo-PIV) stands out from Stereo-PIV by directly measuring a volume rather than a 2D plane, yielding all three velocity components (3C) in a 3D domain. The general workflow of the Tomo-PIV algorithm is illustrated in Fig. 1.7. In the Tomo-PIV experiments, a volume that covers the field of view (FOV) is illuminated by the laser beam, and multiple cameras are placed around the FOV from different angles to capture the scattered light by seeded particles in the flow. Typically, 3 to 6 cameras are used to record images from non-collinear positions, such that each camera angle provides as much new information as possible. Similar to Stereo-PIV, the mapping function of the physical world coordinate system  $(X, Y, Z)$  and its projections onto the image planes  $(x_i, y_i)$  are established by volumetric calibration and refined through self-calibration ( $<0.1$

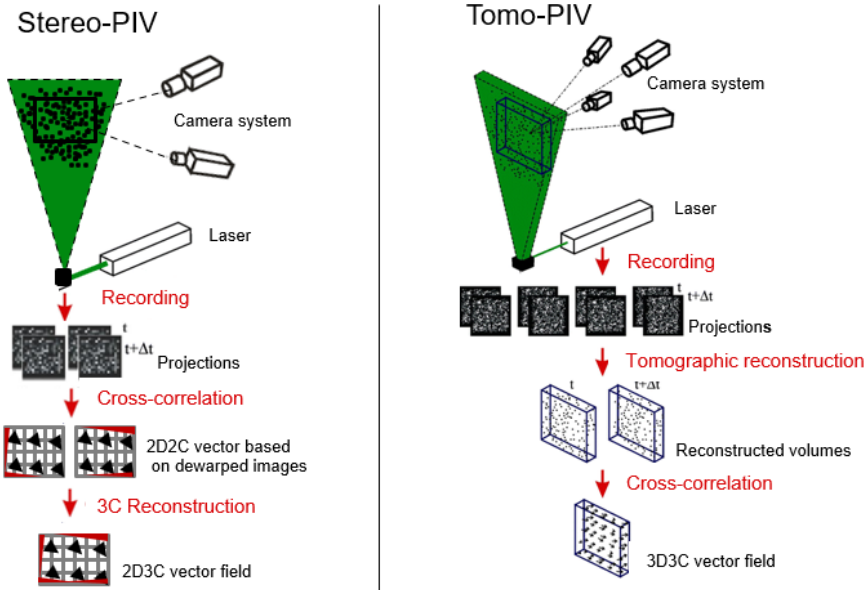


Figure 1.7: Schematic illustration of Stereo-PIV and Tomo-PIV technique (adapted from [30]).

pixel). Subsequently, tomographic reconstruction is conducted based on the recorded particle images and the mapping function. The tomographic reconstruction reconstructs the 3D light intensity distribution  $E(X, Y, Z)$  scattered by particle tracers yet recorded in the 2D images in multiple views. Therefore, the intensity recorded by each pixel of the camera is an integration of the intensity contributed by multiple particles along a view direction through the volume (Fig. 1.8). Commonly, the 3D intensity distribution  $E(X, Y, Z)$  is reconstructed by multiplicative algebraic reconstruction technique (MART) [30]. The algebraic method solves a linear equation linking the pixel intensity  $I(x_i, y_i)$  in the image space to the 3D space

$$\sum_{j \in N_j} w_{i,j} E(X_j, Y_j, Z_j) = I(X_i, Y_i) \quad (1.6)$$

where  $i$  identifies the  $i_{th}$  pixel and  $N_i$  the number of voxels along the line-of-sight (LOS) of the pixel which contributes to its intensity. The value  $w$  defines the weight of the contribution of the  $j_{th}$  voxel to the  $i_{th}$  pixel's intensity and depends from the distance between the voxel and the line-of-sight. After tomographic particle reconstruction of each time-step, 3D3C velocity vectors are calculated on 3D interrogation boxes through 3D cross-correlation.

Note that the spatial resolution of the Tomo-PIV measurements is ultimately determined by the particle density that is seeded in the flow. A minimum of 5-10 particles per interrogation box is required for a robust 3D cross-correlation (70%-90% accuracy) [30]. On the other hand, an increase of particles per interrogation box is limited by the maximum particle density that can ensure a successful 3D particle reconstruction. In

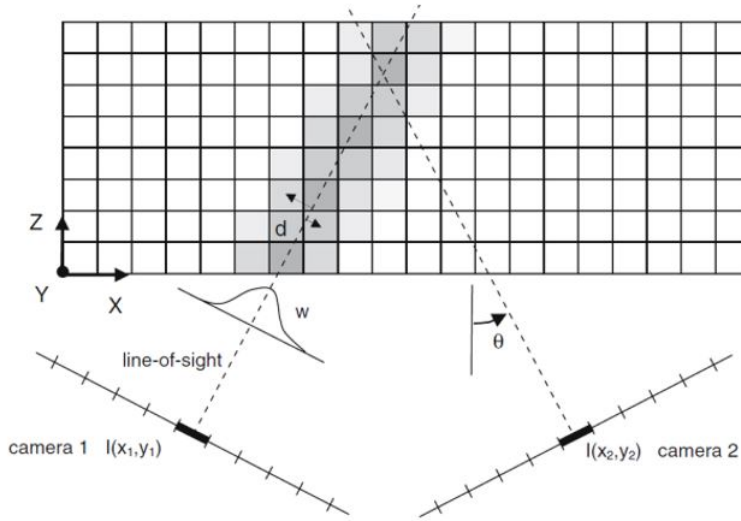


Figure 1.8: Sketch of the Two-dimensional projection model for tomographic reconstruction; dashed lines indicate the pixels' LOS. Voxels are grey color-coded depending on the value of  $w$  and their distance from the LOS is indicated with  $d$  (adapted from [30]).

Tomo-PIV reconstruction, ghost particles that could introduce vector bias error increases as the number of particles along the line-of-sight increases [31]. Therefore, the reconstruction of the 3D particle distribution is strongly correlated with seeding density. With a typical four camera system, a seeding density up to 0.05 ppp (particle per pixel) is allowed [32], with a reconstruction rate of 99% true particles, 20% ghost particle occurrence, and a particle position accuracy of 0.2 pixel [33].

#### 1.4.2. LAGRANGIAN PARTICLE TRACKING

As a robust 3D flow measurement technique, Tomo-PIV still has some technical drawbacks. An important one is the spatial averaging over interrogation boxes introduced by cross-correlation. As a result, velocity gradients and fine flow structures are smoothed out [33]. In contrast, volumetric particle tracking velocimetry (PTV) techniques, often referred as Lagrangian particle tracking (LPT), track each individual particle in the three-dimensional domain, providing precise determination of positions, velocity and acceleration without spatial averaging [33]. Therefore, to evaluate gradient-based quantities such as shear stress, LPT methods are more suitable compared to cross-correlation based techniques, especially in measuring strong-shear flow, turbulent flow, and near-wall regions. The general workflow of LPT methods is shown in Fig. 1.9.

#### 3D PTV

3D PTV, as one of the LPT methods, has been developed and applied over 35 years. The data acquisition of 3D PTV is the same as Tomo-PIV techniques. A set of sequential particle images of the flow are recorded by high speed cameras. For 3D PTV, at least two cameras are needed. Each camera identifies 2D particle positions through 2D peak detec-

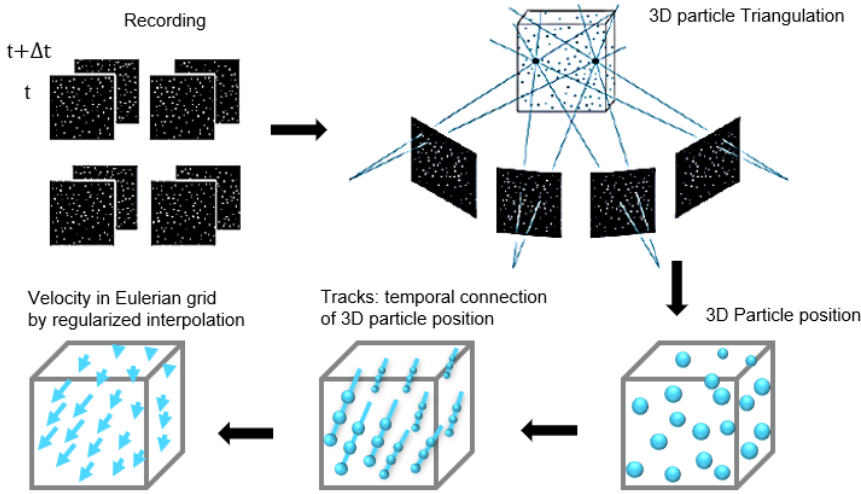


Figure 1.9: Flow chart and schematic illustration of Lagrangian particle tracking experiment.

tion (detecting particle image peaks with a specified intensity threshold). To reconstruct 3D particle positions, 3D PTV uses calibration and epipolar geometry to find the true candidates with an allowed triangulation error  $\epsilon$  ( $\sim 1$  pixel). As shown in Fig. 1.10, originating from particle candidate  $P'$  on one sensor, the epipolar line of the second sensor is calculated with the known image-space mapping functions of the cameras from calibration procedure. On the epipolar line, the corresponding particle candidates ( $P''_a, P''_b, P''_c$ ) of the second sensor are found with an allowed error  $\epsilon$ . Due to the large total number of imaged particles, many ambiguities exist in the found corresponding candidates, making it difficult to determine the true match. By adding the third camera, the ambiguity problem can be solved to an extent. As Fig. 1.10 shows, there is a large probability that the epipolar lines on the third sensor intersect each other at one single point  $P'''_e$  which is very close to one of the candidates. A real 3D particle position is then assumed. This procedure is called triangulation as the projective centres of the three-camera setup form a triangle. Initial 3D particle positions of each time-step are triangulated independently. 3D particle trajectories are then built by carefully selecting particles from the initial 3D particle reconstruction. Only particles with the lowest acceleration over past and future time-steps are selected and added to the trajectory [34]. Based on the trajectories, the velocity is estimated by a polynomial fitting.

For the 3D PTV algorithm, a reliable 3D particle reconstruction is limited to a particle image density of 0.005 ppp. Accurate 2D and 3D particle positioning relies on the low overlapping of particle images. For higher seeding density, 2D peak detection would be shifted due to the overlapping particle images, resulting in high 2D particle positional errors. Moreover, the number of ambiguities grows with an increase in seeding density, leading to an inaccurate triangulation. For this reason, a more advanced particle tracking scheme is required to ensure a robust particle tracking in high seeding density flow.

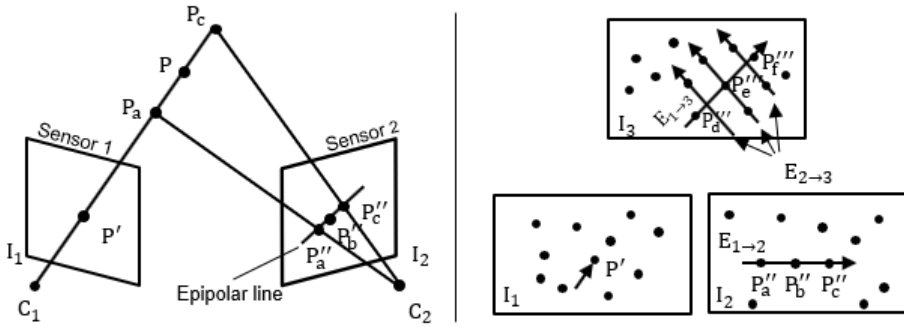


Figure 1.10: Demonstration of the use of epipolar geometry in triangulation. Particle position  $P$  in space is triangulated from corresponding 2D image positions  $P'$  and  $P''$  from two cameras (left) (adapted from Lavision). Principle of intersection of epipolar lines for three camera setup (right) (adapted from [35]).

### SHAKE-THE-BOX

Shake-the-Box is the state-of-the-art of LPT technique. It overcomes the low particle image density constriction by applying particle position refinement scheme - 'shaking' [36], advanced triangulation algorithm - iterative particle reconstruction (IPR) technique [37], and by exploitation of the known temporal information - predicting the particle position of the next time-step via extrapolating the known trajectories. To initiate the tracking-reconstruction process, STB needs some velocity information to be available at hand. Therefore, particle reconstruction is performed at the first four time-steps to extract particle trajectories as *priori* knowledge for predicting the particle distributions of the next time-step. The IPR technique is used to reconstruct particles at the first four time-steps as initialization.

IPR is an iterative approach of particle triangulation that can accurately reconstruct volumetric particle distributions in densely seeded flows (up to 0.05 ppp) [37]. It starts with a standard 3D particle triangulation followed by a projection of the triangulated particles, calculation of the residual images, an inner loop of particle position refinement and filtering, and finally triangulation of new particles from the residual images. The triangulated particles are backprojected to the 2D images, producing projected images. Residual images are then created by subtracting the projected images from the original images. The backprojection demands geometrical calibration and volume self-calibration. To increase the projection accuracy, IPR also calculates local optical functions (OTF) to describe the varying particle shapes which covers most optical distortions like blurring and astigmatism [37]. The initial 3D particle distribution through standard 3D particle triangulation contains errors ( $\sim 1-2$  pixel) due to image noise, image overlapping, and limited 2D peaks detection. To enhance the accuracy, particle positions are refined with image matching technique (shaking), by moving particles in the reprojected images by  $\pm 0.1$  voxel in space to find the best match to the original images [37]. Ghost particles are removed by filtering the particles whose intensity is below a specified threshold. This 'shaking' technique is not only used in IPR but also is an important part of the STB process.

After that, new residual images are obtained and new particle triangulation is conducted. Note that it is important to use a small triangulation error (e.g. 0.5-1 pixel) such that noisy 3D particles originating from overlapping are eliminated effectively [37].

Based on the first four time-steps, particle trajectories are built and extrapolated to the next time-step to predict a new particle distribution. This predicted particle distribution is first corrected by shaking, and then an extended IPR process is applied to identify new particles that are not tracked by the previous time-steps. New particle tracks are then built and ready to be used for the prediction of next time-step. The complete STB scheme is shown in Fig. 1.11. The particle-based velocity and acceleration information then can be interpolated to a Eulerian frame using data assimilation [38].

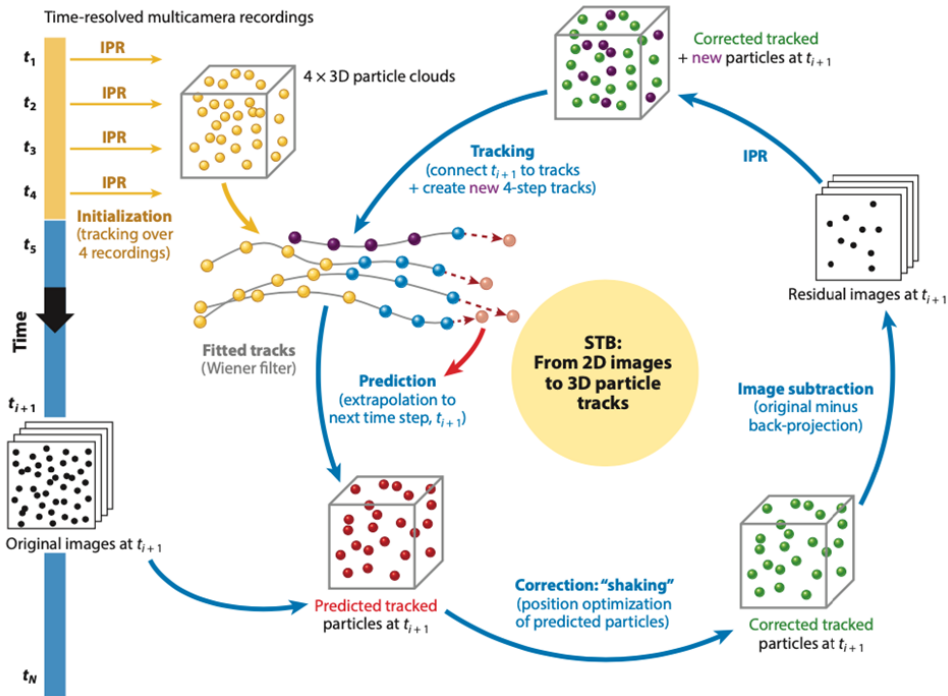


Figure 1.11: An illustration of STB scheme (adapted from [39]).

### 1.4.3. COMPARISON OF THE PARTICLE IMAGE-BASED TECHNIQUES

Stereo-PIV is a 2D3C technique which is not inherently a 3D technology, posing limitations in measuring highly three-dimensional vascular flows. Time-resolved Tomo-PIV offers tomographic reconstruction of particles at each time-step and 3D3C velocity information based on 3D cross-correlation. More importantly, Tomo-PIV is able to work with high seeding density flows (0.01-0.2 ppp), resolving high spatial resolution velocity data. However, because of the averaging smoothing effect brought by 3D cross-correlation, it is less superior than particle tracking methods which offer particle-based flow information.

Conventional 3D PTV is a volumetric particle tracking method. It builds particles and particle tracks of every time-step at low seeding density flows (up to 0.005 ppp). This seeding density is at least an order of magnitude lower than Tomo-PIV and advanced particle tracking method - STB.

The particle image density that STB can process is comparable to that of Tomo-PIV (0.01-0.2 ppp) but with higher accuracy. At a seeding density of 0.125 ppp, STB can reconstruct nearly 99.5% of the particles with almost no ghost particles (< 0.004% false particles) and high positional accuracy (average position error of 0.018 pixel) [33]. Tomographic reconstruction can also process such high particle image density, but at much higher ghost particle occurrence (>250% false particles) and a much lower accuracy (average position error of 0.3 pixel) [33]. Moreover, instead of reconstructing particles at each time-step, STB uses the known particle tracks to predict the particle positions of the next time-step and adds new particles by only triangulate the residual images. This method greatly reduces the amount of data and the process time (4-6 times [33]) compared to 3D PTV and Tomo-PIV.

## 1.5. OBJECTIVE AND OUTLINE

### 1.5.1. OBJECTIVE

The main objective of this research is to improve the fidelity of *in vitro* blood flow modeling and provide detailed, precise evaluation of complex cardiovascular flows. We can approach them from two aspects: realistic blood flow simulator, and accurate flow measurements. Realistic blood flow simulator should integrate as much physiological information as possible, i.e., patient-specific shape, deformable vessel wall, physiological flow condition, and non-Newtonian blood mimicking fluid. Based on the high bio-fidelity blood flow simulator, accurate flow measurement should be three-dimensional, time-resolved, and high-resolution. This can be achieved by using advanced volumetric optical flow measurement techniques – Tomographic particle image velocimetry and Lagrangian particle tracking ‘Shake-the-Box’.

### 1.5.2. OUTLINE

Chapter 2 demonstrates the necessity of using three-dimensional, high-resolution flow measurement techniques for hemodynamic studies. We will conduct a multi-modality study on the blood flow in a patient-specific intracranial aneurysm. The modalities include *in vivo* 4D-Flow MRI, *in silico* CFD, *in vitro* 2D technique - Stereoscopic PIV, and *in vitro* 3D technique - Tomographic PIV. Blood flow patterns, velocity, and WSS were qualitatively and quantitatively compared across modalities.

Chapter 3 is to firstly, demonstrate the feasibility of applying advanced Lagrangian particle tracking technique – Shake-the-Box to reconstruct the highly complicated flow in a realistic-shaped, compliant left ventricle. Moreover, this chapter also aims to explore new flow analysis techniques due to the complexity we experienced in the multi-modality study. Different methods (*in vivo*, *in silico*, *in vitro*) have different coordinates, spatiotemporal resolutions, and data heterogeneity etc., posing challenges for comparing results across modalities. Therefore, proper orthogonal decomposition will be used as a new blood flow analysis technique for an easier and efficient flow analysis.

In chapter 4, will focus on improving the bio-fidelity of the blood flow simulator: (1) a patient-specific, fully optical transparent, compliant aorta will be manufactured using brush-spin-heat coating method, (2) physiological pressure and flow rate are simulated using a combination of a left ventricular assist device (VAD) and a VAD driving system, (3) the realistic aorta phantom together with the flow condition operator will provide physiological lumen distensibility and aortic flow. The flow measurements will be conducted by Shake-the-Box and will be compared to *in vivo* 4D-Flow MRI.

In chapter 5, we will summarize our key findings and provide suggestions for future research.

# REFERENCES

- [1] E. N. Marieb and K. Hoehn, *Human anatomy & physiology*. Pearson Education, 2007.
- [2] WHO. “Cardiovascular diseases (CVDs)”. (2019).
- [3] P. F. Davies, “Hemodynamic shear stress and the endothelium in cardiovascular pathophysiology”, *Nature Clinical Practice Cardiovascular Medicine*, vol. 6, no. 1, pp. 16–26, 2009.
- [4] E. Roux, P. Bougaran, P. Dufourcq, and T. Couffignal, “Fluid shear stress sensing by the endothelial layer”, *Frontiers in Physiology*, vol. 11, p. 861, 2020.
- [5] H. Meng, V. Tutino, J. Xiang, and A. Siddiqui, “High WSS or low WSS? complex interactions of hemodynamics with intracranial aneurysm initiation, growth, and rupture: Toward a unifying hypothesis”, *American Journal of Neuroradiology*, vol. 35, no. 7, pp. 1254–1262, 2014.
- [6] M. A. Gimbrone Jr and G. García-Cardeña, “Vascular endothelium, hemodynamics, and the pathobiology of atherosclerosis”, *Cardiovascular Pathology*, vol. 22, no. 1, pp. 9–15, 2013.
- [7] Z. Kulcsár, A. Ugron, M. Marosfői, Z. Berentei, G. Paal, and I. Szikora, “Hemodynamics of cerebral aneurysm initiation: The role of wall shear stress and spatial wall shear stress gradient”, *American Journal of Neuroradiology*, vol. 32, no. 3, pp. 587–594, 2011.
- [8] H. Meng, Z. Wang, Y. Hoi, *et al.*, “Complex hemodynamics at the apex of an arterial bifurcation induces vascular remodeling resembling cerebral aneurysm initiation”, *Stroke*, vol. 38, no. 6, pp. 1924–1931, 2007.
- [9] A. J. Boyd, D. C. Kuhn, R. J. Lozowy, and G. P. Kulbisky, “Low wall shear stress predominates at sites of abdominal aortic aneurysm rupture”, *Journal of Vascular Surgery*, vol. 63, no. 6, pp. 1613–1619, 2016.
- [10] C. Trenti, M. Ziegler, N. Bjarnegård, T. Ebbers, M. Lindenberger, P. Dyverfeldt, *et al.*, “Wall shear stress and relative residence time as potential risk factors for abdominal aortic aneurysms in males: A 4D flow cardiovascular magnetic resonance case-control study”, *Journal of Cardiovascular Magnetic Resonance*, vol. 24, no. 1, p. 18, 2022.
- [11] J. Xiang, S. K. Natarajan, M. Tremmel, *et al.*, “Hemodynamic–morphologic discriminants for intracranial aneurysm rupture”, *Stroke*, vol. 42, no. 1, pp. 144–152, 2011.

- [12] Y. Qiu, J. Wang, J. Zhao, T. Wang, T. Zheng, and D. Yuan, "Association between blood flow pattern and rupture risk of abdominal aortic aneurysm based on computational fluid dynamics", *European Journal of Vascular and Endovascular Surgery*, vol. 64, no. 2-3, pp. 155–164, 2022.
- [13] J. R. Cebal, M. A. Castro, J. E. Burgess, R. S. Pergolizzi, M. J. Sheridan, and C. M. Putman, "Characterization of cerebral aneurysms for assessing risk of rupture by using patient-specific computational hemodynamics models", *American Journal of Neuroradiology*, vol. 26, no. 10, pp. 2550–2559, 2005.
- [14] P. J. Kilner, G.-Z. Yang, A. J. Wilkes, R. H. Mohiaddin, D. N. Firmin, and M. H. Yacoub, "Asymmetric redirection of flow through the heart", *Nature*, vol. 404, no. 6779, pp. 759–761, 2000.
- [15] J. H. Seo, V. Vedula, T. Abraham, *et al.*, "Effect of the mitral valve on diastolic flow patterns", *Physics of Fluids*, vol. 26, no. 12, 2014.
- [16] G. Pedrizzetti, G. La Canna, O. Alfieri, and G. Tonti, "The vortex—an early predictor of cardiovascular outcome?", *Nature Reviews Cardiology*, vol. 11, no. 9, pp. 545–553, 2014.
- [17] R. W. Gill, "Measurement of blood flow by ultrasound: Accuracy and sources of error", *Ultrasound in Medicine & Biology*, vol. 11, no. 4, pp. 625–641, 1985.
- [18] A. A. Oglat, M. Matjafri, N. Suardi, M. A. Oqlat, M. A. Abdelrahman, and A. A. Oqlat, "A review of medical doppler ultrasonography of blood flow in general and especially in common carotid artery", *Journal of Medical Ultrasound*, vol. 26, no. 1, p. 3, 2018.
- [19] A. W. Quail, D. Cottee, and S. W. White, "Limitations of a pulsed doppler velocimeter for blood flow measurement in small vessels", *Journal of Applied Physiology*, vol. 75, no. 6, pp. 2745–2754, 1993.
- [20] L. Wan, N. Yang, C.-Y. Hiew, *et al.*, "An assessment of the accuracy of renal blood flow estimation by doppler ultrasound", *Intensive Care Medicine*, vol. 34, pp. 1503–1510, 2008.
- [21] P. P. Sengupta, G. Pedrizzetti, P. J. Kilner, *et al.*, "Emerging trends in CV flow visualization", *JACC: Cardiovascular Imaging*, vol. 5, no. 3, pp. 305–316, 2012.
- [22] R. S. Reneman, T. Arts, and A. P. Hoeks, "Wall shear stress—an important determinant of endothelial cell function and structure—in the arterial system in vivo: Discrepancies with theory", *Journal of Vascular Research*, vol. 43, no. 3, pp. 251–269, 2006.
- [23] H. Saaid, "Multimodality analyses of 3D flow in a phantom model of the left ventricle", Ph.D. dissertation, Ghent University, 2019.
- [24] P. Berg, C. Roloff, O. Beuing, *et al.*, "The computational fluid dynamics rupture challenge 2013—phase ii: Variability of hemodynamic simulations in two intracranial aneurysms", *Journal of Biomechanical Engineering*, vol. 137, no. 12, p. 121 008, 2015.
- [25] B. Wieneke, "PIV uncertainty quantification and beyond", Ph.D. dissertation, Delft University of Technology, 2017.

- [26] J. Kompenhans, *Particle Image Velocimetry-A practical guide*. Springer-verlag Berlin and Hei, 2014.
- [27] J. Bale-Glickman, K. Selby, D. Saloner, and O. Savas, “Experimental flow studies in exact-replica phantoms of atherosclerotic carotid bifurcations under steady input conditions”, *Journal of Biomechanical Engineering*, vol. 125, no. 1, pp. 38–48, 2003.
- [28] N. A. Buchmann, M. C. Jermy, and C. V. Nguyen, “Experimental investigation of carotid artery haemodynamics in an anatomically realistic model”, *International Journal of Experimental and Computational Biomechanics*, vol. 1, no. 2, pp. 172–192, 2009.
- [29] C. Kähler, “Investigation of the spatio-temporal flow structure in the buffer region of a turbulent boundary layer by means of multiplane stereo PIV”, *Experiments in Fluids*, vol. 36, pp. 114–130, 2004.
- [30] G. E. Elsinga, F. Scarano, B. Wieneke, and B. W. van Oudheusden, “Tomographic particle image velocimetry”, *Experiments in Fluids*, vol. 41, no. 6, pp. 933–947, 2006.
- [31] G. Elsinga, J. Westerweel, F. Scarano, and M. Novara, “On the velocity of ghost particles and the bias errors in tomographic-PIV”, *Experiments in Fluids*, vol. 50, pp. 825–838, 2011.
- [32] F. Scarano and C. Poelma, “Three-dimensional vorticity patterns of cylinder wakes”, *Experiments in Fluids*, vol. 47, pp. 69–83, 2009.
- [33] D. Schanz, S. Gesemann, and A. Schröder, “Shake-the-box: Lagrangian particle tracking at high particle image densities”, *Experiments in Fluids*, vol. 57, pp. 1–27, 2016.
- [34] M. Raffel, C. E. Willert, F. Scarano, C. J. Kähler, S. T. Wereley, and J. Kompenhans, *Particle image velocimetry: a practical guide*. Springer, 2018.
- [35] H. Maas, A. Gruen, and D. Papantoniou, “Particle tracking velocimetry in three-dimensional flows: Part 1. photogrammetric determination of particle coordinates”, *Experiments in Fluids*, vol. 15, no. 2, pp. 133–146, 1993.
- [36] D. Schanz, S. Gesemann, A. Schröder, B. Wieneke, and M. Novara, “Non-uniform optical transfer functions in particle imaging: Calibration and application to tomographic reconstruction”, *Measurement Science and Technology*, vol. 24, no. 2, p. 024 009, 2012.
- [37] B. Wieneke, “Iterative reconstruction of volumetric particle distribution”, *Measurement Science and Technology*, vol. 24, no. 2, p. 024 008, 2012.
- [38] S. Gesemann, F. Huhn, D. Schanz, and A. Schröder, “From noisy particle tracks to velocity, acceleration and pressure fields using b-splines and penalties”, in *18th International Symposium on Applications of Laser and Imaging Techniques to Fluid Mechanics, Lisbon, Portugal*, vol. 4, 2016.
- [39] A. Schröder and D. Schanz, “3D lagrangian particle tracking in fluid mechanics”, *Annual Review of Fluid Mechanics*, vol. 55, pp. 511–540, 2023.

# 2

## MULTIMODALITY STUDY OF A PATIENT-SPECIFIC INTRACRANIAL ANEURYSM

### A COMPARATIVE ASSESSMENT BY TOMOGRAPHIC PIV, STEREOSCOPIC PIV, IN VIVO MRI AND COMPUTATIONAL FLUID DYNAMICS

#### **Background**

*Wall shear stress (WSS) is associated with the growth and rupture of aneurysms. To reveal their underlying connections, many single-modality studies have been conducted. Multimodality study that integrates in vivo, in vitro, and in silico datasets is one of the proposed approach for comprehensive hemodynamic assessments, as well as for understanding the advantages and disadvantages of each modality.*

#### **Methods**

*In the present study, we performed a comparative assessment on the hemodynamics of a patient-specific intracranial aneurysm using in vivo 4D-Flow MRI, in silico CFD, in vitro Stereoscopic and Tomographic particle imaging velocimetry (Stereo-PIV and Tomo-PIV) techniques. PIV experiments and CFD were conducted under steady state corresponding to the peak systole of 4D-Flow MRI.*

#### **Results**

*The results showed that all modalities provided similar flow features and overall surface*

---

This chapter has been published as: Wu, X., Gürzing, S., Schinkel, C., Toussaint, M., Perinajová, R., van Ooij, P. and Kenjereš, S., Hemodynamic Study of a Patient-Specific Intracranial Aneurysm: Comparative Assessment of Tomographic PIV, Stereoscopic PIV, In Vivo MRI and Computational Fluid Dynamics. *Cardiovasc Eng Tech* 13, 428–442 (2022).

*distribution of WSS. However, a large variation in the absolute WSS values was found. 4D-Flow MRI estimated a 2-4-fold lower peak WSS (3.99 Pa) and a 1.6-2-fold lower mean WSS (0.94 Pa) than Tomo-PIV, Stereo-PIV, and CFD. Bland-Altman plots of WSS showed that the differences between PIV-/CFD-based WSS and 4D-Flow MRI-based WSS increase with higher WSS magnitude. Such proportional trend was absent in the Bland-Altman comparison of velocity where the resolutions of PIV and CFD datasets were matched to 4D-Flow MRI. We also found that because of superior resolution in the out-of-plane direction, WSS estimation by Tomo-PIV was higher than Stereo-PIV.*

**Conclusions**

*Our results indicated that the differences in spatial resolution could be the main contributor to the discrepancies between each modality. The findings of this study suggest that with current techniques, care should be taken when using absolute WSS values to perform a quantitative risk analysis of aneurysm rupture.*

## 2.1. INTRODUCTION

Intracranial aneurysm is an abnormal localized enlargement of an artery in the cerebral vasculature. It is estimated that 1-5% of the general population are affected by this condition and that 20-30% of the affected population have multiple aneurysms [1]–[3]. The rupture of an intracranial aneurysm can cause subarachnoid haemorrhage (SAH), which has a high mortality rate of almost 50% [4]. On the other hand, the clinical treatment of an unruptured aneurysm also comes with risks [5]. Therefore, once detected, a rupture risk analysis of the existing aneurysm is important.

Hemodynamics can potentially help with the risk analysis of aneurysm rupture [6], [7]. To reveal the underlying connection between hemodynamics and the progression of intracranial aneurysms, various parameters have been studied in the literature. Among them, wall shear stress (WSS) has attracted extensive attention. The accurate calculation of WSS requires three-dimensional three-components (3D3C) velocity data with high spatiotemporal resolutions. Current non-invasive medical techniques such as phase-contrast magnetic resonance imaging (PC-MRI) can provide *in vivo* insights into the local blood flow and WSS distribution [8]–[10]. However, the accuracy of WSS *in vivo* estimation can be limited by imaging noise, artefacts, and relatively low spatiotemporal resolutions available—especially in smaller blood vessels commonly encountered in the brain vasculature [11].

Over the past decades, computational fluid dynamics (CFD) has been extensively applied in various arterial flows due to their ability to simulate instantaneous 3D velocity field and corresponding WSS [12]–[15]. Especially with the advancement of medical imaging in recent years, image-based CFD can be applied in patient-specific studies, making it a potential tool for assisting clinical decision-making in the future [16]. However, uncertainties due to imposed modelling assumptions and variations of solution strategies in CFD produced controversial reports, such as the aneurysm rupture is caused by either high or low WSS [14], [17]–[20]. This is one of the reasons that hinder the clinical translational value of hemodynamics. Hence, the validation of CFD results through either *in vitro* or *in vivo* measurements is necessary. Nevertheless, limited computer simulations results, particularly the CFD-based WSS, have been experimentally verified. Optical imaging measurement techniques, such as particle image velocimetry (PIV), are often used for *in vitro* validations because they provide well-controlled, high-resolution flow fields. The challenge is that the three-dimensional WSS requires a complete velocity gradient tensor, which did not become achievable in optical experiments until the last decade followed by the developments of the full 3D measurement techniques, such as multi-plane Stereoscopic PIV (Stereo-PIV), Tomographic PIV (Tomo-PIV) and Shake-the-Box (STB) [21]–[24].

In the current active research area of fluid mechanics in biomedical applications, there is a shift of focus from single- to multi-modality studies. Integrating data (namely *in vivo*, *in vitro*, and *in silico* datasets) is one of the recommended approaches for validating numerical results and providing comprehensive hemodynamic assessments [3]. To date, only one multi-modality study has performed a comparison of WSS obtained by *in vivo* 4D-Flow MRI, CFD, and *in vitro* STB techniques under pulsatile condition [24]. However, the high cycle-to-cycle flow variations under pulsatile flow can cause large differences in flow measurements between different modalities [25], which will amplify the variations

in velocity-derived parameters. To further bridge this gap and exclude the cycle-to-cycle hemodynamic variations, we investigated hemodynamics in a patient-specific intracranial aneurysm under steady flow conditions using a multi-modality approach. We compared the steady flow results of PIV (Tomo-PIV, Stereo-PIV) and CFD to the peak systole measurement of *in vivo* 4D-Flow MRI. The geometry for PIV and CFD models was based on the 4D-Flow MRI velocity field. Steady-state PIV and CFD studies were performed with inlet flow based on *in vivo* 4D-Flow MRI at peak systole. In this study, we presented the similarities and differences in velocity field, vortex, and WSS distributions obtained by 4D-Flow MRI, Stereo-PIV, Tomo-PIV, and CFD.

## 2.2. METHODS

### 2.2.1. PC-MRI SETUP

The patient-specific intracranial aneurysm (Fig. 2.1) is located at the right middle cerebral artery (RMCA) of the Circle of Willis (CoW). The geometry was reconstructed from the 4D-Flow 7T MRI scans performed at the Academic Medical Center in Amsterdam. The patient (man, 65 years old) underwent a 4D-Flow MRI examination on a 7T MRI scanner (Achieva, Philips Healthcare, Cleveland, USA) that was retrospectively gated with a peripheral pulse unit. The overall scan time of the PC-MRI measurement was approximately 15 minutes. The sequence is the same as in Ref. [26]. The acquired spatial resolution was  $0.47 \times 0.47 \times 0.5 \text{ mm}^3$  and the echo time, repetition time and the flip angle were 3.1 ms, 6.8 ms and  $20^\circ$ , respectively. Velocity encoding was 150 cm/s in the x, y, and z directions. The number of reconstructed cardiac phases was 9, resulting in a temporal resolution of 82 ms at an average heart rate of 81 beats/minute. The scan was accelerated with a SENSE factor of 3 in the right-left direction. Phase images were corrected for concomitant field and eddy current related phase offsets. The lumen of the intracranial aneurysm was semi-automatically segmented using commercial software (Mimics, Materialise, Leuven, Belgium) [8]. From now on, we will refer to the *in vivo* 4D-Flow MRI data as MRI for short.

### 2.2.2. PREPARATIONS FOR *In vitro* AND *In silico* MODELS

Before being applied to PIV and CFD studies, the segmented raw surface was processed using Vascular Modelling Toolkit (VMTK). Firstly, we applied Taubin smoothing with passbands of 0.45 and 100 iterations. Afterward, the geometry was clipped at the inlet and outlet of the aneurysm to open the inlet/outlet. Flow extensions and caps were subsequently added to the inlet and the outlet. At this stage, the resulting surface (STL) (Fig. 2.1b) was ready for numerical meshing. For PIV experiments, the STL surface was scaled up 3.77 times to increase the spatial resolution (Fig. 2.1c). Moreover, the outlet vessel was further extended for the convenience of PIV phantom manufacturing (Fig. 2.1c). The PIV phantom (Fig. 2.1f) was constructed by the lost core casting technique. More specifically, a transparent aneurysm phantom was made by casting a removable mould of the aneurysm lumen with PDMS (Polydimethylsiloxane) liquid (Fig. 2.1e). The mould was a 3D ABS (Acrylonitrile Butadiene Styrene) print fabricated by Fortus 450MC (Stratasys, Israel) machine with a layer resolution of 0.127 mm (Fig. 2.1d). Once the PDMS had cured, the mould was dissolved by acetone.

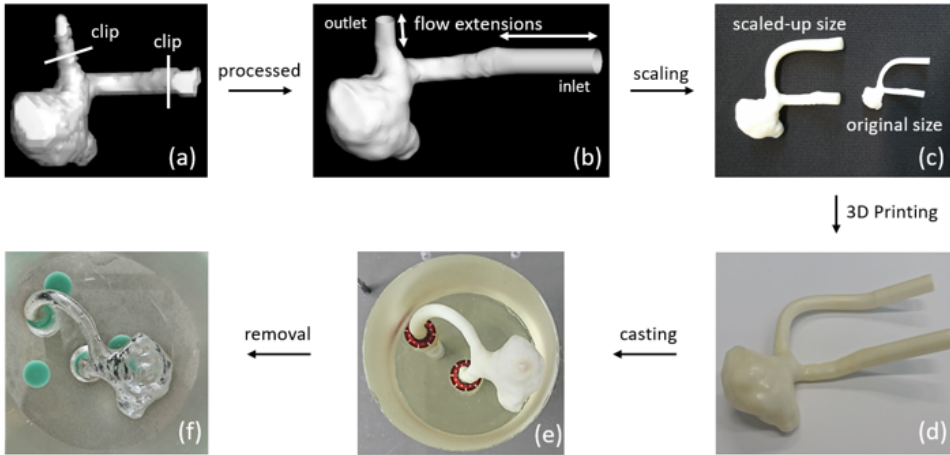


Figure 2.1: (a) Segmented raw surface from *in vivo* 4D-Flow MRI. (b) Processed surface for *in silico* CFD model. (c) Scaling up the geometry for *in vitro* PIV model (Note: for the convenience of casting, the outlet was further extended for *in vitro* PIV model). Manufacturing steps of the PIV phantom: (d) the 3D rapid prototyping printed mould, (e) the mould casted with PDMS, (f) the PDMS phantom with mould removed.

### 2.2.3. PIV SETUP

#### FLOW LOOP

The experiment was conducted under the steady flow condition, which corresponded to the averaged peak systole of 9 cardiac cycles measured by 4D-Flow MRI *in vivo*. To ensure dynamic similarity, the characteristic inlet Reynolds number ( $Re = 350$ ) was imposed. The working fluid in PIV studies is a mixture of water-glycerol with a measured density (DMA 4100 M, Anton Paar, Austria) of  $\rho = 1147 \text{ Kg/m}^3$  and dynamic viscosity of  $\mu = 0.008113 \text{ Pa}\cdot\text{s}$  at  $25^\circ$ . The water-glycerol mixture recipe was chosen to reduce the optical distortion at the interface of working fluid and PDMS phantom. By changing the water/glycerol concentration, the refractive index ( $n = 1.4107$ , Bleeker Zeist Holland refractometer) was matched with that of the PDMS phantom to achieve no visible refraction.

The flow circulation in the aneurysm was driven by a diaphragm fluid pump (NF 1.600 KPDC, KNE, Germany) (Fig. 2.2). A thermostat tank was used to keep the temperature of the working fluid at  $25^\circ$ . The flow rate was controlled and monitored by an electromagnetic flowmeter (Mini Cori-Flow<sup>TM</sup> MT5, Bronkhorst, the Netherlands) and a control valve (F-004AC/AI (NC), Bronkhorst, the Netherlands). The inlet flow of PIV experiments measured by the flowmeter was compared to the averaged peak flow measured with 4D-Flow MRI. The resulted Reynolds numbers in Stereo-PIV and Tomo-PIV measurements were 327 and 335, which deviated 6.6% and 4.3% from 4D-Flow MRI ( $Re = 350$ ), respectively.

#### IMAGING SYSTEM

The optical setup of Stereo-PIV and Tomo-PIV used two high-speed CMOS cameras ( $2016 \times 2016$  pixel, 12 bit, Imager pro-HS 4M, LaVision Inc, England). In Stereo-PIV, fluorescent dyed polystyrene particles with a diameter of  $25 \mu\text{m}$  and density of 1100

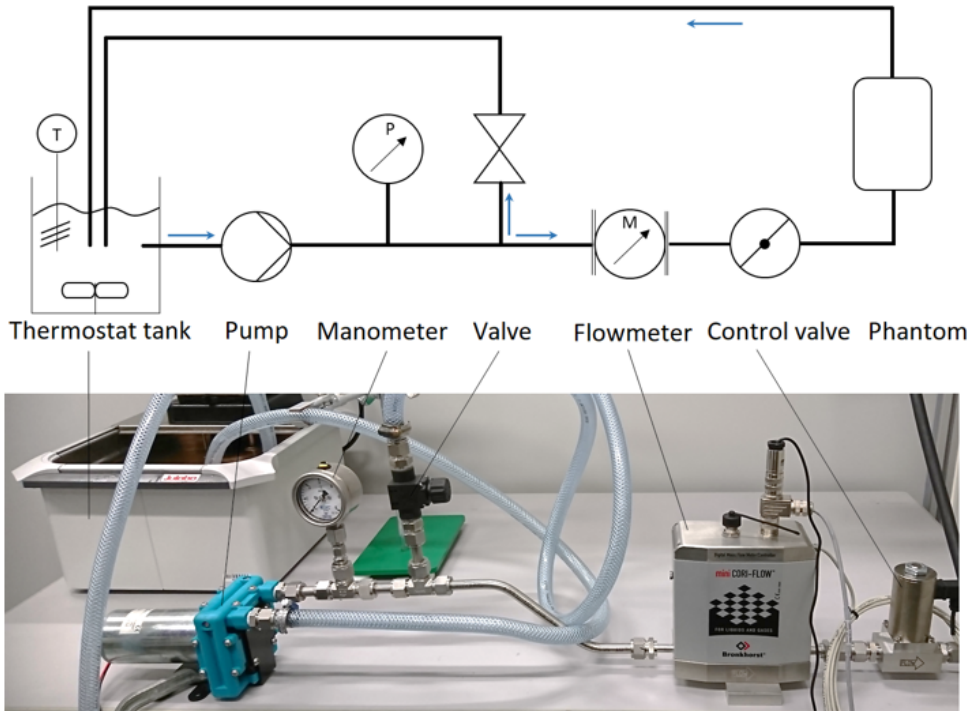


Figure 2.2: Schematic representation and a photo of constructed flow circulation system.

$\text{Kg/m}^3$  was seeded in the flow. In Tomo-PIV, the flow field was seeded with a diameter of  $25\text{--}50\ \mu\text{m}$  and density of  $1100\ \text{Kg/m}^3$  fluorescent Rhodamine-B coated PMMA particles. A volume of approximately  $48 \times 70 \times 50\ \text{mm}^3$  was illuminated by a double pulsed Nd:YLF laser (IDY304, Litron Lasers, England) with the applied laser energy of 27 mJ. A wavelength cut-off filter was equipped on the camera lens to block the laser light. The aneurysm phantom was placed in Plexiglas tanks containing a water-glycerol mixture with the same refractive index of the phantom (Fig. 2.3). This design of the multi-window tank was to ensure that camera views were orthogonal to the liquid-air interface, reducing optical distortions. For the Stereo-PIV setup, the cameras were arranged in an angular configuration of  $90^\circ$  (Fig. 2.3). For the Tomo-PIV setup, a mirror system was introduced to create four different views with two cameras. Each camera sensor was split into the left and right half to record two different views. In total, four views were linearly arranged in a horizontal plane with an aperture angle of  $108^\circ$  (Fig. 2.3). The Plexiglas tanks were mounted on a micrometer slider with an accuracy of  $\pm 0.02\ \text{mm}$  (LES4, Isel Germany AG, Eichenzell, Germany), which facilitates the accurate translation of calibrated and measured planes in the z-direction (perpendicular to the laser sheet). Stereo-PIV measurements were taken at 50 parallel planes with a shift of 1 mm to cover the whole aneurysm. In the Tomo-PIV experiment, the entire aneurysm flow field was illuminated and measured at once.

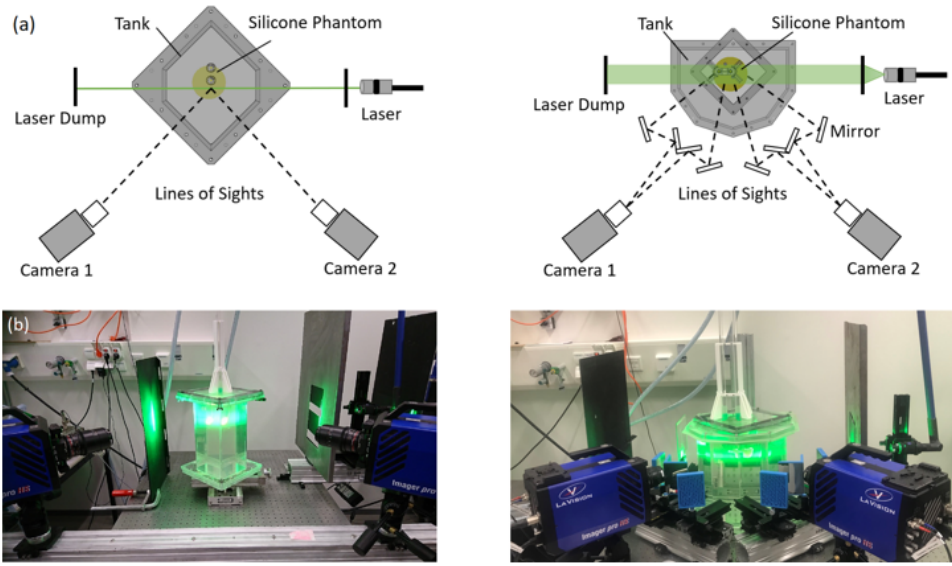


Figure 2.3: Schematic representation and a photo of constructed flow circulation system.

### CALIBRATION AND PIV ANALYSIS

Camera calibrations were performed with a two-level calibration plate placed inside the tank filled with refractive index-matched working fluid. For Tomo-PIV, calibration images at 7 positions equally spaced over 35 mm were taken and used for volumetric calibration along the  $z$ -direction. For Stereo-PIV, calibration was done for each measurement plane. A third-order polynomial fitting method was applied to map the 3D world position to the camera sensor plane. This yielded an error of approximately 0.2-0.4 pixel for all views in Tomo-PIV. The volume self-calibration, based on the particle images taken for velocity field calculations, reduced the calibration error to 0.1 pixel, which was necessary for accurate Tomo-PIV reconstruction [27]. Before the volume self-calibration, the image pre-processing of subtracting an average time filter was applied to exclude any tracing particles which stick to the wall. For stereo-PIV, additional self-calibration was also performed to correct misalignment between the calibration plate and the laser sheet.

Before cross-correlation, manual geometric masks were created in all particle images to remove the non-flow regions. Due to the Gaussian laser illumination shape, the masked images were then pre-processed firstly with an intensity normalization filter, subsequently with Gaussian smoothing ( $3 \times 3$ ) and sharpening. In the Stereo-PIV analysis, the cross-correlation started with 2 passes at window size  $48 \times 48$  pixel with 50% overlap and rectangular weight. Then it was followed by 3 passes decreased window size  $12 \times 12$  pixel with 75% overlap using a circular weight. The resulting final spatial resolution was  $0.144 \text{ mm}^2$ . In the Tomo-PIV analysis, the 3D correlation were performed iteratively with 6 steps and with 2 passes in each step. It started with window size  $96 \times 96 \times 96$  voxel (75% overlap) and then deformed to a 2 times smaller window size in the following each time step. The final interrogation window size was  $16 \times 16 \times 16$  voxel with 75% overlap, resulting

in a spatial resolution of  $0.25 \text{ mm}^3$ . All vector fields were post-processed by a median filter ( $5 \times 5$ ) for the outlier detection, removal, and replacement. In addition, parts with a correlation value of  $< 0.8$  were removed. The removed parts were filled up by averaging 100 vector fields. The PIV processing was performed using DAVIS 10.0.5. The 2D velocity results of Stereo-PIV were extended to 3D by interpolating the velocity vectors on 50 planes into a rectangular field.

#### 2.2.4. CFD SIMULATIONS

The CFD simulations were carried out with the finite-volume code ANSYS Fluent 17.1 (Ansys Inc., Canonsburg, PA, United States). The STL geometry was meshed using the ICEM CFD (Ansys Inc., Canonsburg, PA, United States). To properly resolve the boundary layer, the mesh in the proximity of the wall was composed of 12 layers of flat polyhedral elements, with a first-layer thickness of 0.05 mm and an exponential growth rate of 1.2. In the central part of the domain, polyhedral elements were applied. In total, the mesh contained 0.8 million polyhedral cells. The mean WSS difference between this and a finer mesh of 2.25 million cells simulations was less than 1% confirming that our results are sufficient to obtain grid-independent solutions. Blood was modelled as a Newtonian fluid with a density of  $1060 \text{ Kg/m}^3$  and a dynamic viscosity of  $0.0035 \text{ Pa}\cdot\text{s}$ . A rigid wall with no-slip conditions was assumed at the aneurysm wall. The steady flow simulation was performed by solving the incompressible 3D Navier-Stokes equations with the solver settings in Table 1. A parabolic velocity profile was imposed at the inlet and the outlet was set to the outflow boundary condition, with a zero diffusion flux for all flow variables.

Table 2.1: The CFD solver (ANSYS/ Fluent) settings.

Settings	Method/Value
Physics solver	pressure based
Momentum Gradient	Second-order upwind Least square cell-based
Velocity/pressure coupling	SIMPLE
Convergence criterion	$10^{-6}$

#### 2.2.5. CALCULATION OF WALL SHEAR STRESS

WSS was estimated by mapping the velocity gradient from the measured/simulated data to the STL surface grids. As mentioned previously, the STL surface was based on MRI velocity field with a resolution of  $0.47 \times 0.47 \times 0.5 \text{ mm}^3$ . The unit inward normal vectors at each surface point were calculated. The velocity gradients obtained by each modality were mapped from the measured fields to the aneurysm surface by inversed-distance weighted interpolation. The value at each surface point was weighted by a function of the distance between each measured data point to the surface data point. The WSS vectors were computed as:

$$\vec{\tau} = 2\mu\dot{\epsilon}_{ij} \cdot \vec{n} \quad (2.1)$$

where  $\vec{\tau}$  is WSS vectors,  $\vec{n}$  is the surface unit normal vectors,  $\dot{\epsilon}_{ij}$  rate of deformation tensor, which is calculated as

$$\dot{\epsilon}_{ij} = \frac{1}{2}(\partial_j v_i + \partial_i v_j) \quad (2.2)$$

where indices  $i, j = [1-3]$  are for the 3 Cartesian (x-y-z) coordinates. In the three-dimensional coordinate system, the WSS vectors were calculated as:

$$\vec{\tau} = \begin{bmatrix} \tau_x \\ \tau_y \\ \tau_z \end{bmatrix} = \mu \begin{bmatrix} 2n_x \frac{\partial v_x}{\partial x} + n_y \left( \frac{\partial v_y}{\partial x} + \frac{\partial v_x}{\partial y} \right) + n_z \left( \frac{\partial v_z}{\partial x} + \frac{\partial v_x}{\partial z} \right) \\ n_x \left( \frac{\partial v_x}{\partial y} + \frac{\partial v_y}{\partial x} \right) + 2n_y \frac{\partial v_y}{\partial y} + n_z \left( \frac{\partial v_z}{\partial y} + \frac{\partial v_y}{\partial z} \right) \\ n_x \left( \frac{\partial v_x}{\partial z} + \frac{\partial v_z}{\partial x} \right) + n_y \left( \frac{\partial v_y}{\partial z} + \frac{\partial v_z}{\partial y} \right) + 2n_z \frac{\partial v_z}{\partial z} \end{bmatrix} \quad (2.3)$$

where  $\tau_x, \tau_y, \tau_z$  are the WSS components in the x-, y- and z-direction, while  $n_x, n_y, n_z$  are corresponding unit wall normals. The WSS calculation method was validated against the analytical solution at the inlet where the flow was parabolic. The error was below 20% for PIV experiments. This error should have included the uncertainties propagated by PIV measurements, the uncertainty of wall location and the bias in velocity gradient interpolation.

## 2.3. RESULTS

### 2.3.1. COMPARISON OF FLOW PATTERNS

In PIV experiments, the aneurysm size was scaled up and a matched Reynolds number was imposed at the inlet, which ensured similar flow patterns to MRI flow. Consequently, the inflow velocity varied from that of MRI. In order to exclude the impact of varied inflow velocity across modalities, we normalized the velocity with the maximum velocity of the inlet ( $V_{ref}$ ) during comparison of the flow field.

The global flow structure obtained by each modality was examined first. The streamlines generated from Tomo-PIV, Stereo-PIV, MRI, and CFD data are shown in Fig. 2.4a. They are coloured with normalized velocity magnitude. It can be seen that all modalities show the following flow patterns: the inflow forms a wall impingement region and generates bifurcating flow at the neck of the aneurysm; a part of the flow goes directly to the outlet, while the rest of the flow forms a jet that enters the aneurysm sac. We observed discrepancy in the aneurysm core: helical outflow in PIV and CFD results is not detected by MRI.

### 2.3.2. COMPARISON OF VELOCITY FIELD

The detailed comparisons of the measured and predicted velocity fields were performed next. The iso-surface of normalized velocity magnitude is shown in Fig. 2.4b. The selected value of normalized velocity iso-surface ( $V/V_{ref} = 0.3$ ) captures nicely the jet inflow and gives a similar shape for all modalities. Almost identical results were achieved between the Tomo-PIV and CFD. The MRI shows a slightly smaller recirculation angle of the jet inflow. This is commonly found in MRI acquisition due to displacement artefacts.

Two characteristic cross-sections along the z-coordinate direction (as indicated in (Fig. 2.5a) were selected to conduct a comparison of velocity magnitude among all modalities.

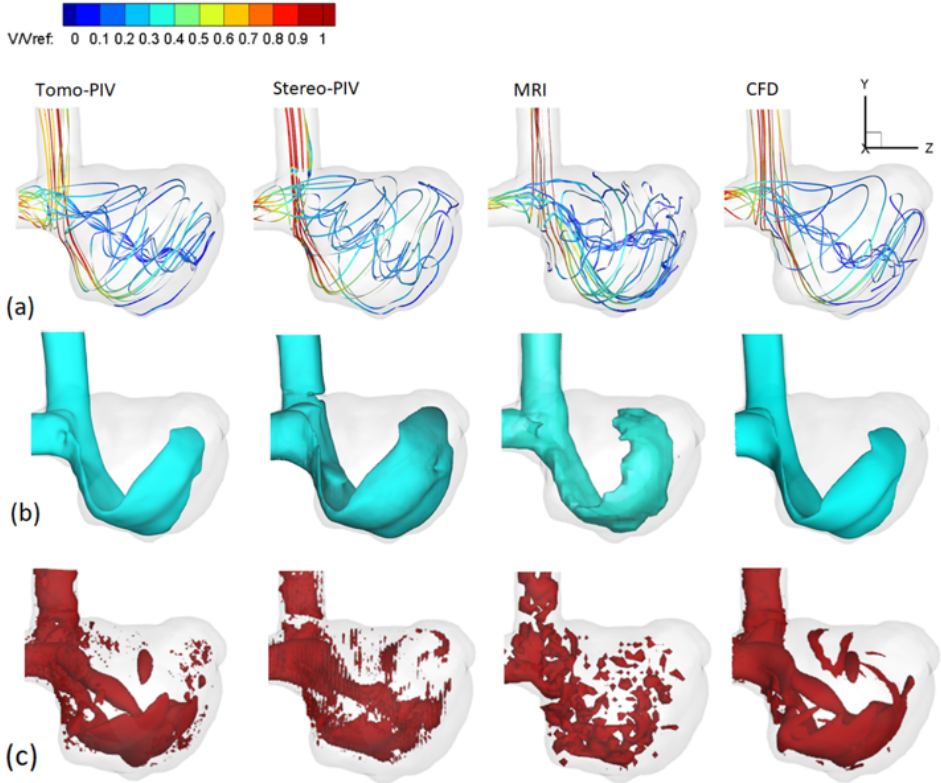


Figure 2.4: (a) Comparison of streamlines coloured by normalized velocity magnitude acquired by Tomo-PIV, Stereo-PIV, MRI and CFD. (b) Iso-surface of normalized velocity magnitude ( $V/V_{ref} = 0.3$ ) from all modalities. (c) Comparison of 3D vortex structures identified by Q-criterion and visualized with the selected iso-surface ( $Q = 9000 \text{ 1/s}^2$ ).

The contours of normalized velocity magnitude in two selected planes are shown in Fig. 2.6a. It can be seen that a good agreement is obtained between both PIV experiments and CFD. The MRI underestimated the velocity magnitude in the aneurysm core region, where the flow is stagnant and severely distorted. This may be due to the limited resolution of MRI acquisition or measurement errors in those voxels.

To provide a quantitative comparison, profiles of the velocity magnitude along selected horizontal and vertical lines (A and B, as indicated in Figs. 2.5b and 2.5c) were extracted in specified cross-sections (Fig. 2.5a) and shown in Fig. 2.7a. The corresponding Pearson correlation coefficients are given in Table 2.2. The velocity profiles exhibit similar trends at both locations for all modalities. Compared to the PIV and CFD, the MRI gives underestimated values of the peak velocity at the 1-A and 1-B locations (see in Fig. 2.7a-top). The calculated Pearson correlation coefficients ( $\rho$ ) of selected profiles show a good agreement between the Tomo-PIV and CFD of  $0.95 < \rho_{1D} < 0.98$ . The correlation coefficient is lower for the MRI versus CFD comparison, showing a correlation of  $\rho_{1D} > 0.67$  for most profiles, with the exception of profile 1-B where the MRI significantly

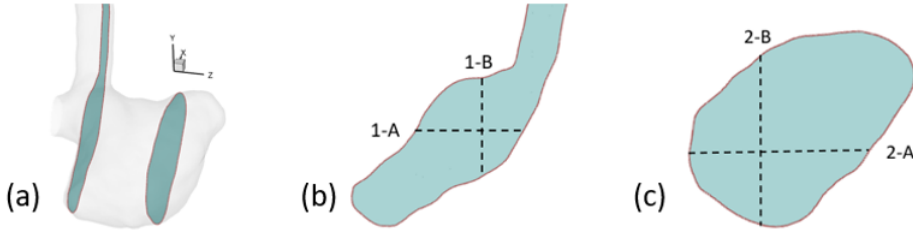


Figure 2.5: (a) Positions of characteristic 2D cross-sections used for a detailed comparison. (b) and (c) Locations of specific horizontal and vertical lines in the selected cross-sections: (b) 1-A and 1-B, (c) 2-A and 2-B.

underestimated the jet peak value.

A Bland-Altman analysis was performed to present differences in normalized velocity at the selected planes. To exclude the influence of the spatial resolutions, PIV and CFD datasets were down-sampled to match the MRI resolution by bilinear interpolation. The results are shown in Fig. 2.7b. It can be seen that the spread of data points was relatively symmetric, and no significant proportional relationship was found between difference and mean values. The mean differences in all Bland-Altman plots are close to 0. The mean differences between MRI and Tomo-PIV are the lowest which is 0.001 and -0.0003 in the first and second plane, respectively.

Table 2.2: Pearson correlation coefficients ( $\rho$ ) of different methods for velocity magnitude profiles along specific lines in characteristic cross-sections shown in Fig. 2.5.

Location	1-A	1-B	2-A	2-B
Tomo-PIV-CFD	0.98	0.95	0.95	0.96
Stereo-PIV-CFD	0.93	0.98	0.79	0.91
MRI-CFD	0.80	0.44	0.71	0.67

### 2.3.3. COMPARISON OF VORTICITY

To further evaluate the ability of different modalities in capturing the 3D flow, the vorticity and Q-criterion (the second invariant of the velocity-gradient tensor) as the vortex detection methods were analysed next. To make the out-of-plane vorticity comparable, we scaled the vorticity level by the average velocity and the vessel size at the inlet:

$$\omega_z = \left( \frac{\partial u_y}{\partial x} - \frac{\partial u_x}{\partial y} \right) \times \frac{u_{MRI}}{u_{PIV}} \times \frac{d_{PIV}}{d_{MRI}} \quad (2.4)$$

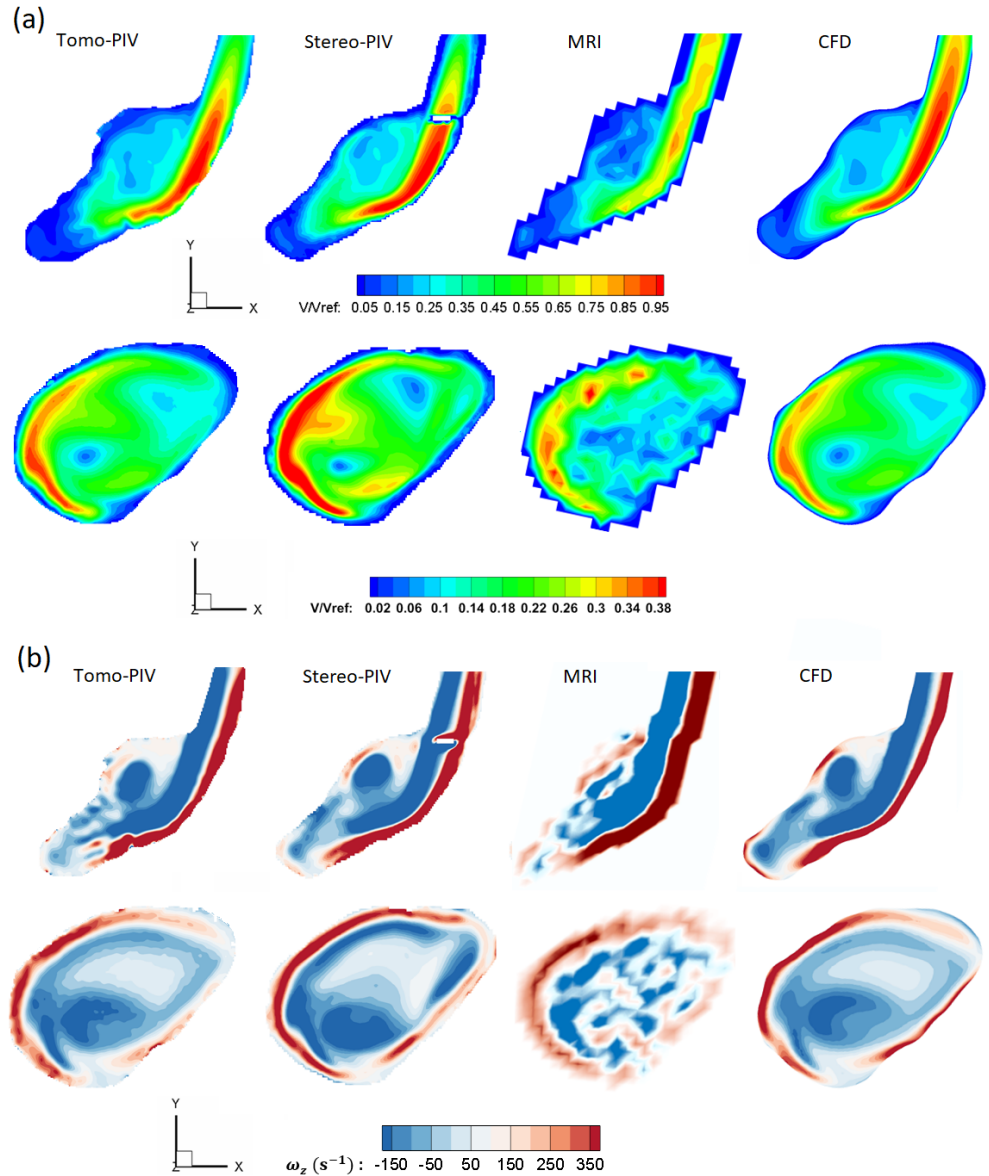


Figure 2.6: (a) Contours of the normalized velocity magnitude, and (b) contours of the out-of-plane vorticity component in characteristic cross-sections shown in Fig. 2.5a for all modalities. Note: the white area in the stereo-PIV measurements is due to missing data points, the cause was a trapped air bubble.

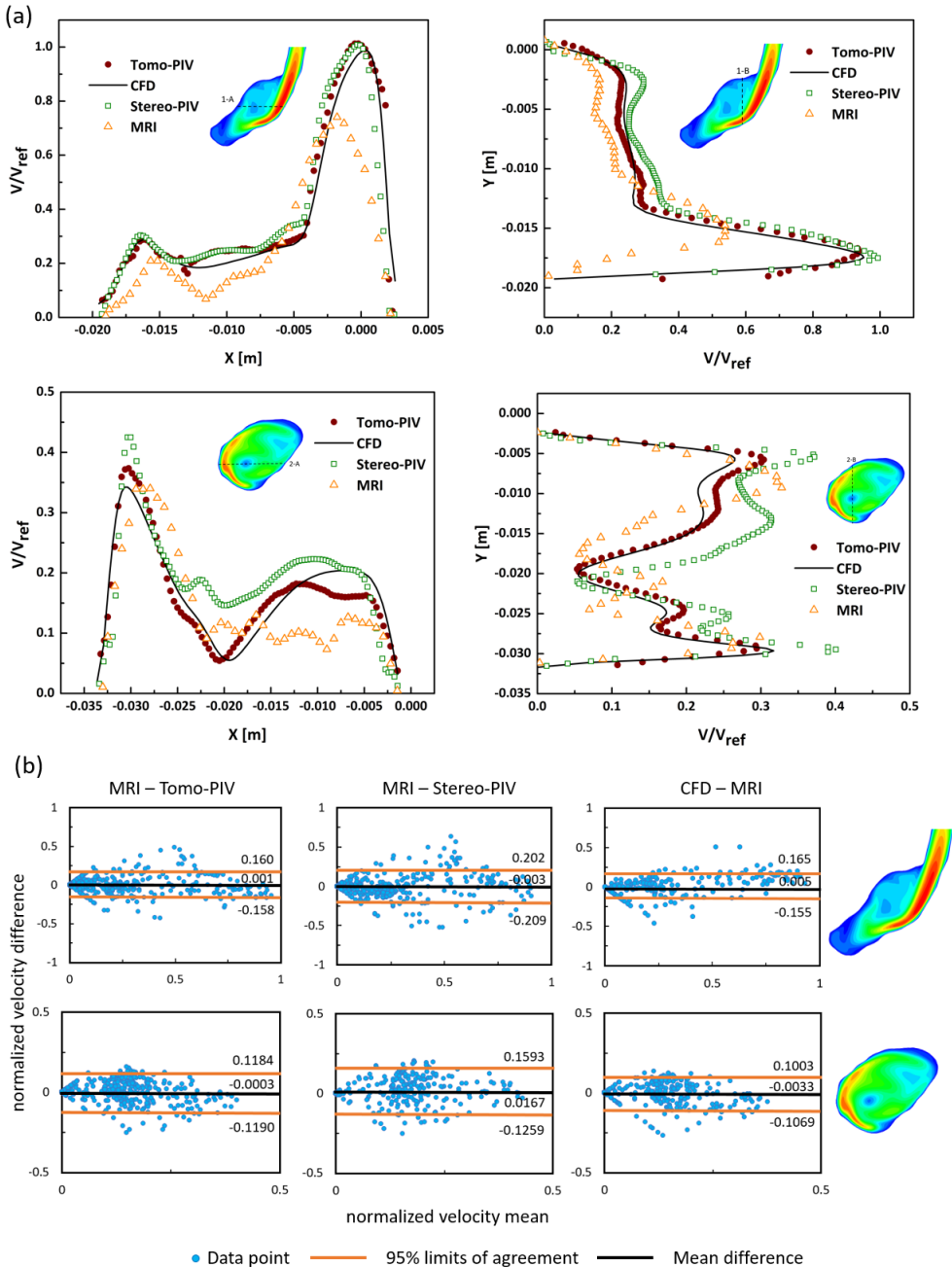


Figure 2.7: (a) Comparison of Tomo-PIV, Stereo-PIV, MRI and CFD velocity profiles along specific lines in characteristic cross-sections shown in Figs. 2.5a-c. (b) Bland-Altman plots of normalized velocity magnitude in two cross-sections, comparing MRI to down-sampled Tomo-PIV, Stereo-PIV and CFD datasets. The 95% limits of agreement were equal to 1.96 SD (where SD is the standard deviation).

Fig. 2.4c shows the Q-criterion iso-surface and Fig. 2.6b shows the contours of the out-of-plane vorticity component of all modalities. Again, a good qualitative agreement is obtained between PIV and CFD. The coherent structures developed by the wall jet and helical outflow are clearly captured by PIV and CFD results. Clear discrepancies observed in MRI are: distributions appear less smooth due to lower spatial resolution; the formation of the vortex in the outflow tract was not detected in MRI data.

2

### 2.3.4. COMPARISON OF WALL SHEAR STRESS

As mentioned previously, there was a variation of fluid viscosity, inflow velocity, and vessel size between PIV experiments and MRI/CFD. To compare WSS quantitatively, we scaled the WSS level by:

$$WSS = \tau \times \frac{\mu_{MRI}}{\mu_{PIV}} \times \frac{u_{MRI}}{u_{PIV}} \times \frac{d_{MRI}}{d_{PIV}} \quad (2.5)$$

Note that the same method described in section 2.2.5 and the original spatial resolution of each modality were used for the WSS calculation. For qualitative comparison, the WSS magnitude was normalized by the WSS at the parent vessel of each modality. Figure 8a illustrates the normalized WSS distribution at the aneurysm surface by all modalities. The normalized WSS patterns show a qualitatively reasonable agreement between various modalities. The local distribution of the WSS can be associated closely with the characteristic near-flow structures in the proximity of the wall. The high WSS regions occur along with the inflow jet, whereas the lower WSS regions are present in the rest of the aneurysm wall. In all modalities, the WSS value at the aneurysm neck is more than twice higher than the one in the sac.

Table 2.3 gives the mean (spatially averaged) and peak absolute WSS magnitude of all modalities. It can be seen that CFD predicts the highest values among all modalities, with peak WSS of 17.91 Pa and averaged WSS of 2.15 Pa. Absolute WSS based on MRI velocity field is over two times smaller than PIV and CFD estimations, which can be attributed to the lower spatial resolution of MRI [8]. The PIV techniques also produce lower values than CFD does, but the differences are less significant. Figure 2.8b shows the Bland-Altman plots comparing the WSS magnitude derived from Tomo-PIV, Stereo-PIV, CFD to that derived from *in vivo* MRI. The mean difference is 1.27 Pa, 0.96 Pa, 2.11 Pa for Tomo-PIV, Stereo-PIV, and CFD, respectively. The 95% limits of agreement is  $\pm 3.80$  Pa,  $\pm 3.64$  Pa, and  $\pm 5.79$  Pa for Tomo-PIV, Stereo-PIV, and CFD, respectively. For all modalities, the difference increases when the WSS magnitude is higher.

Table 2.3: Mean and maximum WSS in Tomo-PIV, Stereo-PIV, MRI, and CFD.

WSS(Pa)	Tomo-PIV	Stereo-PIV	MRI	CFD
Maximum	17.73	9.32	3.99	17.91
Mean	1.75	1.56	0.94	2.15

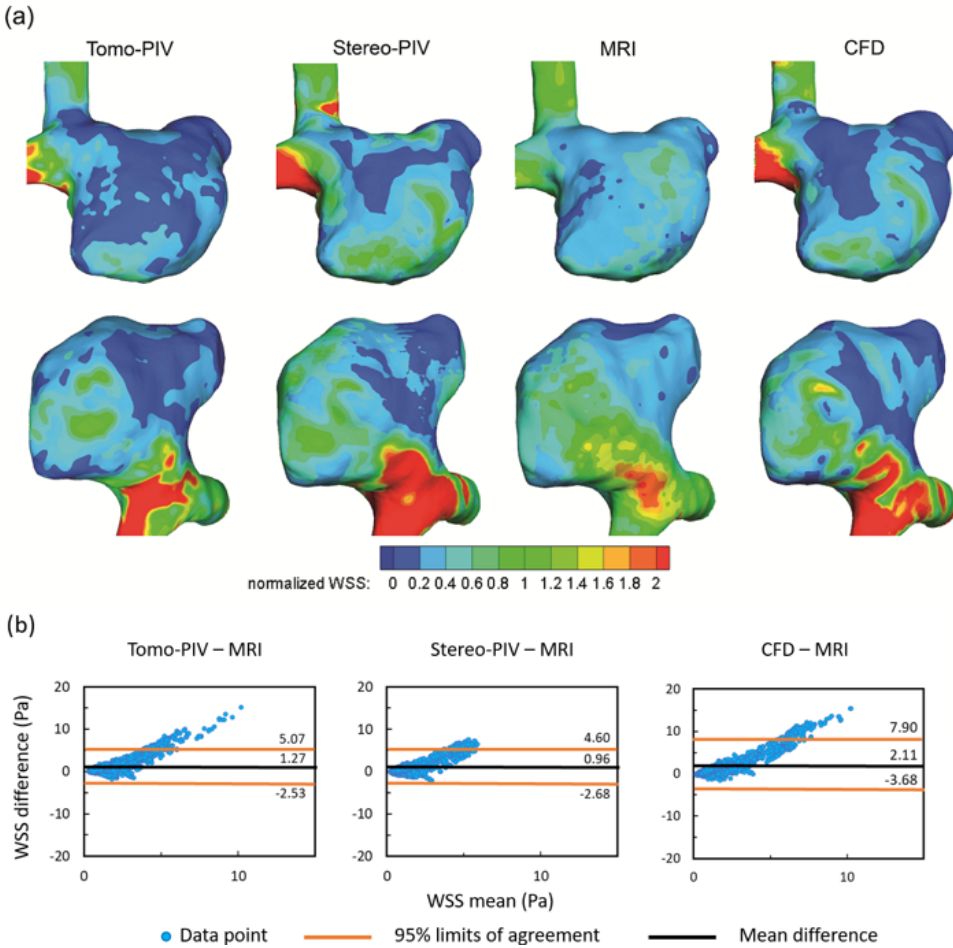


Figure 2.8: (a) Comparison of normalized WSS distribution between Tomo-PIV, Stereo-PIV, MRI and CFD results. (b) Bland-Altman plots of absolute WSS values, comparing MRI to Tomo-PIV, Stereo-PIV and CFD. The 95% limits of agreement were equal to 1.96 SD (where SD is the standard deviation).

## 2.4. DISCUSSION

The association of WSS and its derivatives with the progression and ultimate rupture of intracranial aneurysms has become a growing interest. In the literature, the WSS studies heavily rely on clinical imaging techniques and CFD simulations. An alternative and increasingly popular technique is Tomo-PIV. Several studies have applied Tomo-PIV in assessing WSS in vitro because it can measure the velocity in a volumetric and high-resolution manner [21], [25]. Given that each modality has its strong and weak points, combining data obtained from different modalities has been proposed in order to ensure the reliability of the results and to help the realization of hemodynamic analysis in clinical decision-making [3]. In this work, we conducted a multi-modality study based on a

patient-specific intracranial aneurysm. The velocity field, vorticity, and WSS magnitude were compared between Tomo-PIV, Stereo-PIV, *in vivo* 4D-Flow MRI, and CFD. The results reveal that all modalities can capture the flow characteristic of a high-velocity inflow jet and its accompanying vortex ring structure which recirculates the flow towards the upper part of the aneurysm. MRI shows a slightly smaller recirculation angle compared to other techniques. This is commonly found in MRI acquisition due to displacement artefacts [28]. Regarding the velocity field and vorticity, a good agreement was obtained between CFD and PIV measurements (Fig. 2.6, Fig. 2.7). However, MRI displays some clear discrepancies. Compared to CFD and PIV, the velocity magnitude by MRI is smaller in both fast and slow flow areas, and the coherent vortex structure in the core region of the aneurysm (Fig. 2.4c) is absent. When we down-sampled resolutions of CFD and PIV to that of MRI, the discrepancies have greatly reduced, as can be seen in Fig. 2.7b. This demonstrates that spatial resolution plays an essential role in causing discrepancies of the velocity magnitude among modalities. This notion is consistent with Ref. [29], which also concluded that PC-MRI leads to systematic underestimation of overall velocity magnitude, and resolution is its major contributor.

The overall normalized WSS distribution shows similar patterns (Fig. 2.8a) across different modalities. The WSS level elevates at the inflow jet, its impingement, and its recirculating regions. From Fig. 2.8a, we can see that MRI shows a larger area (green) of elevated WSS at the inflow jet tract, which may imply a more diffused inflow compared to CFD and PIV. Quantitatively, the absolute WSS exhibits significant variations across different modalities (Table 2.2). The CFD predicts the highest WSS magnitudes (peak 17.91 Pa, mean 2.15 Pa). The MRI estimated WSS magnitude (peak 3.99 Pa, mean 0.94 Pa) is around 2- to 4-fold lower than CFD and Tomo-PIV calculations, and around 2-fold lower than Stereo-PIV calculations. It has been previously reported that WSS magnitude based on MRI measurement is underestimated compared with CFD. The mean WSS of a patient-specific aneurysm was around 2 to 3 times lower for MRI measurement than in CFD simulation as reported in Ref. [8]. In Ref. [30], CFD gave 1.63 times higher WSS magnitude than MRI did in 5 patient-specific aneurysm studies. Similar to this study, Natito et al. [31] found that MRI greatly underestimated WSS in a study of 15 patients with intracranial aneurysms—5 times lower than the value based on CFD. The degree of MRI-based WSS underestimation is dependent on the actual WSS [32]. The higher WSS is, the more the underestimation is. The proportional trend observed in the Bland-Altman plots (Fig. 2.8b) confirmed this. The Bland-Altman comparisons in absolute WSS (Fig. 2.8b) indicate a higher agreement of PIV versus MRI than that of CFD versus MRI. The mean difference and 95% limits of agreement of CFD versus MRI is the largest compared with those of Tomo-PIV/Stereo-PIV versus MRI. Studies have shown that spatial resolution is the most significant factor in the velocity and WSS estimation [8], [32]. As Fig. 2.7b shows, no proportional difference of velocity is found when comparing down-sampled PIV and CFD datasets with MRI. Therefore, we believe that the difference in spatial resolution is the main reason for the discrepancies in the velocity and WSS magnitude between modalities in this study.

In this study, we found that even with a lower in-plane spatial resolution comparing to Stereo-PIV, Tomo-PIV provides a higher WSS estimates and shows better agreement with CFD in velocity field. This could be due to the 4 times higher spatial resolution of

Tomo-PIV in the depth direction. For Stereo-PIV, the voxel size in the depth dimension is determined by the thickness of the laser sheet (1 mm in this study). Thus, the averaging effect is severe with low-resolution in the depth direction. It was reported that MRI with a voxel size of 1 mm underestimated WSS by 40% in a noise-free numerical simulation of parabolic flow [33]. We can conclude that the inherently three-dimensionality of Tomo-PIV makes it a preferred technique over Stereo-PIV in hemodynamic investigations, especially when considering pulsatile flow studies. It is very time-consuming to perform volume reconstruction on multiple planes of Stereo-PIV measurement at each time step of the pulsatile cycle.

Several assumptions made in the current PIV and CFD studies, namely the Newtonian viscosity of blood and rigid vessel wall assumptions, could also be associated with the discrepancies. Some numerical studies have reported that neglecting the Non-Newtonian effect of blood and fluid-structure interactions can lead to overestimation of WSS magnitude [34], [35]. Only a few comparative experiments studied the impact of fluid-structure interactions on hemodynamics. These experiments were based on rigid and compliant straight vessels and utilized the 2D PIV technique [36], [37]. Further experimental data based on patient-specific geometries, non-Newtonian fluid solution, and 3D techniques are required to validate the simulation models. In the current study, the inflow boundary conditions in PIV and CFD are steady, which varies from *in vivo* MRI flow condition. However, we also performed unsteady-state PIV experiments and CFD simulations by imposing a patient-specific waveform at the inlet (see results presented in the Online Resource). The results show that the velocity and WSS distribution at the peak systole are similar to the steady-state. The difference in time-averaged WSS between steady and pulsatile flow condition was studied in Ref. [38] and less than 5% difference was reported. In Ref. [39], steady flow conditions gave lower maximum WSS estimations than pulsatile flow conditions did in a CFD study of 210 cerebral aneurysms. Therefore, we conclude that the imposed steady-state should not be the reason that PIV and CFD predicted higher WSS than MRI measurements. In this study, a rigid transformation was performed in order to compare different datasets. The translational misalignment of coordinate systems can contribute to the qualitative but not quantitative variations of velocity field and WSS among modalities. Further investigation by comparing to more advanced technique such as imaging registration is needed to quantify the impact of geometry mismatch caused by the rigid transformation. In addition, in future work, a combination of compliant model, non-Newtonian fluid, and pulsatile flow condition could bring the *in vitro* and *in silico* studies closer to the real *in vivo* cases.

## 2.5. CONCLUSION

We have performed a comparison study of flow and WSS in a patient-specific intracranial aneurysm through *in vivo* 4D-Flow MRI, *in vitro* PIV (Stereo-PIV and Tomo-PIV), and *in silico* CFD. Our results demonstrated a good agreement in the flow pattern, velocity, and vorticity between PIV and CFD modalities. However, MRI-based velocity is smaller than velocity based on other techniques in both fast and slow flow areas. The comparison of down-sampled PIV and CFD data to MRI resolution indicates that spatial resolution is the main contributor to the discrepancy. Qualitative agreement in WSS was found across all modalities, but there is a large variation in the absolute WSS values. We observed that

the MRI-based WSS magnitude is significantly lower than those based on PIV and CFD. We also found that with a higher out-of-plane spatial resolution, Tomo-PIV gave a higher WSS and better velocity agreement with CFD than Stereo-PIV did. This confirms that spatial resolution plays an important role in the underestimation of WSS. However, the impacts of non-Newtonian viscosity and the compliant wall on WSS should be assessed through *in vitro* experiments in future studies.

### APPENDIX A: COMPARATIVE ASSESSMENT OF THE FLOW UNDER STEADY AND PULSATING INFLOW CONDITIONS AT PEAK SYSTOLE

We have performed additional set of experiments and numerical simulations by imposing the patient-specific pulsating inflow conditions (Fig. 2.9) too. The obtained results are presented in this appendix. Comparisons of the velocity magnitude (Fig. 2.10), wall shear stress distribution (Fig. 2.11), and Bland-Altman analysis of WSS (Fig. 2.12) among modalities at the peak systole of the pulsatile flow condition were presented. We found that the results are similar to our steady condition results that presented in this chapter (performed to mimic the peak systole condition) and no new additional information can be drawn from the unsteady results regarding the WSS distributions.

Since it is expected that the highest WSS will be generated at the peak systole, by focusing on extracting distributions of WSS (as a potential local biomarker to indicate a probable location of the aneurysm rupture) solely at this particular time instant will make the entire computationally based clinical approach much more efficient (resulting in a factor of 100-1000 speed-up compared to the multi-cycle pulsating flow conditions simulations). Low computational cost is especially an important aspect of simulating a large number of patient-specific cases.

In conclusion, when the focus is on comparing the flow and/or WSS, prescribing steady-state flow at the inlet is efficient and sufficient - the additionally performed experimental and numerical studies (based on the patient-specific pulsating inflow) re-confirmed further our initial findings.

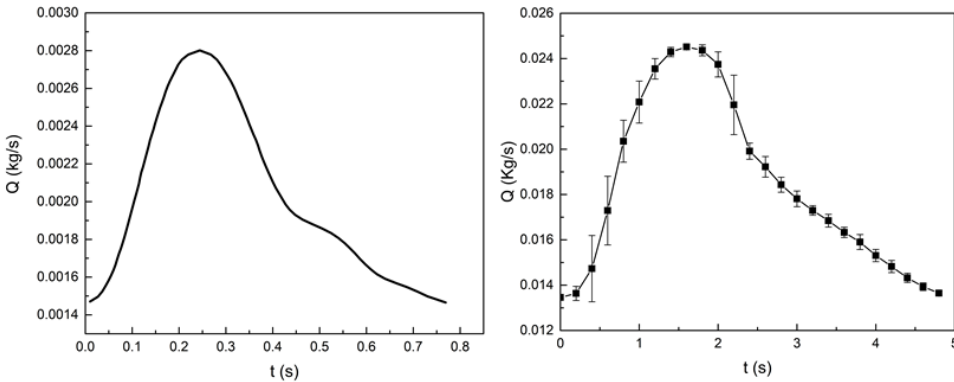


Figure 2.9: Inlet mass flow rates for CFD unsteady simulation (left), and for unsteady PIV measurements (right).

The inlet flow profile of CFD was the average flow rate of 9 cardiac cycles measured by 4D-Flow MRI. This patient-specific flow pattern was mimicked by the pump system in PIV experiments. Since in PIV experiments the dimension of the aneurysm was scaled up 3.77 times and the fluid properties also differ from blood, the Womersley number ( $\alpha = 2.33$ ) and the Reynolds number ( $Re = 350$ ) which characterize the aneurysmal flow were kept the same as 4D-Flow MRI measurement to ensure dynamic similarity.

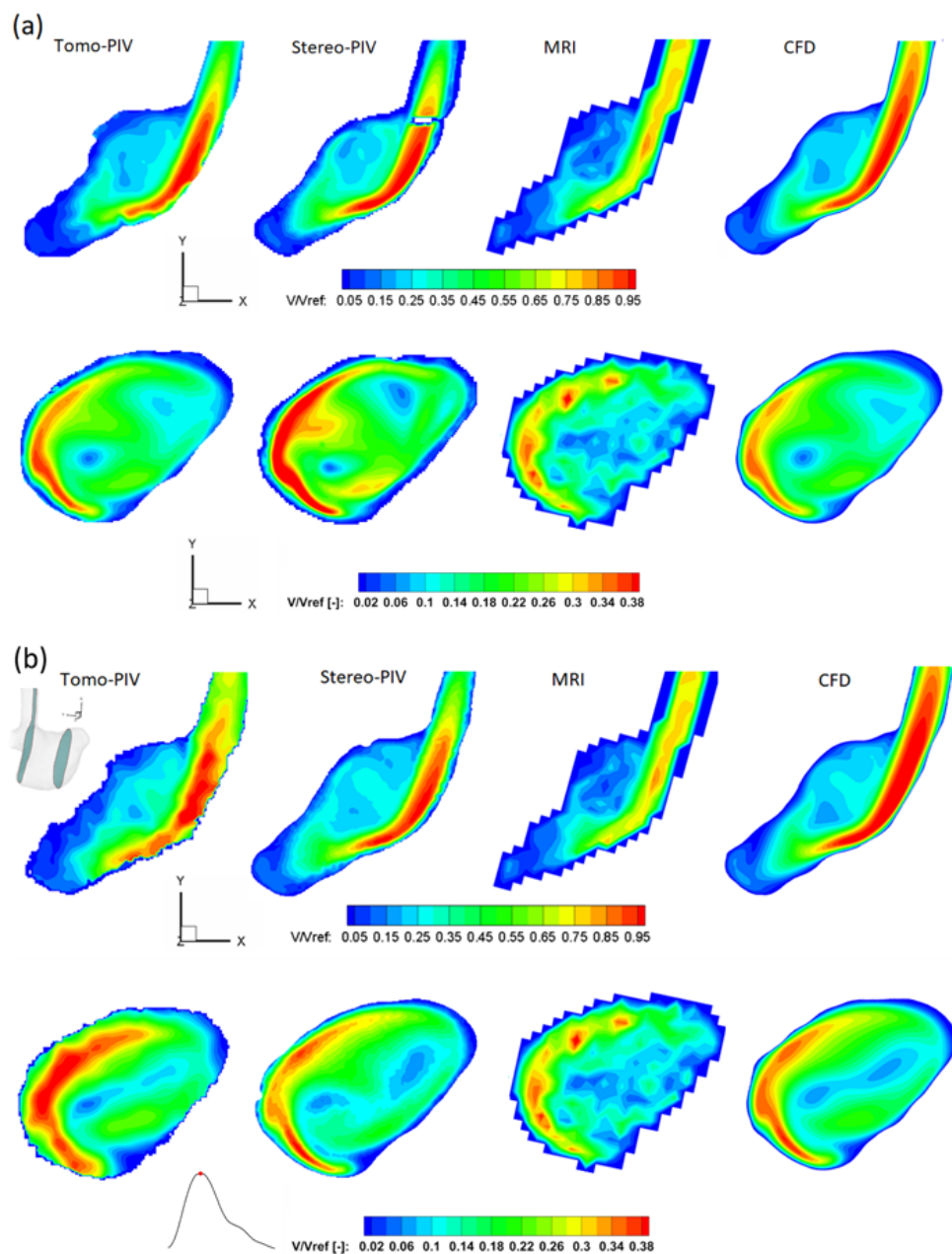


Figure 2.10: Velocity magnitude comparison between Tomo-PIV, Stereo-PIV, MRI and CFD at peak systole under (a) steady-state condition and (b) pulsatile flow condition.

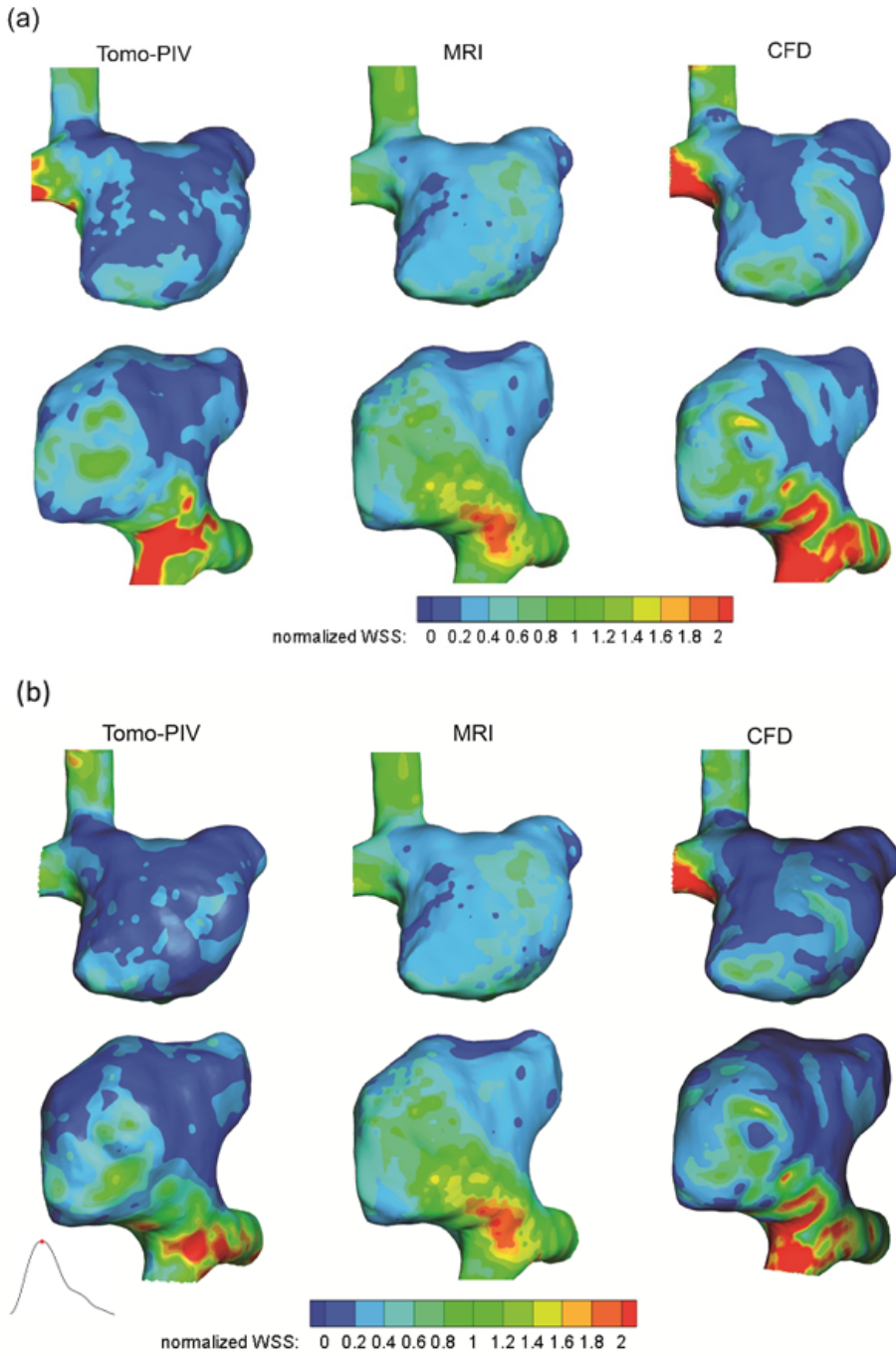


Figure 2.11: Normalized WSS comparison between Tomo-PIV, MRI and CFD at peak systole under (a) steady-state condition and (b) pulsatile flow condition.

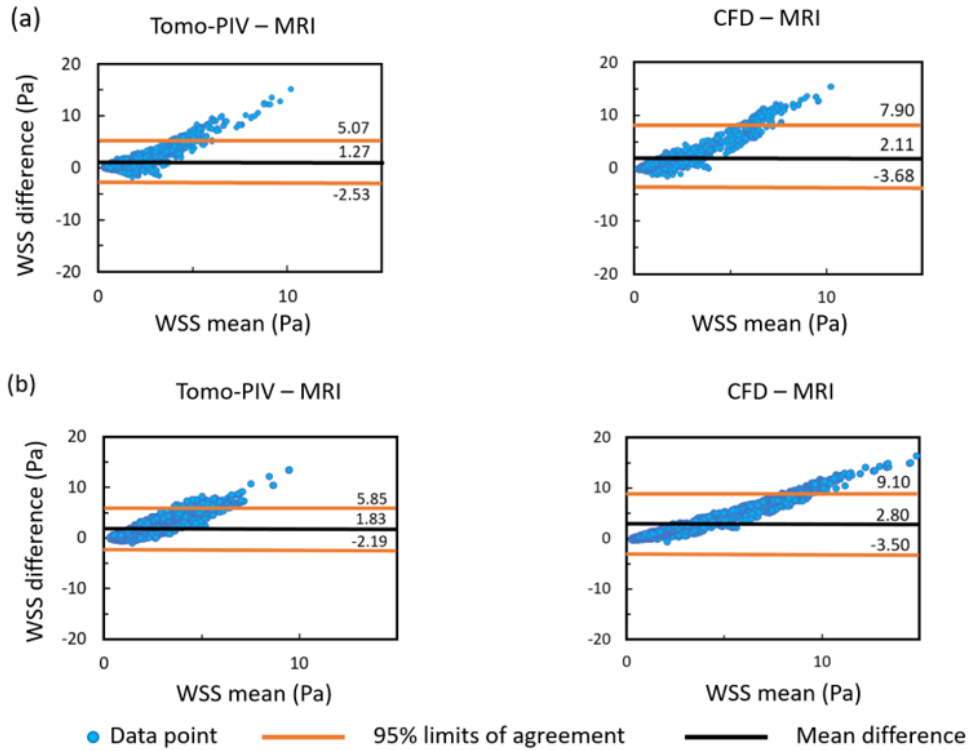


Figure 2.12: Bland-Altman plots of absolute WSS values at peak systole of (a) steady-state condition and (b) pulsatile flow condition, comparing MRI to Tomo-PIV and CFD.

# REFERENCES

- [1] N. Ajiboye, N. Chalouhi, R. M. Starke, M. Zanaty, R. Bell, *et al.*, “Unruptured cerebral aneurysms: Evaluation and management”, *The Scientific World Journal*, vol. 2015, 2015.
- [2] B. Weir, “Unruptured intracranial aneurysms: A review”, *Journal of Neurosurgery*, vol. 96, no. 1, pp. 3–42, 2002.
- [3] V. L. Rayz and A. A. Cohen-Gadol, “Hemodynamics of cerebral aneurysms: Connecting medical imaging and biomechanical analysis”, *Annual Review of Biomedical Engineering*, vol. 22, pp. 231–256, 2020.
- [4] M. K. Abraham and W.-T. W. Chang, “Subarachnoid hemorrhage”, *Emergency Medicine Clinics*, vol. 34, no. 4, pp. 901–916, 2016.
- [5] L. Spelle and L. Pierot, “Endovascular treatment of non-ruptured intracranial aneurysms: Critical analysis of the literature”, *Journal of Neuroradiology*, vol. 35, no. 2, pp. 116–120, 2008.
- [6] J. Cebal, E. Ollikainen, B. J. Chung, *et al.*, “Flow conditions in the intracranial aneurysm lumen are associated with inflammation and degenerative changes of the aneurysm wall”, *American Journal of Neuroradiology*, vol. 38, no. 1, pp. 119–126, 2017.
- [7] J. R. Cebal, F. Detmer, B. J. Chung, *et al.*, “Local hemodynamic conditions associated with focal changes in the intracranial aneurysm wall”, *American Journal of Neuroradiology*, vol. 40, no. 3, pp. 510–516, 2019.
- [8] P. van Ooij, W. V. Potters, A. Guédon, *et al.*, “Wall shear stress estimated with phase contrast MRI in an in vitro and in vivo intracranial aneurysm”, *Journal of Magnetic Resonance Imaging*, vol. 38, no. 4, pp. 876–884, 2013.
- [9] W. V. Potters, P. van Ooij, H. Marquering, E. vanBavel, and A. J. Nederveen, “Volumetric arterial wall shear stress calculation based on cine phase contrast MRI”, *Journal of Magnetic Resonance Imaging*, vol. 41, no. 2, pp. 505–516, 2015.
- [10] J. Szajer and K. Ho-Shon, “A comparison of 4D flow MRI-derived wall shear stress with computational fluid dynamics methods for intracranial aneurysms and carotid bifurcations—a review”, *Magnetic Resonance Imaging*, vol. 48, pp. 62–69, 2018.
- [11] R. S. Reneman, T. Arts, and A. P. Hoeks, “Wall shear stress—an important determinant of endothelial cell function and structure—in the arterial system in vivo: Discrepancies with theory”, *Journal of Vascular Research*, vol. 43, no. 3, pp. 251–269, 2006.

- [12] J. R. Cebal, M. A. Castro, J. E. Burgess, R. S. Pergolizzi, M. J. Sheridan, and C. M. Putman, "Characterization of cerebral aneurysms for assessing risk of rupture by using patient-specific computational hemodynamics models", *American Journal of Neuroradiology*, vol. 26, no. 10, pp. 2550–2559, 2005.
- [13] P. Berg, C. Roloff, O. Beuing, *et al.*, "The computational fluid dynamics rupture challenge 2013—phase ii: Variability of hemodynamic simulations in two intracranial aneurysms", *Journal of Biomechanical Engineering*, vol. 137, no. 12, p. 121 008, 2015.
- [14] J. Xiang, S. K. Natarajan, M. Tremmel, *et al.*, "Hemodynamic–morphologic discriminants for intracranial aneurysm rupture", *Stroke*, vol. 42, no. 1, pp. 144–152, 2011.
- [15] S. Kenjereš and B. Righolt, "Simulations of magnetic capturing of drug carriers in the brain vascular system", *International Journal of Heat and Fluid Flow*, vol. 35, pp. 68–75, 2012.
- [16] M. Cibis, W. V. Potters, F. J. Gijzen, *et al.*, "Wall shear stress calculations based on 3D cine phase contrast mri and computational fluid dynamics: A comparison study in healthy carotid arteries", *NMR in Biomedicine*, vol. 27, no. 7, pp. 826–834, 2014.
- [17] M. Shojima, M. Oshima, K. Takagi, *et al.*, "Magnitude and role of wall shear stress on cerebral aneurysm: Computational fluid dynamic study of 20 middle cerebral artery aneurysms", *Stroke*, vol. 35, no. 11, pp. 2500–2505, 2004.
- [18] L.-D. Jou, D. H. Lee, H. Morsi, and M. E. Mawad, "Wall shear stress on ruptured and unruptured intracranial aneurysms at the internal carotid artery", *American Journal of Neuroradiology*, vol. 29, no. 9, pp. 1761–1767, 2008.
- [19] J. Cebal, F. Mut, M. Raschi, *et al.*, "Aneurysm rupture following treatment with flow-diverting stents: Computational hemodynamics analysis of treatment", *American Journal of Neuroradiology*, vol. 32, no. 1, pp. 27–33, 2011.
- [20] H. Meng, V. Tutino, J. Xiang, and A. Siddiqui, "High WSS or low WSS? complex interactions of hemodynamics with intracranial aneurysm initiation, growth, and rupture: Toward a unifying hypothesis", *American Journal of Neuroradiology*, vol. 35, no. 7, pp. 1254–1262, 2014.
- [21] N. Buchmann, C. Atkinson, M. Jeremy, and J. Soria, "Tomographic particle image velocimetry investigation of the flow in a modeled human carotid artery bifurcation", *Experiments in Fluids*, vol. 50, pp. 1131–1151, 2011.
- [22] T. Yagi, A. Sato, M. Shinke, *et al.*, "Experimental insights into flow impingement in cerebral aneurysm by stereoscopic particle image velocimetry: Transition from a laminar regime", *Journal of the Royal Society Interface*, vol. 10, no. 82, p. 20 121 031, 2013.
- [23] A. L. DiCarlo, D. W. Holdsworth, and T. L. Poepping, "Study of the effect of stenosis severity and non-Newtonian viscosity on multidirectional wall shear stress and flow disturbances in the carotid artery using particle image velocimetry", *Medical Engineering & Physics*, vol. 65, pp. 8–23, 2019.

- [24] M. C. Brindise, S. Rothenberger, B. Dickerhoff, *et al.*, “Multi-modality cerebral aneurysm haemodynamic analysis: In vivo 4D flow MRI, in vitro volumetric particle velocimetry and in silico computational fluid dynamics”, *Journal of the Royal Society Interface*, vol. 16, no. 158, p. 20190465, 2019.
- [25] R. Medero, K. Ruedinger, D. Rutkowski, K. Johnson, and A. Roldán-Alzate, “In vitro assessment of flow variability in an intracranial aneurysm model using 4D flow MRI and tomographic PIV”, *Annals of Biomedical Engineering*, vol. 48, pp. 2484–2493, 2020.
- [26] P. van Ooij, J. Zwanenburg, F. Visser, *et al.*, “Quantification and visualization of flow in the circle of willis: Time-resolved three-dimensional phase contrast MRI at 7 T compared with 3 T”, *Magnetic Resonance in Medicine*, vol. 69, no. 3, pp. 868–876, 2013.
- [27] G. Elsinga, B. Van Oudheusden, and F. Scarano, “Experimental assessment of tomographic-PIV accuracy”, in *13th International Symposium on Applications of Laser Techniques to Fluid Mechanics, Lisbon, Portugal, paper*, Citeseer, vol. 20, 2006.
- [28] R. Frayne and B. K. Rutt, “Understanding acceleration-induced displacement artifacts in phase-contrast MR velocity measurements”, *Journal of Magnetic Resonance Imaging*, vol. 5, no. 2, pp. 207–215, 1995.
- [29] C. Roloff, D. Stucht, O. Beuing, and P. Berg, “Comparison of intracranial aneurysm flow quantification techniques: Standard PIV vs stereoscopic PIV vs tomographic PIV vs phase-contrast MRI vs CFD”, *Journal of Neurointerventional Surgery*, 2018.
- [30] H. Isoda, Y. Ohkura, T. Kosugi, *et al.*, “Comparison of hemodynamics of intracranial aneurysms between MR fluid dynamics using 3D cine phase-contrast MRI and MR-based computational fluid dynamics”, *Neuroradiology*, vol. 52, pp. 913–920, 2010.
- [31] T. Naito, S. Miyachi, N. Matsubara, *et al.*, “Magnetic resonance fluid dynamics for intracranial aneurysms—comparison with computed fluid dynamics”, *Acta Neurochirurgica*, vol. 154, pp. 993–1001, 2012.
- [32] S. Petersson, P. Dyverfeldt, and T. Ebbers, “Assessment of the accuracy of MRI wall shear stress estimation using numerical simulations”, *Journal of Magnetic Resonance Imaging*, vol. 36, no. 1, pp. 128–138, 2012.
- [33] A. F. Stalder, M. Russe, A. Frydrychowicz, J. Bock, J. Hennig, and M. Markl, “Quantitative 2D and 3D phase contrast MRI: Optimized analysis of blood flow and vessel wall parameters”, *Magnetic Resonance in Medicine*, vol. 60, no. 5, pp. 1218–1231, 2008.
- [34] G. Carty, S. Chatpun, and D. M. Espino, “Modeling blood flow through intracranial aneurysms: A comparison of Newtonian and non-Newtonian viscosity”, *Journal of Medical and Biological Engineering*, vol. 36, pp. 396–409, 2016.
- [35] D. Lopes, H. Puga, J. C. Teixeira, and S. Teixeira, “Influence of arterial mechanical properties on carotid blood flow: Comparison of CFD and FSI studies”, *International Journal of Mechanical Sciences*, vol. 160, pp. 209–218, 2019.

- [36] K. Pielhop, M. Klaas, and W. Schröder, “Experimental analysis of the fluid–structure interaction in finite-length straight elastic vessels”, *European Journal of Mechanics-B/Fluids*, vol. 50, pp. 71–88, 2015.
- [37] P. H. Geoghegan, M. C. Jermy, and D. S. Nobes, “A PIV comparison of the flow field and wall shear stress in rigid and compliant models of healthy carotid arteries”, *Journal of Mechanics in Medicine and Biology*, vol. 17, no. 03, p. 1 750 041, 2017.
- [38] A. Geers, I. Larrabide, H. Morales, and A. Frangi, “Comparison of steady-state and transient blood flow simulations of intracranial aneurysms”, in *2010 Annual International Conference of the IEEE Engineering in Medicine and Biology*, IEEE, 2010, pp. 2622–2625.
- [39] J. R. Cebal, F. Mut, J. Weir, and C. Putman, “Quantitative characterization of the hemodynamic environment in ruptured and unruptured brain aneurysms”, *American Journal of Neuroradiology*, vol. 32, no. 1, pp. 145–151, 2011.

# 3

## SHAKE-THE-BOX IN A LEFT VENTRICLE MODEL

### 4D FLOW PATTERNS AND RELATIVE PRESSURE IN A LEFT VENTRICLE MODEL BY SHAKE-THE-BOX AND PROPER ORTHOGONAL DECOMPOSITION ANALYSIS

#### **Background**

*Intraventricular blood flow dynamics are associated with cardiac function. Accurate, noninvasive, and easy assessments of hemodynamic quantities (such as velocity, vortex, and pressure) could be an important addition to the clinical diagnosis and treatment of heart diseases. However, the complex time-varying flow brings many challenges to the existing noninvasive image-based hemodynamic assessments. Reliable measurement techniques and analysis tools are essential for the development of applying hemodynamic biomarkers in clinical practice.*

#### **Methods**

*In this study, a time-resolved particle tracking method, Shake-the-Box, was applied to reconstruct the flow in a realistic left ventricle (LV) silicone model with biological valves. Based on the obtained velocity, 4D pressure field was calculated using a Poisson equation-based pressure solver. Furthermore, flow analysis by proper orthogonal decomposition (POD) of the 4D velocity field has been performed.*

#### **Results**

*As a result of the Shake-the-Box algorithm, we have extracted: (i) particle positions, (ii) particle tracks, and finally, (iii) 4D velocity fields. From the latter, the temporal evolution*

---

This chapter has been published as: Wu, X., Saaid, H., Voorneveld, J., Claessens, T., Westenberg, J.J., de Jong, N., Bosch, J.G. and Kenjereš, S., 4D Flow Patterns and Relative Pressure Distribution in a Left Ventricle Model by Shake-the-Box and Proper Orthogonal Decomposition Analysis. *Cardiovasc Eng Tech* 14, 743–754 (2023)

of the 3D pressure field during the full cardiac cycle was obtained. The obtained maximal pressure difference extracted along the base-to-apex was about 2.7 mmHg, which is in good agreement with those reported *in vivo*. The POD analysis results showed a clear picture of different scale of vortices in the pulsatile LV flow, together with their time-varying information and corresponding kinetic energy content. To reconstruct 95% of the kinetic energy of the LV flow, only the first six POD modes would be required, leading to significant data reduction.

### **Conclusions**

This work demonstrated Shake-the-Box is a promising technique to accurately reconstruct the left ventricle flow field *in vitro*. The good spatial and temporal resolutions of the velocity measurements enabled a 4D reconstruction of the pressure field in the left ventricle. The application of POD analysis showed its potential in reducing the complexity of the high-resolution left ventricle flow measurements. For future work, image analysis, multi-modality flow assessments, and the development of new flow-derived biomarkers can benefit from fast and data-reducing POD analysis.

### 3.1. INTRODUCTION

Current research efforts in hemodynamic analysis of blood flow in a left ventricle (LV) are associated with an ever-demanding quest to find proper flow-derived biomarkers that can be used for the early identification of heart failure. Studies have demonstrated that the intraventricular flow patterns, local pressure differences, and flow kinetic energy were closely related to the function, efficiency, and pathologies of the LV [1]–[3]. For example, patients that underwent mitral valve replacement had a reversed vortical motion in LV during diastole, which resulted in higher flow kinetic energy dissipation compared to the normal subjects [4]. The intraventricular pressure gradient is found to be correlated to the propagation of early diastolic filling in heart failure patients [5]. Based on a similar foundation, many research studies are ongoing to further refine quantitative assessment of the hemodynamic parameters in the LV or to develop new reliable tools for this, which will enable a timely diagnosis of heart diseases in clinical practice.

In literature, two-dimensional (2D) particle imaging velocimetry (PIV) (either in form of a standard planar PIV providing just two velocity components, or in form of stereoscopic PIV providing all three components of the velocity in a characteristic plane) is the most commonly used optical technique for in vitro flow measurements in transparent models of the LV, and downstream of the heart valves [6]–[9]. However, the vortex-rich flow structures and the wide-ranged flow regimes—from laminar to transitional, and turbulent—within the LV necessitate the use of three-dimensional (3D) high-resolution experimental techniques. Only in recent years, 3D optical techniques, such as tomographic PIV (Tomo-PIV) and 3D particle tracking velocimetry (PTV), are applied in studying the flow downstream of the aortic or mitral valves [10]–[13]. Despite the fact that Tomo-PIV is a volumetric technique, there are still some technical challenges that affect the obtained velocity field [14] (e.g., ghost particles, limited position accuracy of 0.3 pixel, spatial averaging over interrogation windows resulting in the smoothing of the velocity gradients and small-scale flow structures, etc.).

Compared to PIV, particle tracking velocimetry (PTV) techniques have a higher order of accuracy and are capable of delivering more reliable results in strong-shear flow and near-wall regions [14]. However, there is a major drawback of conventional PTV techniques, which is the limited spatial resolution restricted by low seeding density. Recently, a novel 3D Lagrangian particle tracking (LPT) algorithm ‘Shake-the-Box’ (STB) [14] has been developed. It has overcome the low seeding concentration limitation, allowing the evaluation of significantly denser particle trajectory fields at very low ghost particles occurrence (< 0.004% false particles) and high accuracy (average position error of 0.018 pixel). With data assimilation algorithms or data binning, STB results can provide temporally resolved three-dimensional/three-components (3D/3C) Eulerian velocity fields in a high-resolution manner that is comparable (or even superior) to Tomo-PIV. To date, STB has not yet been applied in studying the flow topology in the LV.

At present, 3D flow diagnostics techniques are becoming more mature and applicable for a wide range of flow phenomena, allowing advanced analysis of the high-resolution velocity field and velocity-derived hemodynamic parameters. Modal analysis techniques such as Proper Orthogonal Decomposition (POD) offer a promising new direction for analyzing blood flow. POD is a data-driven reduced-order modeling tool, which enables breaking down a large high-dimensional dataset into a low-dimensional system where

the flow evolution is represented by energy-ordered spatial and temporal modes [15]. The dominant coherent flow structures in complex flows are effectively identified by finite physically interpretable linear modes while the inessential low-energy degrees of freedom are removed. In addition, POD is an entirely data-dependent technique that does not require a *priori* information about the system behavior. Comparative assessments based on the POD modes are computationally quite effective and reliable since they do not require registration nor mesh interpolations to compare datasets with different grids, coordinates, as well as different resolutions. Thanks to these features, POD analysis was widely used in various fluid mechanics applications. In cardiovascular flow, POD has been used in the analysis of the transitional or turbulent flow regimes in the following flows: (i) behind the mechanical aortic valve, (ii) in intracranial aneurysms, and (iii) in abdominal aortic aneurysms [16]–[18].

The main goals of the present work are: (a) to obtain 4D flow in a realistic LV model with biological valves using Shake-the-Box flow measurement technique; (b) to reconstruct the LV pressure field based on the 4D flow Shake-the-Box measurements; (c) to provide additional spatial-temporal information of the LV flow by applying POD analysis. These results can provide additional insights into the fluid dynamics of heart valves and the left ventricle.

## 3.2. METHODS

### 3.2.1. EXPERIMENTAL SETUP

The realistic LV used in this study has a statistically averaged shape derived from 150 patients' computed tomography (CT) scans [11], [19], [20]. The optically transparent compliant phantom based on this averaged shape geometry was made of four silicone layers (HT 33 Transparent LT, Zhermack SpA, Rome, Italy). In addition to the LV shape, the phantom also contains a simplified atrium and aortic root extensions. Biological valves (biological Perimount 2900, Edwards Lifesciences, Irvine, USA) were placed at the aortic and mitral positions. Characteristic dimensions of the complete model are summarized in Fig. 3.2a. The refractive index of the silicone phantom is  $n = 1.413$ . To achieve minimal optical distortion, a mixture of water-glycerol was chosen as a blood-mimicking fluid. By varying the water/glycerol concentration, the refractive index was matched to the phantom material. The resulting fluid solution (60% glycerol, 40% water) has a density of  $\rho = 1160 \text{ Kg/m}^3$  and dynamic viscosity of  $\mu = 0.01777 \text{ Pa}\cdot\text{s}$ . The fluid in the LV was seeded with Fluorescent Rhodamine-B particles (diameter of 20–50  $\mu\text{m}$  and a density of 1100  $\text{kg/m}^3$ ) in a particle image density of 0.04 particles per pixel (ppp). A commercial piston pump (Vivitro Labs Inc., BC, Canada) was used to impose a sinusoidal-like volume change of the external pressure chamber with a cardiac cycle period of 857 ms (70 bpm, systolic duration of 300 ms, stroke volume 50 ml). The dynamics of the LV-shape variation was imposed by this external volume variation (the ventricle volume change must be equivalent to the external volume change) which induces the flow through the valves, mimicking an actively pumping ventricle. The overview of the experimental setup is shown in Fig. 3.1. For additional details of the experimental configuration, please see [11].

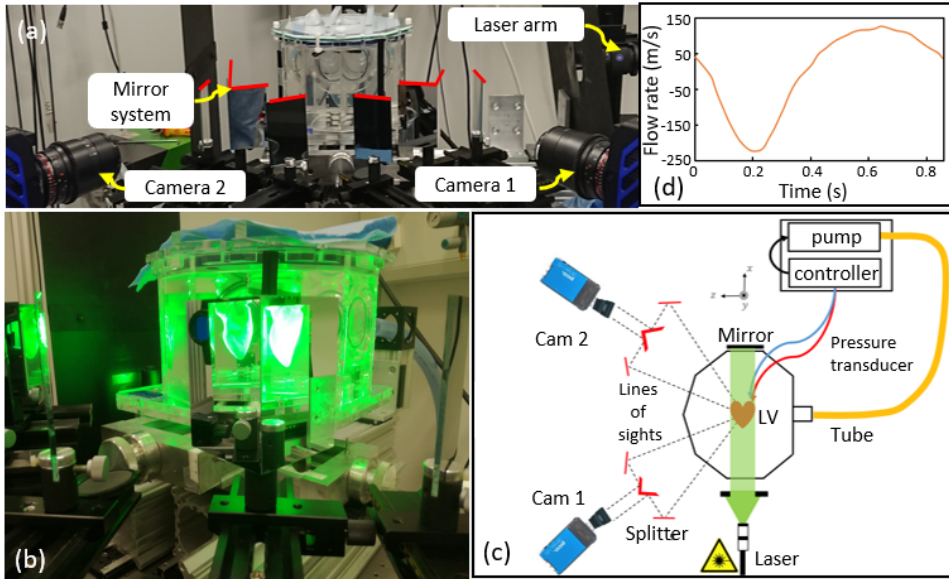


Figure 3.1: (a) The experimental setup (the front view), consisting of the left ventricle phantom, laser arm, two CMOS cameras, and an image splitter mirror system, (b) An indication of the image splitting, (c) Schematic sketch of the experimental setup (the top-view), (d) The flow waveform imposed at the pump.

### 3.2.2. DATA ACQUISITION AND SHAKE-THE-BOX ANALYSIS

Two high-speed cameras (Imager Pro HS 4 M, PCO, Kelheim, Germany), each with an image splitter, were applied to acquire particle images from four different views with a frequency of 2 kHz. Image acquisition and processing were performed in DaVis 10.1 (LaVision, Göttingen, Germany). In total 30 cardiac cycles were recorded. The initial calibration was performed using a two-plane target immersed in the working fluid and a third-order polynomial fitting mapping method was applied, resulting in an error of approximately 0.2 pixel ( $\sim 2.4 \mu\text{m}$ ) for all views. This calibration was then improved to less than 0.02 pixel error by conducting volume self-calibration based on preprocessed particle images. Details of the image preprocessing were given in our previous publication [11]. Next, a local determination of the particles' optical transfer function (OTF) [21] was performed to correctly describe the particle shapes in recorded images, which was needed for the STB calculations.

To initialize the STB algorithm, identification of particles was performed in the first four time steps using an iterative particle reconstruction (IPR) method [22]. To find as many potential particle candidates as possible, an intensity threshold of 5 counts and an allowed triangulation error of 1 voxel were specified. After initialization, an iterative process was applied for the subsequent time steps in adding particles and refining their positions by matching the images (i.e., 'shaking' procedure). For each time instant, a guess of the particles' next position was made by extrapolating particle projections from the previous time steps. The predicted distribution of particles was refined by shaking particles by 0.1 voxel in the 3D domain. Simultaneously, residual images were

obtained by subtracting the corrected particles distribution from the initial images. Then, a triangulation was conducted on the residual images to identify new particles. Both the tracked and new particles were shaken again in a total of eight iterations to increase the accuracy. New particles were added only if they were found in at least four consecutive time steps. The final convergent solution contained approximately 7000 particle tracks in the measured volume ( $62 \times 100 \times 57$  mm). To obtain the final time-resolved 3D velocity field and derived variables (e.g., vorticity, vortical structures, or pressure), the particle tracks were first fitted with quadratic B-splines with a typical length of 3 time steps to retrieve velocity and acceleration from the discrete particle-based information. After this, the velocity vectors were interpolated onto the Eulerian grid using binning with the Gaussian weighting. The data Binning is similar to the interrogation window in the Tomo-PIV. In the vector Binning process, we set an initial sub-volume of 72 voxels and an overlap of 87.5% for iterations, resulting in a final resolution of 9 voxels (0.735 mm) in each dimension. A convergence analysis was conducted by comparing the phase averaged data obtained from 10, 20, and 30 cardiac cycles. We obtained velocity vector differences smaller than 2% among these datasets. Hence, the averaged velocity field data of 10 cycles is sufficient to obtain a reliable POD analysis and pressure calculations.

### 3.2.3. INSTANTANEOUS PRESSURE FIELD

To obtain the relative pressure field from the STB calculated velocity vectors, we apply the 4D Poisson solver of DaVis 10.1. We provide a short mathematical rationale of the pressure extraction based on the Navier-Stokes equations for incompressible fluids [23]:

$$\nabla p = -\rho \frac{D\mathbf{u}}{Dt} + \mu \nabla^2 \mathbf{u} \quad (3.1)$$

where  $p$ ,  $\mathbf{u}$ ,  $t$ ,  $\rho$ , and  $\mu$  represent the pressure, velocity, density, and dynamic viscosity of the fluid, respectively, and  $\frac{D\mathbf{u}}{Dt}$  is the velocity material derivative. The latter can be expressed in the Lagrangian framework as a local velocity difference of a particle at two points along its pathline:

$$\frac{D\mathbf{u}}{Dt} = \frac{d\mathbf{u}_p(t)}{dt} = \frac{d\mathbf{u}(\mathbf{x}_p(t), t)}{dt} \quad (3.2)$$

where  $\mathbf{x}_p(t)$  and  $\mathbf{u}_p(t)$  are the position and the velocity of a selected fluid particle, respectively. The particle positions  $\mathbf{x}_p$  are determined from the STB reconstructed particle trajectories, and the material derivative is calculated from the second-order least-square fitting scheme. Once the material derivative is determined, the pressure gradient of the entire measurement domain can be obtained from Eq. 3.1. The pressure field is then evaluated by solving a Poisson equation. By taking the divergence of Eq. 3.1, one can obtain the Poisson pressure equation (PPE):

$$\nabla^2 p = \nabla \cdot \mathbf{b} \quad (3.3)$$

where  $\mathbf{b}$  denotes contributions from the right hand side terms of Eq. 3.1. In Davis, the 4D pressure solver also includes the time derivative term of pressure via estimation of the convective velocity of the flow structure:

$$\nabla'^2 p = \nabla \cdot \mathbf{b} + \xi \frac{\partial^2 p}{\partial t^2} \Big|_c \quad (3.4)$$

where  $\nabla'^2$  is a modified operator,  $\xi$  is the weighting factor between the temporal and spatial derivatives, and the time derivative of pressure is calculated as:

$$\frac{\partial p}{\partial t} \Big|_c \approx \frac{1}{\Delta t} \int_{x+\mathbf{u}_c \Delta t}^x \nabla p d\mathbf{x} \quad (3.5)$$

where  $\mathbf{u}_c$  is the convective velocity. If setting  $\xi = 0$ , then the convective velocity is not calculated and the pressure field is evaluated separately for each instantaneous velocity field. In the present study, we adopt  $\xi = 1$ , resulting in the estimation of the convective velocity  $\mathbf{u}_c$  by applying the least-squares method of [24]. Moreover, under the incompressible fluid assumption, a divergence-free filter is applied to the calculated velocity field before it is used for the pressure calculation. This leads to efficient suppression of non-physical pressure fluctuations in time, resulting in high temporal accuracy. An additional advantage of the inclusion of the time derivative of the pressure in the PPE equation is that a reference pressure only needs to be applied once at the very first time step. In the present study, we prescribed Dirichlet boundary condition with an average zero value of the measured domain at the first time step. Whereas Neumann condition, which makes use of the calculated pressure gradient from Eq. 3.1, is imposed at all boundary voxels at each time step. Consequently, the calculated field represents the relative pressure. Additional numerical details of the 4D pressure solver are given in [25], [26].

### 3.2.4. 3D POD ANALYSIS

Next, we present the mathematical rationale of the snapshot POD analysis that we applied to the STB measured instantaneous velocity field [27], [28]. Each instantaneous STB velocity measurement is a snapshot of the flow. In the snapshot POD method, the velocity field is decomposed into a linear combination of spatially orthonormal modes and their corresponding coefficients:

$$\mathbf{u}(x, t) \approx \sum_{k=1}^N a_k(t) \cdot \phi_k(x) \quad (3.6)$$

where  $x$  is the location,  $t$  is the time,  $N$  denotes the total number of snapshots ( $k$  is the snapshot index),  $\mathbf{u}(x, t)$  is the measured velocity,  $\phi_k(x)$  are the spatial orthonormal modes (i.e. eigenfunctions representing the spatial behavior of the flow), and  $a_k(t)$  are the time coefficients (representing the flow changes over time). The eigenfunctions are obtained by solving the eigenvalue problem. In the content of the present work, the resulting eigenvalues will be referred to as the kinetic energy contributions of corresponding POD modes [28], [29]. These eigenvalues then can be ordered in a decreasing order such that the first few POD modes are containing the largest amount of kinetic energy. Consequently, dominant coherent flow structures associated with the first few POD modes can be easily identified. In the present study, the full three-dimensional POD analysis is performed over 343 snapshots (5 times temporal downsampling of STB measurement data) covering the cardiac cycle. Note that the shape of the left ventricle model changes over time. This

moving boundary condition results the grid and the number of vectors differs from each snapshot. To handle this condition, the mesh at end-systole was selected as reference frame. The velocity data of other time steps were interpolated by polynomial functions onto this reference mesh. The POD analysis is then performed on the interpolated data.

### 3.3. RESULTS AND DISCUSSION

#### 3.3.1. GENERAL INTRAVENTRICULAR FLOW FEATURES

The generated flow structures in the LV are visualized by means of a long exposure recording of the fluorescent particles during Tomo-PIV experiments [11], shown in Fig. 3.2b. Corresponding instantaneous locations of the particles extracted from the Shake-the-Box are shown in Fig. 3.2c. The reconstructed particle tracks from 40 consecutive time steps during the filling phase are shown in Fig. 3.2d. Approximately 7000 particles are identified and colored by the velocity magnitude. It can be seen that the biological valve generates a strong trans-mitral jet accompanied by a pair of counter-rotating vortices, Fig. 3.2d. This particular feature has been regarded as an important criterion in valve design. Many studies have addressed that optimal vortex formation plays an important role in preserving the momentum and kinetic energy of the intraventricular flow [3], [30], [31]. In Fig. 3.3a, we tracked the diastolic vortex propagation by presenting vortex structures at six characteristic time instants of the cardiac cycle. Here, we superimposed the contours of the velocity magnitude in the central vertical plane with 3D vortex structures identified as iso-surfaces of the  $\lambda_2 = -150 \text{ 1/s}^2$  (colored in grey) (where  $\lambda_2$  is the second eigenvalue of the symmetric tensor ( $S^2 + \Omega^2$ ) where  $S$  and  $\Omega$  are symmetric and antisymmetric parts of the velocity gradient tensor [32]). The roll-up of the shear layer, generated by the transmitral flow jet, results in a ring-shaped vortex. It starts to pinch-off from the mitral annulus at time step III, and then propagates towards the center of the ventricle at later time instants IV and V. At time instant VI, the central jet reaches the side wall of the ventricle and the dominant vortex ring structure starts to break down. The evolution of this vortical structure is in agreement with similar *in vivo* and *in silico* studies previously reported in literature [3], [30], [31]. We perform a detailed comparison of the STB measured velocity field with the previous Tomo-PIV (see the Appendix A). Overall good agreement between techniques is obtained with some distinct advantages of the STB in a better representation of the velocity vectors in the near wall region and, consequently, in a more accurate capturing of the LV wall morphology changes during the cardiac cycle (see animations in Supplementary Material of the online publication [33]). This can be beneficial for the validation of numerical simulations intended to mimic exact experimental conditions, similar to Refs. [11], [34].

#### 3.3.2. 4D RELATIVE PRESSURE FIELD

In Fig. 3.3b, we show the relative pressure contours in the central vertical plane at various time instants of the cardiac cycle. 2D projections of the velocity vectors (x- and y-components) are superimposed on the pressure contour to indicate the flow. To further study the temporal variation of the intraventricular pressure, the pressure differences between two representative locations and the apex of the LV are plotted over time in Fig. 3.4c. The locations are indicated in Fig. 3.4a: (a) the apex, (b) 3 cm below location c,

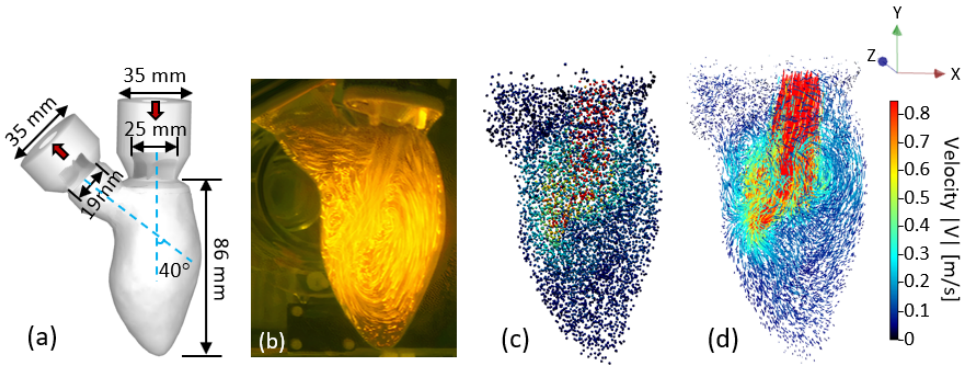


Figure 3.2: (a) Characteristic dimensions of the left ventricle model. The model contains bio-prosthetic mitral (25 mm, Perimount, Edwards Lifesciences Corp.) and aortic (19 mm, Perimount Magna Ease, Edwards Lifesciences Corp.) valves. The angle between the mitral valve and the aortic valve axes is 40°. (b) A long exposure picture of the particle image of the LV flow. (c) Particle tracers at an instantaneous time step reconstructed from the STB algorithm. (d) Reconstructed particle tracks of 40 consecutive time steps.

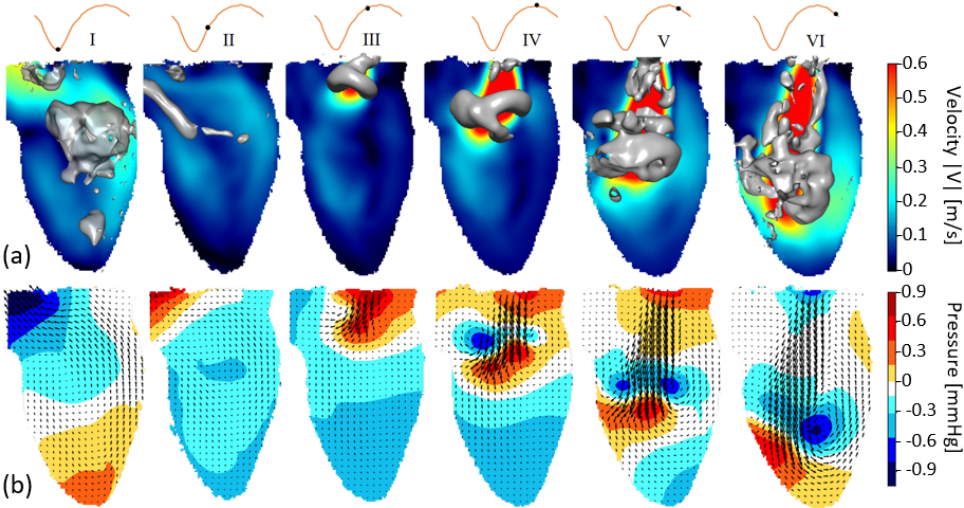


Figure 3.3: (a) Velocity contours at the center 2D z-plane and the 3D vortical structures identified by the lambda-2 criterion are visualized as iso-surface ( $\lambda_2 = -1501/s^2$ ). (b) Instantaneous Pressure contour at the center 2D z-plane. Roman numerals indicate the time steps (I = 0.265 s, II = 0.4 s, III = 0.645 s, IV = 0.7 s, V = 0.765 s, VI = 0.85 s).

and (c) the center of the mitral annulus. The velocity temporal profiles of these locations are also plotted in Fig. 3.4b. The diastolic and systolic flow can be recognized from the velocity profile at the LV base (location c).

The results show that the pressure distribution along the (longitudinal) base-apex axis reverses at the onset and the termination of the LV filling and ejecting, respectively (Fig. 3.3b). At the onset of early diastole (i.e., time-instant III), high pressure is observed

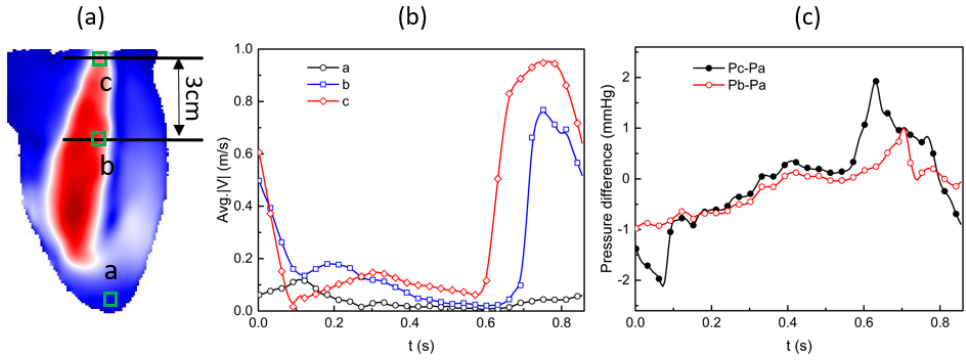


Figure 3.4: Assessments of temporal velocity profiles (b) at different positions a–c shown in (a). Pressure differences (c) between the apex location a and location near the left ventricle mitral annulus b and the base c. The pressure and velocity were averaged in a  $2 \times 2$  mm box (green) located at the center 2D z-plane

near the mitral valve and is gradually decreasing towards the LV apex, driving the blood entering the LV rapidly. Despite the rapid filling, the pressure in the proximity of the apex is continuously decreasing (time-instant IV), which can be observed as well in a successful LV suction *in vivo*. After the completion of the ventricular filling, a pressure increase takes place near the apex, and the pressure difference between the base and the apex starts to decline (time-step V), resulting in the blood flow decelerating and redirecting. Eventually, a reversal of the initial pressure distribution is observed at the late diastole (time-step VI): low pressure at the base while high pressure at the apex. Notably, during diastole, the intraventricular pressure does not increase or decrease monotonically across the long axis of the LV. Instead, localized low-pressure regions are observed where the aforementioned vortex ring presents. During systole, the pressure gradient inside the LV rises again with the minimal local pressure located below the aortic valve and the maximum pressure at the apex, compelling blood flow to the aortic valve (time-instant I). At the end of the systole (time-instant II), the pressure gradient reverses again, with the high- and low-pressure regions located in the proximities of the aortic valve and apex, respectively. This reversion pattern of intraventricular pressure can be also observed from the pressure differences between the apex and the base over time, Fig. 3.4c. This pressure change pattern in early filling and late ejection contributes to the closure of the aortic and mitral valves [35]. On the other hand, there are also some observed differences compared to the Non-invasive MRI-based relative pressure studies of [36], [37]. In comparison to these studies, the present study exhibits a smaller amplitude of the peak of the temporal evolution of the pressure difference between the apex and basal (mitral valve) locations, and also there is a lack of the second peak. These differences arise due to the simplified sinusoidal flow waveform imposed in our study, which fails to capture the strong acceleration of the E-wave and the presence of A-wave described *in vivo*. In addition, it's worth addressing that the spatiotemporal resolution and the choice of sampling points or planes to define the basal and apical locations can affect the accuracy of the pressure assessment, as discussed by [37]. However, it should be noted that the spatial resolution ( $0.735 \times 0.735 \times 0.735$  mm<sup>3</sup>) and temporal resolution (2 kHz) of

current study are considerably fine resolutions.

The overall reconstructed pressure magnitude in the LV model is in a similar range to our CFD result shown in [38], as well as previous studies based on pressure transducers [39], catheters [40], and MRI measurement [41]. The maximum relative pressure range in the LV is found to be about 2.7 mmHg, which is in good agreement with values reported in MRI studies [37], [42]–[44]. Nevertheless, it is important to acknowledge the impact of the aforementioned limitation, specifically the use of a simplified sinusoidal flow waveform. Despite this limitation, there are some advantages of the STB-based intraventricular relative pressure: (i) it is a non-invasive technique, (ii) it provides time-resolved 3D pressure distributions, instead of the 1-D point-like catheter measurements, (iii) relatively high spatiotemporal resolution, which can be utilized for further calibration, validation and improvement of the clinically available echocardiography [45] and MRI techniques [46].

### 3.3.3. POD ANALYSIS

#### POD MODES AND COEFFICIENTS

Next, we performed the 3D POD analysis using in total 343 snapshots of the STB-based velocity field over the entire cardiac cycle. The resulting flow morphologies visualized by calculated pathlines (colored by the velocity magnitude) for the first six spatial POD modes are shown in Fig. 3.5a. The corresponding contours of the out-of-plane vorticity component (in the  $z$ -coordinate direction) superimposed with the 3D velocity vectors in the central vertical plane are given in Fig. 3.5b-top. We also indicate the approximate size and direction of rotation of coherent flow structures with the black arrowed lines. Similarly, the contours of the  $z$ -vorticity in the selected horizontal plane for identical POD modes are shown in Fig. 3.5b-bottom. We show this plane also to illustrate the importance of performing a fully 3D POD analysis since by focusing solely on the central vertical plane (i.e., 2D data), many important 3D flow features will not be captured (e.g., the eccentricity of the central trans-mitral jet in the horizontal plane). Recall that the POD modes are ordered by flow kinetic energy dominance such that the first few modes should identify the most distinct flow features. It can be seen that the 1st spatial POD mode captures the central jet surrounded by a pair of counter-rotating vortices. This pattern is a well-known feature of the intraventricular flow during early diastole, as presented in [11], [30], [31]. The 2nd spatial POD mode is characterized by a clockwise coherent flow structure located between the middle of the LV and its apex. This flow structure is associated with vortices that appear during late diastole and remain until early systole. While the first pair of POD modes displayed the most prominent features of LV flow, small-scale flow structures are revealed in the higher spatial POD modes, Fig. 3.5a and b. The number of these small vortical structures significantly increases for the higher POD modes, but they are characterized by weaker velocity and vorticity. To elucidate further on the above-discussed vortex near the LV apex, we also perform additional POD analysis of the separate systole and diastole phases of the cardiac cycle, respectively, Fig. 3.6. A similar vortex can be seen in the 2nd POD mode of the diastole (containing 27.9% of total kinetic energy) and the 1st POD mode of the systole phase (containing 63.3% of the kinetic energy). The existence of this vortex was associated with a minimization of the momentum loss during the ejection phase by redirecting the flow already to the aortic root

before the LV ejects [4], [47]–[50]. However, some studies suggested that instead of leading to energy reduction for systolic ejection, this vortical motion is crucial in washing out the blood from the apical region and therefore preventing possible thrombus formation [51]–[53]. The results presented here indicate that the formation of this vortex is closely correlated with the LV contraction function due to its relatively high energy content (27.9% of diastolic flow, 63.3% of the systolic flow).

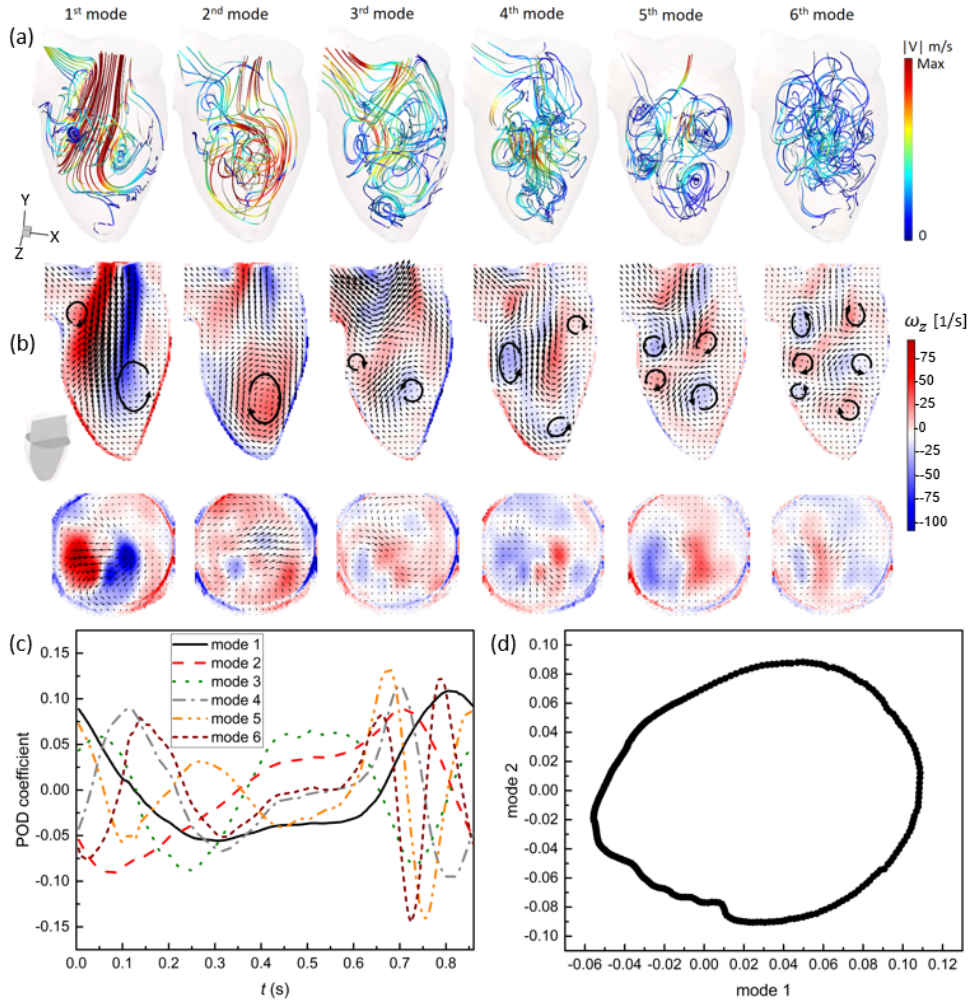


Figure 3.5: Snapshot POD analysis of the velocity field of the full cardiac cycle: a 3D Streamlines for the first six POD spatial modes, colored by velocity magnitude. The maximum of  $|V|$  is 0.8 m/s for the first three modes, and is 0.34 m/s for the 4th to 6th modes, b Vector fields of the first six POD spatial modes at the center z-plane colored by z-vorticity magnitude, c The corresponding time coefficient of the first six POD modes, d Phase portrait of the first two POD modes

In Fig. 3.5c, the time coefficients of the six POD modes are plotted as a function of the

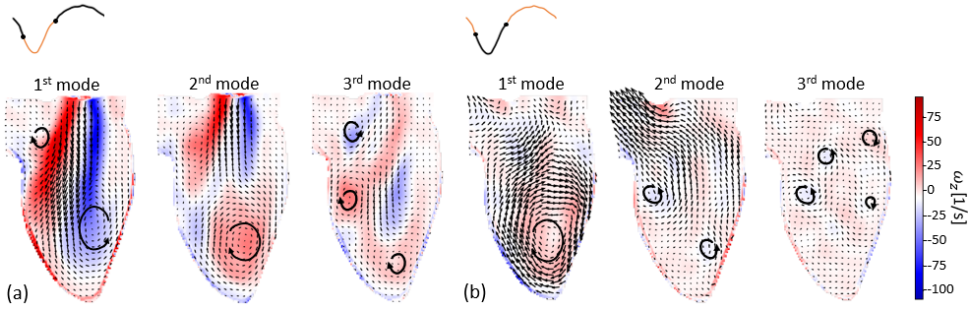


Figure 3.6: Vector fields of the first three spatial modes at the center z-plane colored by z-vorticity magnitude from a POD analysis of the diastolic phase and b POD analysis of the systolic phase.

cardiac cycle. It can be seen that the temporal evolutions of the first and second modes are similar and both resemble the shape of the flow waveform imposed at the mitral orifice. A phase-shift of  $\pi/4$  can be observed between the first two modes. For the higher POD modes, coefficients exhibit a more irregular behavior with various frequencies. However, similar to the first two modes, the coefficients of the second and third pair of modes evolve analogously in a pair, but with a phase-shift. It is noted that this pairwise characteristic was reported in well-defined periodic flows, such as flow over a cylinder [54], [55] (vortex shedding), or flow in carotid artery bifurcation [56]. In periodic flows, the first pair of modes are often found to be the orthogonal components of the basic harmonics and is usually associated with the traveling of a wave. The high temporal correlation of the first two modes can be verified from a phase portrait plotting one time coefficient as a function of another. As Fig. 3.5d shows, the time coefficients  $\alpha_1$  and  $\alpha_2$ , are strongly correlated, forming an ellipse-like trajectory. The observed deviations from an ideal elliptic trajectory could be an indication of cycle-to-cycle variations, induced by small-scale fluctuations or turbulence.

### 3.3.4. ENERGY CONTRIBUTION OF POD MODES

The fraction and accumulated fraction of the total kinetic energy of the flow as a function of the POD modes number are shown in Fig. 3.7a and b, respectively. It can be seen that a sum of the first two POD modes contribute to 76.5% of the total kinetic energy (with 50.3% for the 1st POD and 26.2% for the 2nd POD mode). This confirms the dominance of the first pair of the POD modes (i.e. a superposition of the central mitral jet and vortex near the apex will provide the most salient flow features quite accurately, see Fig. 3.5a and b). Although the first two eigenvalues are much bigger than the rest, the next four eigenvalues are still bigger than 1%. In total, the second and third pair of POD modes account for 18.5% of the kinetic energy. This suggests that to reconstructed the LV flow with 95% of the kinetic energy content, only six POD modes are needed. Compared to 343 snapshots, a significant data reduction is achieved. It should be kept in mind that the energy contribution of each mode could be case-related. For example, it was reported in experimental studies of a flow in ascending aorta with a normal and dysfunctional bileaflet mechanical aortic valve, the corresponding energetic contributions of the 1st

POD mode is approximately 74% and 60%, respectively [16]. Moreover, it was also reported that the normally functioning valve case also required the lowest number of POD modes to reconstruct the flow regardless of the percentage of the kinetic energy to be captured. A similar strategy can be also adopted for the flow in LV where various patient-specific cases and their comparison with the healthy control group can lead to establishing the specific thresholds of the POD modes contributions. An example is the study by [57], which provided 2D POD and DMD analysis for both healthy LV flow and for cases subjected to various degrees of aortic regurgitation. Future studies are needed to extend the database from 2D to 3D POD models. In addition, POD studies based on *in vivo* measurements are required to establish appropriate clinical thresholds.

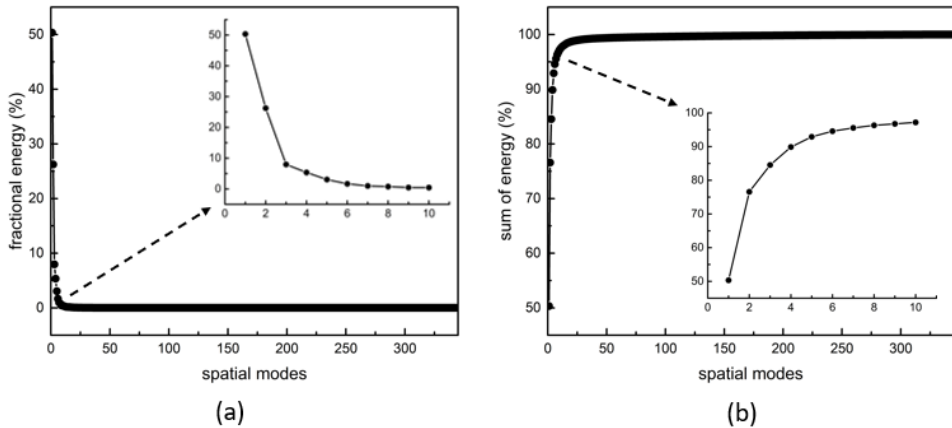


Figure 3.7: (a) Fraction of total kinetic energy and (b) accumulated fraction of total kinetic energy as a function of the number of modes

### 3.3.5. LIMITATIONS

Next, we will address some limitations of the performed experimental study. Firstly, the imposed flow and pressure have a simple sinusoidal variation, which does not represent the diastasis and late filling (A-wave) phases of the LV *in vivo*. Secondly, the blood-mimicking fluid has a 4 times higher viscosity than blood. This could have impact on the flow structure dynamics and corresponding vortex ring formation, pressure, and viscous dissipation rate. In addition, the impact of spatial resolution on the POD analysis has not been investigated. Future study is necessary to quantify its role when applying POD to MRI measurements, considering that MRI technique often has lower spatial resolution than this study. The effect of temporal resolution on POD was studied and the results can be found in the Appendix B. Only 1.0% to 1.6% differences in kinetic energy content were found in the first four modes.

### 3.4. CONCLUSIONS

In this work, we applied Shake-the-Box, an advanced state-of-the-art 3D Lagrangian particle tracking method, to study the flow in a compliant LV model with biological

valves. New features such as particle tracks were extracted and a high spatiotemporal resolution of 4D velocity field was resolved. The 4D relative pressure was calculated using a Poisson equation-based solver. Detailed spatial distribution from the base to the apex and temporal evolution of relative pressure over the cardiac cycle were presented. In general, the obtained flow features and relative pressure are in good agreement with those *in vivo* reports. In addition, we applied POD analysis to decompose the complex velocity data and extract key information about the flow dynamics in LV flows successfully. Our results showed that the first six POD modes captured 95% of the kinetic energy and provided a clear picture of different scales of vortices formed in the pulsatile LV flow, demonstrating that POD can be an alternative approach to efficiently visualize and analyze the various scale flow structures and their temporal behaviors in the LV.

In summary, this work demonstrated that Shake-the-Box and POD analysis are promising tools for the accurate and efficient investigation of highly three-dimensional and time-varying flows. The obtained new features such as particle tracks and 4D relative pressure results can be used to validate *in vivo* or *in silico* LV flows. Clinical image analysis and multi-modality comparison research could benefit from fast, complexity-reduced, and data-reduced POD analysis. Moreover, POD-based metrics can be developed as potential new biomarkers for cardiac function in future work.

### APPENDIX A: VELOCITY PROFILE COMPARISON BETWEEN SHAKE-THE-BOX AND TOMO-PIV

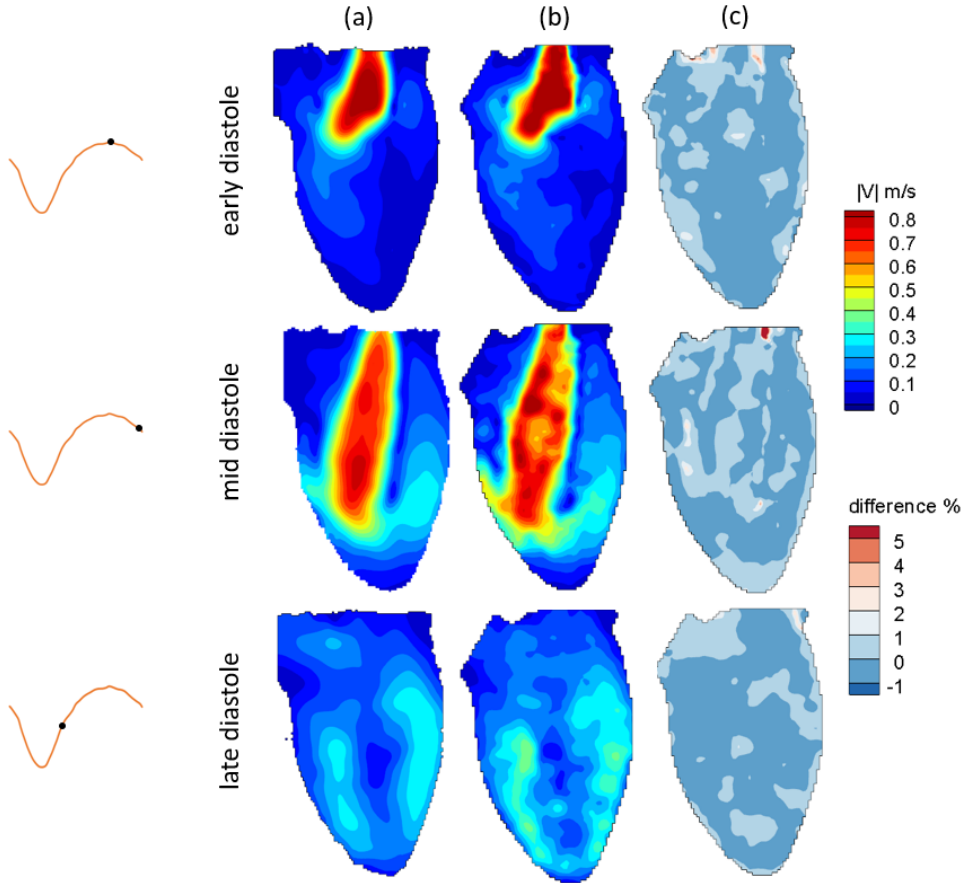


Figure 3.8: (a) STB velocity results at the center z-plane, (b) Tomo-PIV velocity results at the center z-plane, (c) percentage of difference between Tomo-PIV and STB.

The same imaging datasets were used to perform STB and Tomo-PIV analysis. The obtained velocity field of STB gives a higher spatial resolution ( $0.735 \text{ mm}^3$ ) than Tomo-PIV ( $0.98 \text{ mm}^3$ ). It can be seen (Fig. 3.8) that STB showed a better spatial coherence than Tomo-PIV. The velocity difference (Fig. 3.8c) was calculated based on the down-sampled the STB results and Tomo-PIV results. The STB results were interpolated onto the grids of Tomo-PIV. As Fig. 3.8c shows, the velocity difference between STB and Tomo-PIV is mostly below 1%. Only at the inlet, approximately 5% difference was found at the mid-diastole phase.

APPENDIX B: EFFECT OF TEMPORAL RESOLUTIONS ON POD ANALYSIS OF LV FLOW

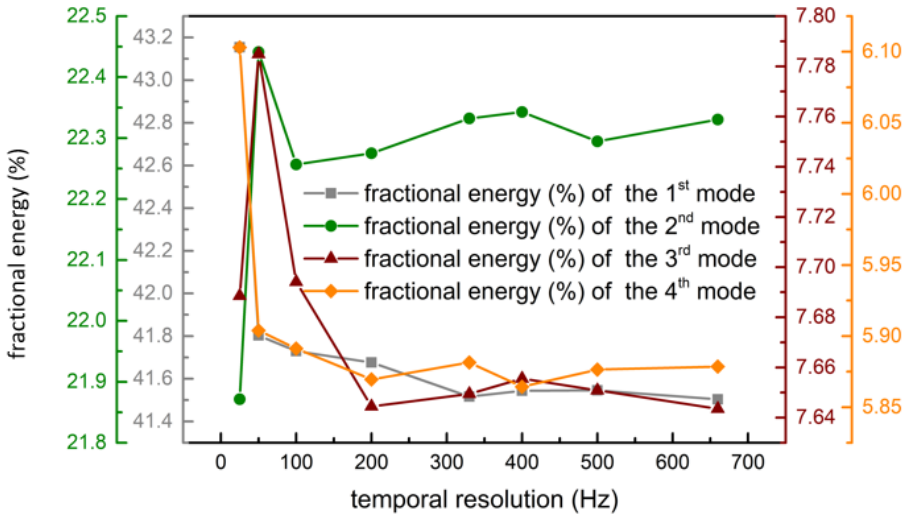


Figure 3.9: Effect of the number of used modes in POD analysis on fractional energy spectra. In snapshot POD, function of mode number corresponding to different frame rates

To examine the sensitivity of the POD results, a statistical convergence test was conducted using data subsets size of 21, 43, 86, 171, 286, 343, 428, and 571 snapshots, corresponding to frame rates of 25, 50, 100, 200, 330, 400, 500, and 660 Hz, respectively. The fractional energy of the first four eigenvalues are plotted as a function of the data size (i.e. number of snapshots) in Fig. 3.9. It reveals that starting from 171 to 571 snapshots (from 200 to 660 Hz frame rate), the magnitude of the fractional energy contributed by the first four eigenvalues does not change significantly, indicating that the present data size (343 snapshots) is sufficiently large for providing statistically converged POD results. Investigating the impact of temporal resolution on POD results is essential step, especially considering applying POD to *in vivo* data analysis. *In vivo* blood flow measurement techniques, such as PC-MRI and echo-PIV, have limited temporal and spatial resolutions comparing to time-resolved PIV system. Our convergence test result shows that a imaging frame rate of 25 to 100 Hz (temporal resolution of 40 to 10 ms), matching the temporal resolution range of PC-MRI measurements, led to a variation of 1.5%, 1.6%, 1.0%, and 1.5% in the kinetic energy content of the first four mode, respectively. If one considers the variations are acceptable, POD could be applied to clinical flow kinetic energy analysis. Together with the low-order reconstruction, flow structures and their temporal behaviors, such as the vortex formation, evolution and convection, can be analyzed in greater detail without requiring high imaging rate data.

# REFERENCES

- [1] A. Bavo, A. M. Pouch, J. Degroote, *et al.*, “Patient-specific CFD models for intraventricular flow analysis from 3D ultrasound imaging: Comparison of three clinical cases”, *Journal of Biomechanics*, vol. 50, pp. 144–150, 2017.
- [2] P. Garg, S. Crandon, P. P. Swoboda, *et al.*, “Left ventricular blood flow kinetic energy after myocardial infarction-insights from 4D flow cardiovascular magnetic resonance”, *Journal of Cardiovascular Magnetic Resonance*, vol. 20, no. 1, p. 61, 2018.
- [3] M. Gharib, E. Rambod, A. Kheradvar, D. J. Sahn, and J. O. Dabiri, “Optimal vortex formation as an index of cardiac health”, *Proceedings of the National Academy of Sciences*, vol. 103, no. 16, pp. 6305–6308, 2006.
- [4] G. Pedrizzetti, F. Domenichini, and G. Tonti, “On the left ventricular vortex reversal after mitral valve replacement”, *Annals of Biomedical Engineering*, vol. 38, pp. 769–773, 2010.
- [5] H. Iwano, D. Kamimura, E. Fox, M. Hall, P. Vlachos, and W. C. Little, “Altered spatial distribution of the diastolic left ventricular pressure difference in heart failure”, *Journal of the American Society of Echocardiography*, vol. 28, no. 5, pp. 597–605, 2015.
- [6] N. Mirvakili, G. Di Labbio, W. Saleh, and L. Kadem, “Flow characteristics in a model of a left ventricle in the presence of a dysfunctional mitral mechanical heart valve”, *Journal of Visualization*, vol. 23, pp. 1–8, 2020.
- [7] A. Falahatpisheh and A. Kheradvar, “High-speed particle image velocimetry to assess cardiac fluid dynamics in vitro: From performance to validation”, *European Journal of Mechanics-B/Fluids*, vol. 35, pp. 2–8, 2012.
- [8] J. Wang, Q. Gao, R. Wei, and J. Wang, “Experimental study on the effect of an artificial cardiac valve on the left ventricular flow”, *Experiments in Fluids*, vol. 58, pp. 1–17, 2017.
- [9] H. Saaid, P. Segers, M. Novara, T. Claessens, and P. Verdonck, “Single calibration multiplane stereo-PIV: The effect of mitral valve orientation on three-dimensional flow in a left ventricle model”, *Experiments in Fluids*, vol. 59, pp. 1–13, 2018.
- [10] D. Hasler, A. Landolt, and D. Obrist, “Tomographic PIV behind a prosthetic heart valve”, *Experiments in Fluids*, vol. 57, pp. 1–13, 2016.
- [11] H. Saaid, J. Voorneveld, C. Schinkel, *et al.*, “Tomographic PIV in a model of the left ventricle: 3D flow past biological and mechanical heart valves”, *Journal of Biomechanics*, vol. 90, pp. 40–49, 2019.

- [12] U. Gülan, B. Lüthi, M. Holzner, A. Liberzon, A. Tsinober, and W. Kinzelbach, “Experimental study of aortic flow in the ascending aorta via particle tracking velocimetry”, *Experiments in Fluids*, vol. 53, pp. 1469–1485, 2012.
- [13] U. Gülan and M. Holzner, “The influence of bileaflet prosthetic aortic valve orientation on the blood flow patterns in the ascending aorta”, *Medical Engineering & Physics*, vol. 60, pp. 61–69, 2018.
- [14] D. Schanz, S. Gesemann, and A. Schröder, “Shake-the-box: Lagrangian particle tracking at high particle image densities”, *Experiments in Fluids*, vol. 57, pp. 1–27, 2016.
- [15] J. L. Lumley, “The structure of inhomogeneous turbulent flows”, *Atmospheric Turbulence and Radio Wave Propagation*, pp. 166–178, 1967.
- [16] A. Darwish, G. Di Labbio, W. Saleh, and L. Kadem, “Proper orthogonal decomposition analysis of the flow downstream of a dysfunctional bileaflet mechanical aortic valve”, *Cardiovascular Engineering and Technology*, vol. 12, pp. 286–299, 2021.
- [17] G. Janiga, “Novel feature-based visualization of the unsteady blood flow in intracranial aneurysms with the help of proper orthogonal decomposition (POD)”, *Computerized Medical Imaging and Graphics*, vol. 73, pp. 30–38, 2019.
- [18] G. H. Chang, C. M. Schirmer, and Y. Modarres-Sadeghi, “A reduced-order model for wall shear stress in abdominal aortic aneurysms by proper orthogonal decomposition”, *Journal of Biomechanics*, vol. 54, pp. 33–43, 2017.
- [19] H. Kirişli, M. Schaap, S. Klein, *et al.*, “Evaluation of a multi-atlas based method for segmentation of cardiac cta data: A large-scale, multicenter, and multivendor study”, *Medical Physics*, vol. 37, no. 12, pp. 6279–6291, 2010.
- [20] C. T. Metz, N. Baka, H. Kirisli, *et al.*, “Regression-based cardiac motion prediction from single-phase CTA”, *IEEE Transactions on Medical Imaging*, vol. 31, no. 6, pp. 1311–1325, 2012.
- [21] D. Schanz, S. Gesemann, A. Schröder, B. Wieneke, and M. Novara, “Non-uniform optical transfer functions in particle imaging: Calibration and application to tomographic reconstruction”, *Measurement Science and Technology*, vol. 24, no. 2, p. 024 009, 2012.
- [22] B. Wieneke, “Iterative reconstruction of volumetric particle distribution”, *Measurement Science and Technology*, vol. 24, no. 2, p. 024 008, 2012.
- [23] B. Van Oudheusden, “PIV-based pressure measurement”, *Measurement Science and Technology*, vol. 24, no. 3, p. 032 001, 2013.
- [24] Y. J. Jeon, D. Michaelis, and B. Wieneke, “Estimation of flow structure transport in TR-PIV data and its application to pressure field evaluation”, in *2nd ‘CFD for PIV’ Workshop*, 2017, p. 21.
- [25] N. Fujisawa, S. Tanahashi, and K. Srinivas, “Evaluation of pressure field and fluid forces on a circular cylinder with and without rotational oscillation using velocity data from PIV measurement”, *Measurement Science and Technology*, vol. 16, no. 4, p. 989, 2005.

- [26] D. Ragni, B. Van Oudheusden, and F. Scarano, “Drag coefficient accuracy improvement by means of particle image velocimetry for a transonic naca0012 airfoil”, *Measurement Science and Technology*, vol. 22, no. 1, p. 017 003, 2010.
- [27] K. E. Meyer, J. M. Pedersen, and O. Özcan, “A turbulent jet in crossflow analysed with proper orthogonal decomposition”, *Journal of Fluid Mechanics*, vol. 583, pp. 199–227, 2007.
- [28] A. Chatterjee, “An introduction to the proper orthogonal decomposition”, *Current science*, pp. 808–817, 2000.
- [29] R. Kalter, M. Tummers, S. Kenjereš, B. Righolt, and C. Kleijn, “Effects of electromagnetic forcing on self-sustained jet oscillations”, *Physics of Fluids*, vol. 26, no. 6, 2014.
- [30] J. O. Dabiri and M. Gharib, “The role of optimal vortex formation in biological fluid transport”, *Proceedings of the Royal Society B: Biological Sciences*, vol. 272, no. 1572, pp. 1557–1560, 2005.
- [31] M. S. Elbaz, E. E. Calkoen, J. J. Westenberg, B. P. Lelieveldt, A. A. Roest, and R. J. Van Der Geest, “Vortex flow during early and late left ventricular filling in normal subjects: Quantitative characterization using retrospectively-gated 4D flow cardiovascular magnetic resonance and three-dimensional vortex core analysis”, *Journal of Cardiovascular Magnetic Resonance*, vol. 16, no. 1, pp. 1–12, 2014.
- [32] J. Jeong and F. Hussain, “On the identification of a vortex”, *Journal of Fluid Mechanics*, vol. 285, pp. 69–94, 1995.
- [33] X. Wu, H. Saaid, J. Voorneveld, *et al.*, “4D flow patterns and relative pressure distribution in a left ventricle model by Shake-the-Box and proper orthogonal decomposition analysis”, *Cardiovascular Engineering and Technology*, vol. 14, no. 6, pp. 743–754, 2023.
- [34] F. Xu and S. Kenjereš, “Numerical simulations of flow patterns in the human left ventricle model with a novel dynamic mesh morphing approach based on radial basis function”, *Computers in Biology and Medicine*, vol. 130, p. 104 184, 2021.
- [35] H. Reul, N. Talukder, E. Mu, *et al.*, “Fluid mechanics of the natural mitral valve”, *Journal of Biomechanics*, vol. 14, no. 5, pp. 361–372, 1981.
- [36] D. Marlevi, M. Balmus, A. Hessenthaler, *et al.*, “Non-invasive estimation of relative pressure for intracardiac flows using virtual work-energy”, *Medical Image Analysis*, vol. 68, p. 101 948, 2021.
- [37] R. B. Thompson and E. R. McVeigh, “Fast measurement of intracardiac pressure differences with 2D breath-hold phase-contrast MRI”, *Magnetic Resonance in Medicine*, vol. 49, no. 6, pp. 1056–1066, 2003.
- [38] S. S. Khalafvand, F. Xu, J. Westenberg, F. Gijzen, and S. Kenjeres, “Intraventricular blood flow with a fully dynamic mitral valve model”, *Computers in Biology and Medicine*, vol. 104, pp. 197–204, 2019.
- [39] M. Courtois, S. J. Kovács Jr, and P. Ludbrook, “Transmitral pressure-flow velocity relation. importance of regional pressure gradients in the left ventricle during diastole.”, *Circulation*, vol. 78, no. 3, pp. 661–671, 1988.

- [40] M. S. Firstenberg, N. G. Smedira, N. L. Greenberg, *et al.*, “Relationship between early diastolic intraventricular pressure gradients, an index of elastic recoil, and improvements in systolic and diastolic function”, *Circulation*, vol. 104, no. suppl\_1, pp. I-330, 2001.
- [41] S. Cimino, G. Pedrizzetti, G. Tonti, *et al.*, “In vivo analysis of intraventricular fluid dynamics in healthy hearts”, *European Journal of Mechanics-B/Fluids*, vol. 35, pp. 40–46, 2012.
- [42] T. Ebberts, L. Wigstrom, A. Bolger, B. Wranne, and M. Karlsson, “Noninvasive measurement of time-varying three-dimensional relative pressure fields within the human heart”, *Journal of Biomechanical Engineering*, vol. 124, no. 3, pp. 288–293, 2002.
- [43] F. Buyens, O. Jolivet, A. De Cesare, *et al.*, “Calculation of left ventricle relative pressure distribution in MRI using acceleration data”, *Magnetic Resonance in Medicine*, vol. 53, no. 4, pp. 877–884, 2005.
- [44] R. Yotti, J. Bermejo, J. C. Antoranz, *et al.*, “A noninvasive method for assessing impaired diastolic suction in patients with dilated cardiomyopathy”, *Circulation*, vol. 112, no. 19, pp. 2921–2929, 2005.
- [45] J. Voorneveld, H. Saaïd, C. Schinkel, *et al.*, “4-D echo-particle image velocimetry in a left ventricular phantom”, *Ultrasound in Medicine & Biology*, vol. 46, no. 3, pp. 805–817, 2020.
- [46] R. S. Reneman, T. Arts, and A. P. Hoeks, “Wall shear stress—an important determinant of endothelial cell function and structure—in the arterial system in vivo: Discrepancies with theory”, *Journal of Vascular Research*, vol. 43, no. 3, pp. 251–269, 2006.
- [47] G. Querzoli, S. Fortini, and A. Cenedese, “Effect of the prosthetic mitral valve on vortex dynamics and turbulence of the left ventricular flow”, *Physics of Fluids*, vol. 22, no. 4, 2010.
- [48] H. Zhang, L. Liu, L. Chen, *et al.*, “The evolution of intraventricular vortex during ejection studied by using vector flow mapping”, *Echocardiography*, vol. 30, no. 1, pp. 27–36, 2013.
- [49] S. Goya, T. Wada, K. Shimada, D. Hirao, and R. Tanaka, “The relationship between systolic vector flow mapping parameters and left ventricular cardiac function in healthy dogs”, *Heart and Vessels*, vol. 33, pp. 549–560, 2018.
- [50] K. Yang, S. Wu, H. Zhang, D. N. Ghista, O. W. Samuel, and K. K. Wong, “Lagrangian-averaged vorticity deviation of spiraling blood flow in the heart during isovolumic contraction and ejection phases”, *Medical & Biological Engineering & Computing*, vol. 59, pp. 1417–1430, 2021.
- [51] V. Vasudevan, A. J. J. Low, S. P. Annamalai, *et al.*, “Role of diastolic vortices in flow and energy dynamics during systolic ejection”, *Journal of Biomechanics*, vol. 90, pp. 50–57, 2019.

- [52] H. Watanabe, T. Sugano, S. Sugiura, and T. Hisada, “Finite element analysis of ventricular wall motion and intra-ventricular blood flow in heart with myocardial infarction”, *JSME International Journal Series C Mechanical Systems, Machine Elements and Manufacturing*, vol. 47, no. 4, pp. 1019–1026, 2004.
- [53] J. H. Seo, V. Vedula, T. Abraham, *et al.*, “Effect of the mitral valve on diastolic flow patterns”, *Physics of Fluids*, vol. 26, no. 12, 2014.
- [54] B. v. Oudheusden, F. Scarano, N. v. Hinsberg, and D. Watt, “Phase-resolved characterization of vortex shedding in the near wake of a square-section cylinder at incidence”, *Experiments in Fluids*, vol. 39, pp. 86–98, 2005.
- [55] A. S. Cruz, L. David, J. Pecheux, and A. Texier, “Characterization by proper-orthogonal-decomposition of the passive controlled wake flow downstream of a half cylinder”, *Experiments in Fluids*, vol. 39, no. 4, pp. 730–742, 2005.
- [56] S. Kefayati and T. L. Poepping, “Transitional flow analysis in the carotid artery bifurcation by proper orthogonal decomposition and particle image velocimetry”, *Medical Engineering & Physics*, vol. 35, no. 7, pp. 898–909, 2013.
- [57] G. Di Labbio and L. Kadem, “Reduced-order modeling of left ventricular flow subject to aortic valve regurgitation”, *Physics of Fluids*, vol. 31, no. 3, 2019.

# 4

## WALL DEFORMATION AND FLOW ANALYSIS IN A PATIENT-SPECIFIC COMPLIANT AORTA MODEL

### AORTIC STRAIN, FLOW PATTERN AND WALL SHEAR STRESS IN A PATIENT-SPECIFIC COMPLIANT AORTA REPLICA USING 4D PARTICLE TRACKING VELOCIMETRY

#### **Introduction**

*High-fidelity in vitro flow simulator in combination with high-dimensional flow visualization techniques can offer precise and comprehensive evaluation of aortic hemodynamics. However, it is particularly challenging to create a fully transparent aorta replica that faithfully mimics the aortic curvature and stiffness.*

#### **Methods**

*In this study, we successfully manufactured a patient-specific compliant aorta phantom with a dilated ascending aorta that can be used in in vitro hemodynamic study. We conducted pulsatile flow measurement on the deformable aorta replica using advanced 4D particle tracking velocimetry – Shake-the-Box. The aortic distensibility, circumferential strain, flow pattern and wall shear stress (WSS) were assessed. Furthermore, the peak velocity field and WSS distribution were compared to in vivo MRI measurements.*

#### **Results**

*We found that the distensibility and circumferential strain of our aortic replica fell within the physiological range of young patients. The aortic diameter changed as much as 5.4 mm*

---

This chapter is based on X. Wu, K. M. B. Jasen, J. J. M. Westenberg, H.J.Lamb, and S. Kenjereš. Aortic Strain, Flow Pattern and Wall Shear Stress in a Patient-specific Compliant Aorta Replica Using 4D Particle Tracking Velocimetry. Submitted.

(42%) in a cardiac cycle and the aortic distensibility was  $9.9 \times 10^{-3} \text{ mmHg}^{-1}$ . In addition, the obtained flow pattern and WSS distribution were found in a good agreement with in vivo MRI measurement.

### **Conclusions**

*In conclusion, the compliant aorta phantom replicated the aortic wall material well. It also faithfully simulated the aortic flow and near-wall hemodynamics. The relatively large lumen dimension change (5.4 mm) in a cardiac cycle suggests the necessity of considering wall deformation in aortic flow simulations. We propose employing this approach for future studies, such as medical treatment training, validation of in silico fluid-structure interaction models, or as a complement to in vivo measurements.*

## 4.1. INTRODUCTION

Aortic Coarctation (CoA) is a congenital narrowing of the aorta artery that causes an increase in the left ventricle workload in order to maintain sufficient blood flow [1]–[4]. After surgical correction, patients may face long-term complications such as aortic aneurysm formation, hypertension, and coronary artery disease [5], [6]. These complications are linked to the hemodynamic environment in the reconstructed aorta, which highly depends on the choice of surgical approach. Therefore, hemodynamic assessment is an important aspect of CoA management for making treatment decisions that leads to successful long-term results.

Precise and comprehensive evaluation of aortic hemodynamics remains a challenge. All methods for analysing blood flow, such as *in vivo* and *in vitro* measurements, and *in silico* modelling, have their limitations. *In vivo*, the measurement accuracy is constrained by invasiveness, patient movement, artifacts, or insufficient spatial/temporal resolution [7], [8]. *In silico* and *in vitro* approaches have been adopted to complement *in vivo* measurements by providing high-resolution data with fewer of these restrictions. Nonetheless, accurately replicating the precise hemodynamic environment poses numerous challenges, including the faithful reconstruction of realistic geometry, physiological flow conditions, compliant vessel walls, and non-Newtonian fluid properties. These characteristics play important roles in the aortic hemodynamics and yet are challenging to reproduce them.

In *in vitro* experiments, many works have conducted under the assumption of rigid walls, [9]–[11]. However, ignoring the elastic behavior of the aorta can lead to an overestimation of velocity, wall shear stress (WSS), and pressure field [12]. Nowadays, there is a shortage of experimental data for validating computational fluid-structure interaction (FSI) modeling. Only a few experimental works on compliant phantoms are available, which were mostly conducted in simplified geometries and under 2D techniques, i.e., planar and stereoscopic particle imaging velocimetry (PIV) [13]–[15]. Due to the high three-dimensionality of aortic flows, 3D technique is naturally more desirable than 2D techniques.

In literature, 3D techniques, such as tomographic PIV (Tomo-PIV) and 3D particle tracking velocimetry (3D PTV), have been applied to compliant aortic root phantoms [16]–[18]. However, to state, the state-of-art 3D optical flow measurement technique is the Shake-the-Box. Shake-the-Box is a novel Lagrangian particle tracking (LPT) algorithm [19]. It enables temporal-spatial particle reconstruction for high seeding density (up to 0.125 ppp) flows at very low ghost particles occurrence ( $< 0.004\%$  false particles) and high accuracy (average position error of 0.018 pixel) [19]. This is a considerable improvement in both accuracy (compared to 3D PTV and Tomo-PIV) and the applicable seeding density (especially in relation to 3D PTV). STB has been successfully applied to a compliant left ventricle [20] and a rigid aortic root [21]. It has not been adopted for measuring the flow in a realistic shaped compliant aorta model. The goal of this study is to fill this gap by manufacturing a low-cost patient-specific compliant aorta phantom and conducting *in vitro* flow assessment on it using Shake-the-Box. We fabricated a compliant silicone phantom of a child patient's thoracic aorta, which underwent surgical repair of CoA and later on developed a complication of a dilated ascending aorta. Pulsatile flow experiment was then carried out using STB technique. Based on the reconstructed particle tracks, we

assessed the aortic strain and its hemodynamic parameters, such as velocity, WSS, time-averaged WSS (TAWSS), and oscillatory shear index (OSI). The results were compared with the *in vivo* MRI measurements, demonstrating the promise of this approach for high-fidelity *in vitro* hemodynamic investigation.

## 4.2. MATERIAL AND METHODS

### 4.2.1. COMPLIANT AORTA MODEL

#### MRI ACQUISITION AND GEOMETRY PRE-PROCESSING

The aorta geometry in this study was reconstructed from MRI images of a patient (Female, 9 years old) who underwent CoA repair at the age of 1 year. The image acquisition was performed on a 3T scanner (Ingenia, Philips Healthcare, Best, The Netherlands) at Leiden University Medical Center, using a hemidiaphragm respiratory navigator, a retrospective ECG gating, and a standard non-symmetrical four-point velocity encoding. Additional sequence parameters can be found in Table 4.1. The lumen of the aorta was segmented using CAAS MR Solutions v5.0 (Pie Medical Imaging, Maastricht, The Netherlands). The segmentation details can be found in [22]. For experimental use, we shortened the descending aorta. The initial surface and final surface are shown in Fig. 4.1a and b.

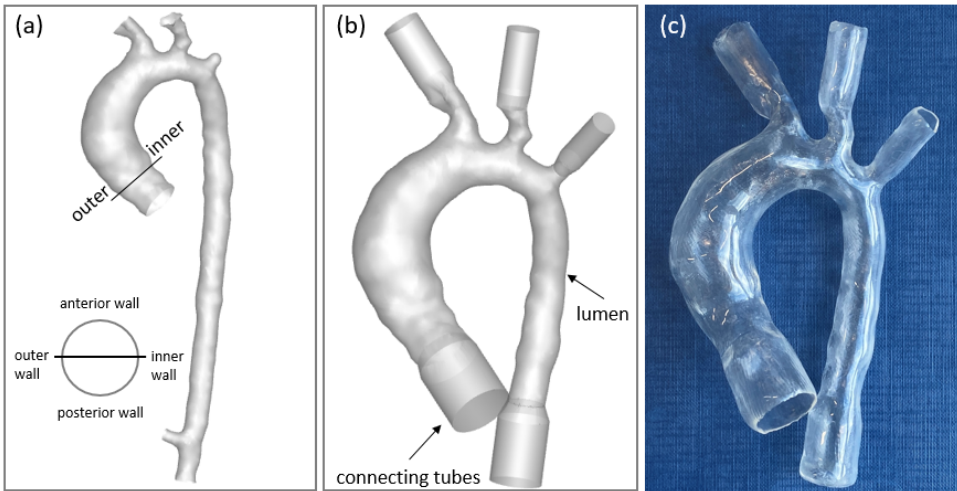


Figure 4.1: (a) Initial lumen surface obtained from 4D-flow MRI. (b) Final geometry used for *in vitro* experiments. (c) manufactured compliant aorta phantom (1 mm thickness).

#### COMPLIANT AORTA PHANTOM MANUFACTURING

For *in vitro* PTV experiment, we utilized a brush-spin-heat coating method to fabricate a transparent aorta phantom that mimics the curvature and elasticity of the patient's aorta. The aorta was firstly 3D printed with ABS material, polished and then wetted with silicone gel (Sylgard 184, 10:1 mix ratio, 30 mL) by brushing. Rotate the wetted model in a stepper motor (see in Appendix 4.5) for 5 minutes at 30 rad/min and remove the excessive silicone gel droplet with a painting brush (hair width 2 mm). The coated model was then cured

Table 4.1: Details of 4D-flow MRI sequence

Parameters	Unit	Values
Field of view	[mm <sup>3</sup> ]	350 × 350 × 62.5
Acquisition spatial resolution	[mm <sup>3</sup> ]	2.5 × 2.5 × 2.5
Reconstructed temporal resolution	[ms]	29.2
Velocity encoding	[cm/s]	200
Echo time	[ms]	2.4
Repetition time	[ms]	4.3
Flip angle	[°]	10
Acquisition time	[min]	4.9
Segmentation factor	[-]	2
Sensitivity encoding factor	[-]	2

at heating temperature of 70 °C for 15 minutes. It should be noted that for forming an uniform thickness, it is important to rotate the model while curing it. After 13 repetitions of this brush-spin-heat process, a  $1 \pm 0.15$  mm silicone film was achieved, which was 0.6 times of the reported physiological thickness ( $1.7 \pm 0.3$  mm) [23]. The final silicone model (Fig. 4.1c) was obtained by dissolving the 3D-printed ABS core with acetone. The circumferential thickness measured at 16 cross-sections ranged from 0.84 mm to 1.13 mm (variation below 15%). Notably, this method required only 30 mL of silicone gel (120 €/kg), offering a significantly more affordable option compared to purchasing a customized phantom from commercial companies (~5000€).

#### TENSILE TESTS

We performed uniaxial tensile testing using a TA-Instruments Q800 tensile tester on five rectangular samples obtained from a spared aorta phantom. It was identical to the one used in STB measurements (same geometry, silicone, and manufacturing method). The Young's modulus was calculated from the stress-strain region between 5% to 40% where remains the linear elastic region. The average Young's modulus was 0.93 MPa, falling within the reported physiological range (0.46 - 1.60 MPa) for the human thoracic aorta. However, it is approximately 1.6 times that of young patients (0.585 MPa) [23].

### 4.2.2. EXPERIMENTAL SETUP

#### BLOOD-MIMICKING FLUID

In this study, a water-glycerol-urea mixture was used as blood-mimicking fluid. This working fluid has a density of  $\rho = 1130$  kg/m<sup>3</sup> and a dynamic viscosity of  $\mu = 0.0040$  Pa·s at 25 °C. By tuning the concentration of water/glycerol/urea (47%/27%/26%), the refractive index ( $n=1.413$ , Bleeker Zeist Holland refractometer) was matched with the silicone phantom.

#### FLOW LOOP

The circulatory mock loop in Fig. 4.2c supplied flow through the aortic phantom. To simulate the *in vivo* pulsatile flow, a left ventricular assist device (VAD) (Berlin Heart EXCOR) and a MEDOS VAD driving system were used. The VAD, with a stroke volume

of 60 mL, operated under tailored physiological settings to achieve the maximum flow rate (Fig. 4.2d): 40 bpm, a duty cycle of 35%, systolic pressure of 180 mmHg, and diastolic pressure of 0 mmHg. The temperature of the working fluid was maintained at 25 °C using a thermostat tank.

### IMAGING SYSTEM

The STB imaging system (Fig.4.2a-b) consisted of two high-speed CMOS cameras (Imager Pro HS 4 M, PCO, Kelheim, Germany) and customized image splitters to capture particle images from four different viewing angles (angular aperture 108°). The flow was seeded with fluorescent particles (PMMA-RhB coated PMMA, diameter 25-50  $\mu\text{m}$ , density 1100  $\text{kg}/\text{m}^3$ ). The particle image density is 0.05 particles per pixel (ppp). A volume ( $110 \times 150 \times 46 \text{ mm}^3$ ) that covers the entire aorta was illuminated by a double pulsed Nd: YLF laser (LDY304, Litron Lasers, England).

4

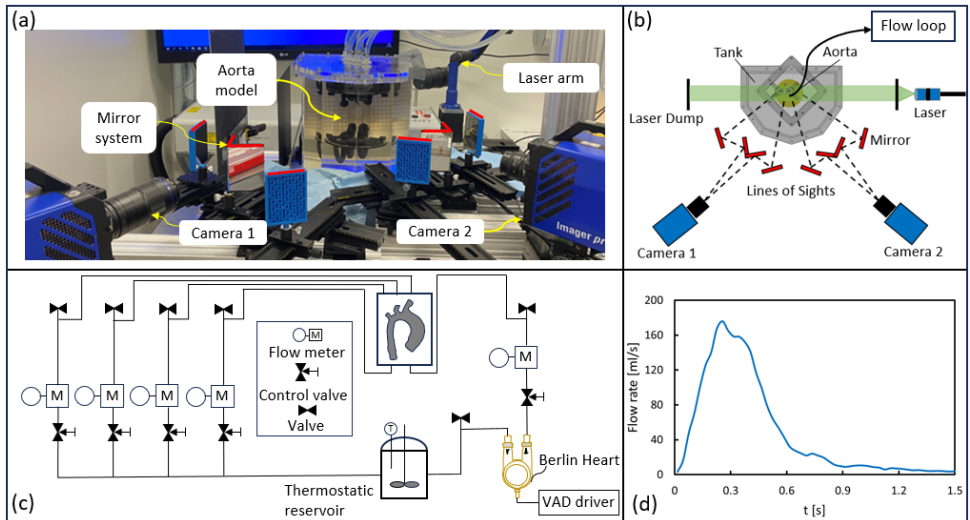


Figure 4.2: (a) Imaging system (front view) of the *in vitro* experiment, including the aorta phantom, laser optics, two CMOS cameras, and an image splitter mirror system. (b) The top view of the imaging system (sketch). (c) Schematic sketch of the flow loop. (d) The flow waveform imposed at the inlet.

### 4.2.3. DATA ACQUISITION AND SHAKE-THE-BOX ANALYSIS

#### DATA ACQUISITION

All image acquisition, processing, and analysis were carried out in DaVis 10.1 (LaVision, Göttingen, Germany). Particle images of 10 cardiac cycles were recorded at an imaging rate of 2 kHz and underwent pre-processing, including geometric masking, a history-minimum-background subtraction, Gaussian smoothing, and sharpening. Camera calibration was firstly done by mapping the calibration marks on a 3D plate to the 2D camera sensor plane. A third-order polynomial mapping function was used, resulting in a fitting error of approximately 0.5 pixel ( $\sim 47 \mu\text{m}$ ). Subsequently, this mapping function was refined to an error below 0.03 pixel by volumetric self-calibration based on

pre-processed particle images. For STB analysis, the particles' optical transfer function (OTF) [24] calibration was also conducted. OTF facilitates the detection of 3D particle positions in the 'shaking' process.

#### SHAKE-THE-BOX ANALYSIS

STB was first introduced in 2013 [25] and has been applied to the bio-flow field in recent years [20]. STB uses an advanced particle tracking scheme – iterative triangulation and image matching (shaking) [26] for reconstructing particle positions in a 3D space domain. In our study, an intensity threshold of 10 counts and an allowed triangulation error of 1 voxel were specified for particle detection. Particle position refinement was done by shaking the particle by 0.1 voxel in space and in 8 iterations. The converged solution contains approximately 1250-5200 active particle tracks from diastole to systole phase.

#### 4D VELOCITY CALCULATION

In order to retrieve velocity (and acceleration) information, the particle tracks were firstly fitted with a second-order B-spline function. The velocity and acceleration were extracted as the first and second derivatives of that function. Subsequently, the resulting velocity field from this discrete particle-based data was interpolated onto the Eulerian grid using binning with Gaussian weighting. The binning has a sub-volume of 48 voxel with an overlap of 87.5%, resulting in a final grid size of 6 voxel (0.56 mm<sup>3</sup>) in each dimension. This spatial resolution is higher than the previous study (0.75 mm<sup>3</sup>) based on 3D PTV measurements [16].

#### 4.2.4. POST-PROCESSING

In this study, strain (the diameter change) and distensibility were calculated to evaluate the arterial stiffness of the aorta replica. The diameter of the lumen was estimated by a binary mask applied in the velocity field. The binary mask has a value of 1 wherever a vector exists and a value of 0 where a vector does not exist. The strain represents the relative change in diameter. The distensibility was defined as [27]:

$$Distensibility = \frac{A_{max} - A_{min}}{A_{min}(P_{max} - P_{min})} \quad (4.1)$$

where  $A_{max}$  and  $A_{min}$  are the maximum and minimum aortic lumen areas.  $P_{max}$  and  $P_{min}$  are the corresponding pressures. The post-processing of near-wall hemodynamics includes wall shear stress (WSS) and its time derivatives - TAWSS and OSI. The TAWSS is the time-averaged magnitude of WSS over a cardiac cycle:

$$TAWSS = \frac{1}{T} \int_0^T |\vec{\tau}_w| dt \quad (4.2)$$

where  $T$  is the length of a cardiac cycle, and  $\vec{\tau}_w$  is the wall shear stress. The OSI is defined as:

$$OSI = \frac{1}{2} \left( 1 - \frac{\left| \int_0^T \vec{\tau}_w dt \right|}{\int_0^T |\vec{\tau}_w| dt} \right) \quad (4.3)$$

WSS was estimated by mapping the velocity gradient from the measured data to the surface geometry by inversed-distance weighted interpolation. To calculate TAWSS and OSI, the WSS from different time instants were interpolated to the peak-systole geometry. This method for estimating near-wall quantities has been successfully applied in our previous study [11].

## 4.3. RESULTS

### 4.3.1. PARTICLE TRACKS

An instantaneous snapshot of particle positions at peak systole is shown in Fig. 4.3b. At peak systole, approximately 5200 particles were reconstructed and tracked. The particle tracks with a tracking length of 13 time-steps are shown in Fig. 4.3c. The particle and particle tracks are colored by the velocity magnitude. The maximum flow velocity is approximately 1 m/s.

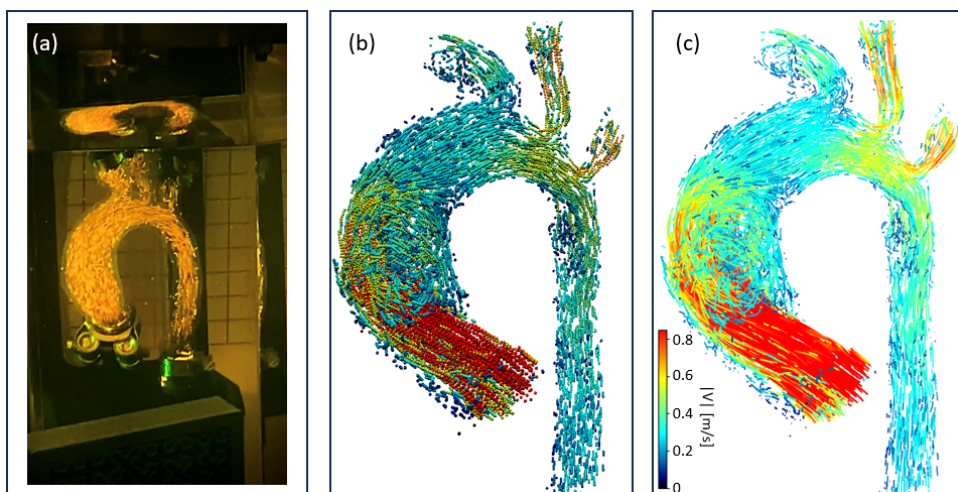


Figure 4.3: (a) A picture of the particle image of the aortic flow. (b) Particles at an instantaneous time step reconstructed from the Shake-The-Box algorithm. (c) Particle tracks of 13 consecutive time steps.

### 4.3.2. AORTIC WALL DEFORMATION

It was evident that the aorta contracts and expands with the pulsation of the VAD system. In Fig. 4.4, we presented the contour edge of five representative cross-sections during peak systole and early diastole. The non-uniform nature of deformation, particularly in the ascending aorta and aortic arch, is observed. It is mainly the outer curvature that expands or contracts. The maximum cyclic diameter changes, strain, and distensibility were calculated on an average of fifteen cross-sections. The maximum diameter change and strain are summarized in Table 4.2. The maximum aortic diameter change was 3.8 - 7.2 mm in a cardiac cycle. The circumference strain was on average 42 %. The averaged distensibility of the aorta phantom was  $9.9 \times 10^{-3} \text{ mmHg}^{-1}$ .

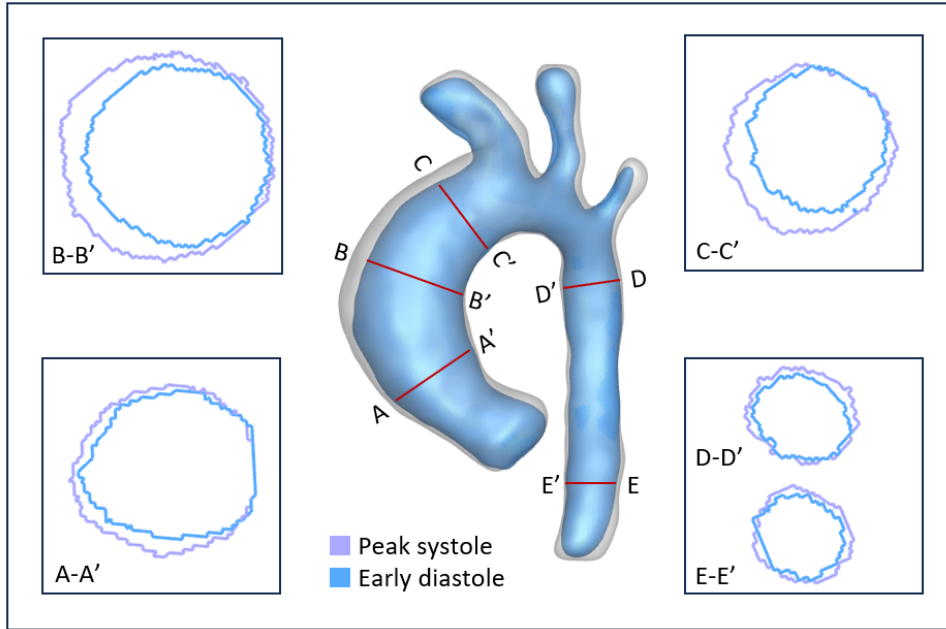


Figure 4.4: The contour edge of five cross-sections at peak systole (purple) and early diastole (blue).

Table 4.2: Details of 4D-flow MRI sequence

Parameters	Unit	Values
Wall thickness	[mm]	$1 \pm 0.15$
Young's modulus	[MPa]	0.93
Systolic pressure	[mmHg]	150
Diastolic pressure	[mmHg]	62
Cyclic diameter change	[mm]	$5.4 \pm 1.9$
Strain	[%]	$42 \pm 1$
Distensibility	$[\text{mmHg}^{-1}, 10^3]$	$9.9 \pm 2$

### 4.3.3. FLOW PATTERNS

The 3D flow patterns with time evolution are visualized by 3D streamlines at four key-frames of the cardiac cycle (i.e. mid acceleration, peak systole, mid deceleration, and early diastole), shown in Fig. 4.5. It can be seen that a highly eccentric inflow jet impinged the posterior wall of ascending aorta, with parts of the jet rolling up and forming vortices in the middle of ascending aorta. These vortex structures travel along the inner curvature towards the posterior wall of the branches and descending aorta with time, persisting till the start of diastole. Helical flow is also observed at the descending aorta, appearing at the mid-acceleration and becoming more dominant in the late deceleration and early diastole stages.



Figure 4.5: 3D streamlines of the aorta phantom at four key-frames of the cardiac cycle (mid acceleration, peak systole, mid deceleration, and early diastole), colored by velocity magnitude.

4

#### 4.3.4. WSS, TAWSS, AND OSI

Fig. 4.6 displays the spatial distributions of systolic WSS, TAWSS, and OSI. High WSS and TAWSS are observed at the area (yellow) of the inlet, posterior wall of the ascending aorta, arch, and posterior wall of the descending aorta. The highest WSS (4.5 Pa) and TAWSS (1.2 Pa) are found in the proximity of the inlet. Localized areas of high OSI ( $> 0.45$ ) appear in the marked areas (black) in Fig. 4.5 where the vortex and helix flows were formed. It can be observed that these high OSI areas exhibit low WSS/TAWSS values.

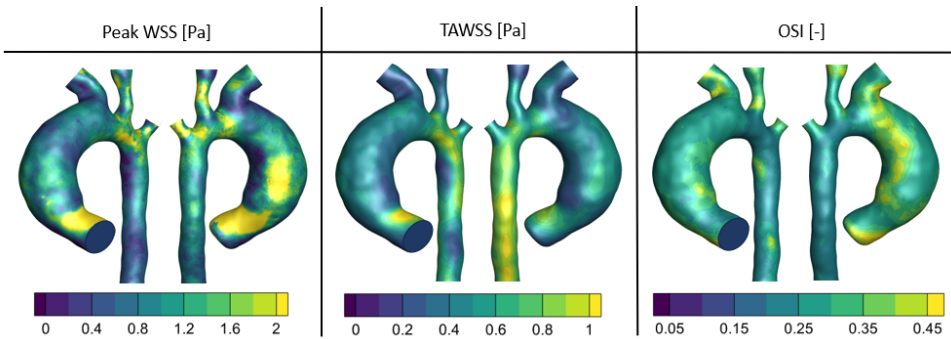


Figure 4.6: Peak wall shear stress (WSS), time-averaged WSS, and oscillatory shear index (OSI) of the aorta phantom.

#### 4.3.5. COMPARISON WITH 4D-FLOW MRI

To assess our methods, we qualitatively compared results with *in vivo* 4D-Flow MRI measurements. Fig. 4.7 presents the comparison of flow patterns, velocity at a central plane, and WSS distribution at peak systole between STB and 4D-Flow MRI. Due to differences in inflow waveforms, velocity, and WSS values were normalized by the maximum inlet value for comparison. The obtained flow patterns closely resemble *in vivo* flow, and the velocity at the central plane is also in reasonable agreement. Additionally, the spatial

distribution of peak WSS is generally consistent, although STB indicates a larger area of high WSS at the posterior ascending aorta, while 4D-Flow MRI shows higher WSS at the posterior descending aorta.

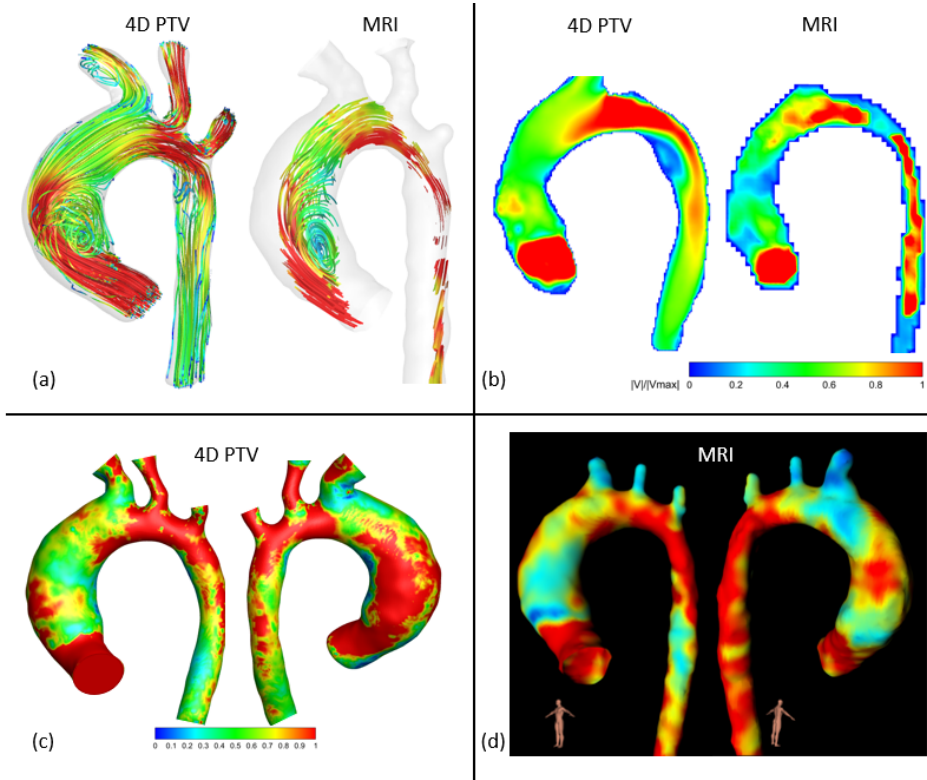


Figure 4.7: Comparison of the peak systole results between 4D PTV (Shake-The-Box) and *in vivo* 4D-flow MRI measurements: (a) flow patterns, (b) velocity in the central vertical plane, and (c) & (d) Normalized WSS ( $WSS/WSS_{inlet}$ ).

## 4.4. DISCUSSION

Studies have demonstrated the necessity of enhancing the bio-fidelity of *in vitro* and *in silico* hemodynamic modeling in understanding its relation with the pathogenesis and progression of cardiovascular disease [13]–[15], [28], [29]. Manufacturing accurate artery models that replicate vessel elasticity while maintaining optical transparency is challenging, especially for patient-specific models with complex, tortuous surfaces. Thickness control, identified as a big challenge in complex vascular geometries by previous studies [30]–[32], often led to the use of simplified geometries in *in vitro* experiments [33], [34]. Although a couple of exceptions involved the creation of more intricate and comprehensive vascular models [30], [31], no flow measurements were conducted. To our knowledge, this is the first study to manufacture a patient-specific, fully transparent, compliant, and

low-cost aorta model, and also conduct flow measurements on it using advanced 4D particle tracking velocimetry – Shake-the-Box. Detailed analysis on flow (velocity, WSS, TAWSS, OSI) and wall deformation (strain, distensibility) was also provided.

#### 4.4.1. AORTIC STRAIN AND DISTENSIBILITY

Arterial stiffness is an important predictor of many cardiovascular events. It can be accessed by strain, strain, and distensibility. We found an average maximum diameter change of  $5.4 \pm 1.9$  mm in a cardiac cycle, which is comparable to studies [28], [29] reporting a lumen dilation of 5 mm. The obtained strain (42%), and the distensibility in ascending and descending aorta ( $9.9 \times 10^{-3}$  mmHg<sup>-1</sup>) align closely with those obtained by Redheuil et al [27], derived noninvasively from MRI measurements of 122 patients. A strain of  $33 \pm 8\%$  and a distensibility of  $9.8 \times 10^{-3}$  mmHg<sup>-1</sup> in ascending aorta and  $9.6 \times 10^{-3}$  mmHg<sup>-1</sup> in descending aorta were reported in the young patient group (20-29 years). Redheuil et al [27] also reported that ascending aortic strain and distensibility decreased by 5.3% and  $1.8 \times 10^{-3}$  mmHg<sup>-1</sup>, respectively, for each decade of age. It was in accordance with several other studies, which reported approximately 10% -15% of strain in aged patients ( $\geq 50$  years) with abdominal aortic aneurysms [33], [35]. The elasticity of the patients varies greatly depending on the physiological conditions. This notion should be considered when interpreting various reported data on aortic dimension changes, compliance, and pulse wave velocity.

#### 4.4.2. FLOW PATTERNS AND WSS DISTRIBUTION

Hemodynamics are coupled with vascular remodeling and functionality. An abnormal hemodynamic environment can stimulate local vessel wall restructuring, leading to atherosclerosis, aneurysm formation, and dissections. Vessel morphology, in turn, impacts blood flow and hemodynamic forces [36], [37]. The aorta geometry used in this study has a dilated ascending aortic lumen (Fig. 4.1). The diameter ratio between the ascending and descending aorta is approximately 2. This has led to the particular systolic flow patterns shown in Fig. 4.3 and Fig. 4.5. The observed eccentric inflow jet, helical flow, and strong vortical flow align with flow patterns typically seen in patients with aortic valve stenosis, aortic dilation but normal tricuspid valve, or in patients with normal aortic dimension and bicuspid aortic valve [38]–[41].

Flow-derived parameters such as WSS and OSI distribution can also offer important insights into aortic remodeling. Elevated WSS can cause extracellular degradation and aortic wall thinning. Local high WSS can be used as a bio-maker to predict aortic dilation [42]. On the other hand, low WSS and high OSI together are linked to atherosclerosis [43]. In our case, localized high WSS is the result of wall impingement of the deflected jet flow and the sudden diameter change in the aortic arch and descending aorta. Low WSS and high OSI regions are at the ascending aorta where the vortical flow is located, Fig. 4.6. The presented systolic WSS distribution and magnitude are in accordance with similar patient cases as reported in [39], [44].

#### 4.4.3. AGREEMENT BETWEEN *In vitro* AND *In vivo* DATA

We compared our flow measurements with the patient's *in vivo* MRI measurements. The peak flow patterns and peak WSS show a qualitative agreement between *in vitro* model

and *in vivo* MRI measurements, Fig. 4.7. It is important to note that the eccentricity of the aortic jet is simulated in our experiment without modeling the leaflets. This suggests that the leaflet orifice diameter in relation to the ascending aorta diameter plays a major role in the jet flow angle. Similar findings were reported in [44], [45].

#### 4.4.4. LIMITATIONS

The current aorta was modeled as a linear elastic phantom with isotropic wall thickness and Young's modulus, while the human aorta has a non-uniform wall thickness and different Young's modulus in the circumferential and longitudinal direction. It could have an impact on the resulting flow and shear stress. However, when compared our flow measurements to the patient's *in vivo* 4D Flow MRI measurements, no significant discrepancies in flow patterns were observed. Newtonian fluid was used as blood-mimicking fluid, which neglected the non-Newtonian blood rheology. The non-Newtonian effects could influence the vortex formation, the magnitudes of velocity and shear rates. Controversial conclusions regarding the impact of non-Newtonian effect on blood flow in large arteries emerged in literature (both significant and negligible impacts were reported) [33], [35]. Finally, due to limitations of our pump system, we were not able to recreate the identical MRI-measured patient-specific waveform. This prevented a direct quantitative comparison between the MRI and STB measurements.

## 4.5. CONCLUSIONS

In this study, we manufactured our own patient-specific, fully transparent, and compliant aorta model utilizing a brush-spin-heat coating method. Furthermore, we conducted time-resolved 3D flow measurements in the aortic phantom using advanced 4D particle tracking velocimetry – Shake-the-Box technique. Velocity, wall shear stress, and its time derivatives (TAWSS, OSI) were calculated. Based on the high spatiotemporal resolution velocity field, we assessed the cyclic diameter change and distensibility of the aorta model. The aortic strain and distensibility agreed well with the physiological values of young patients reported in past *in vivo* studies. We also compared the flow field with *in vivo* 4D-Flow MRI measurements. A reasonable agreement in peak flow pattern and wall shear stress distribution was observed, demonstrating the high bio-fidelity of our method. Therefore, this work illustrated the feasibility of manufacturing a complex and compliant artery model that not only mimics the mechanical behavior of blood vessels but also is well-suited for advanced optical flow measurements. This can increase the availability of experimental data for validating computational models such as fluid-structure interaction.

## APPENDIX A: MANUFACTURE OF THE COMPLIANT AORTA PHANTOM

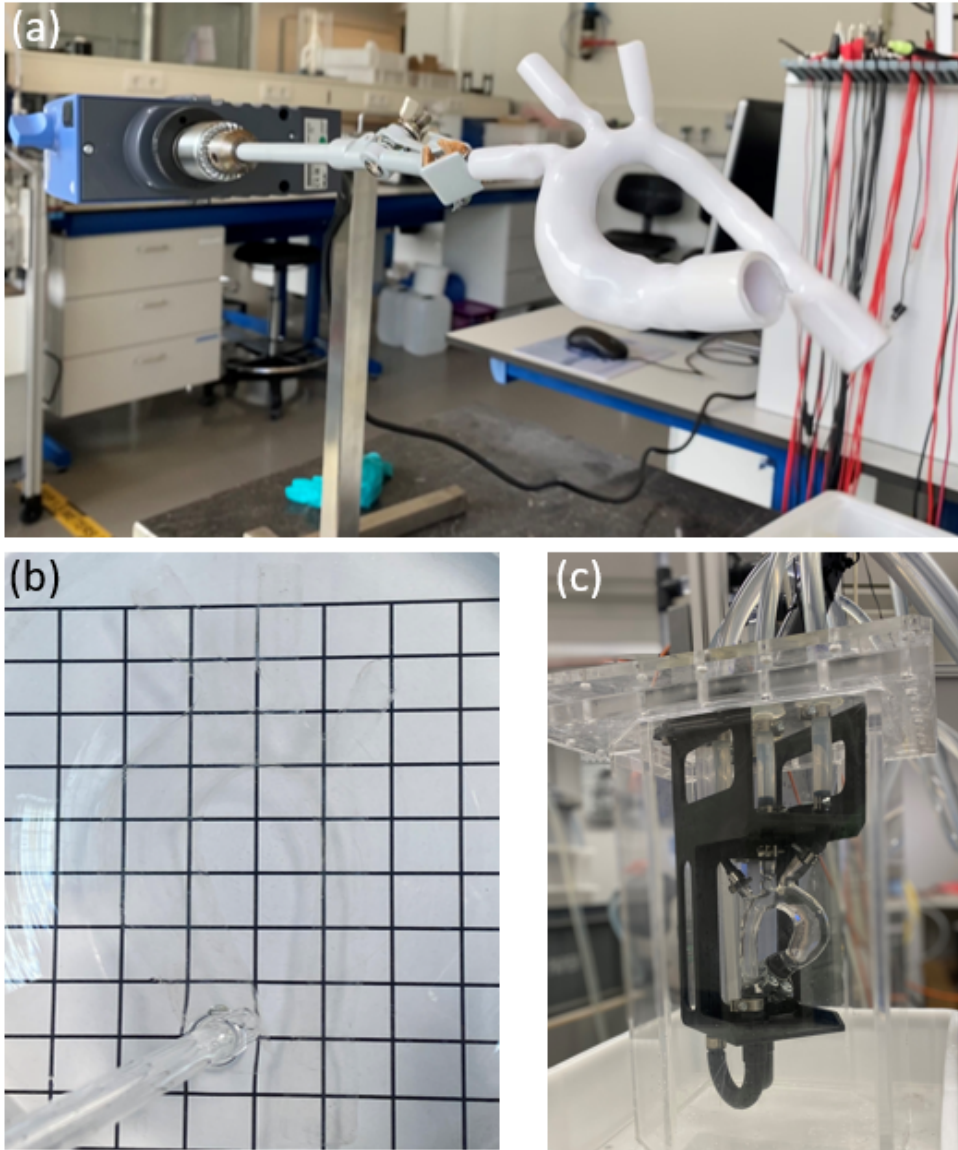


Figure 4.8: (a) the wetted 3D printing of aorta is rotated by the stepper motor. (b) the refractive index of the silicone aorta phantom is matched with the working fluid. (c) the silicone phantom was mounted on a rigid box for fixing its position, limiting its 3D movement in space.

The model manufacturing process are as follows: the aorta was firstly 3D printed using ABS (Acrylonitrile Butadiene Styrene) material by Fortus 450MC (Stratasys, Israel) machine. The 3D-printed model was polished with sandpaper and then wetted with

silicone gel (Sylgard 184, 10:1 mix ratio) by brushing. Next, the wetted model was spinning for 5 minutes at a rotation speed of 30 rad/min in a stepper motor (Fig. 4.8a). Once stop rotating, excessive silicone droplets would be formed quickly at the bottom edge. Remove them by gently brushing them away. Repeat this step a few times until no excessive silicone gel droplet accumulated anywhere. The coated model was then cured at heating temperature of 70 °C for 15 minutes. Please note that it is important to keep the model spinning during the curing process. This brush-spin-heat process was repeated 13 times. The compliant silicone model was refractive index-matched to the working fluid (Fig. 4.8b). To mount the silicone model for measurement setup, we designed a mounting box (Fig. 4.8c) to limit the free-movement of the aorta 3D space position. This design ensures only the aortic wall movements like expansion and contraction.

## APPENDIX B: THICKNESS QUANTIFICATION OF THE COMPLIANT AORTA PHANTOM

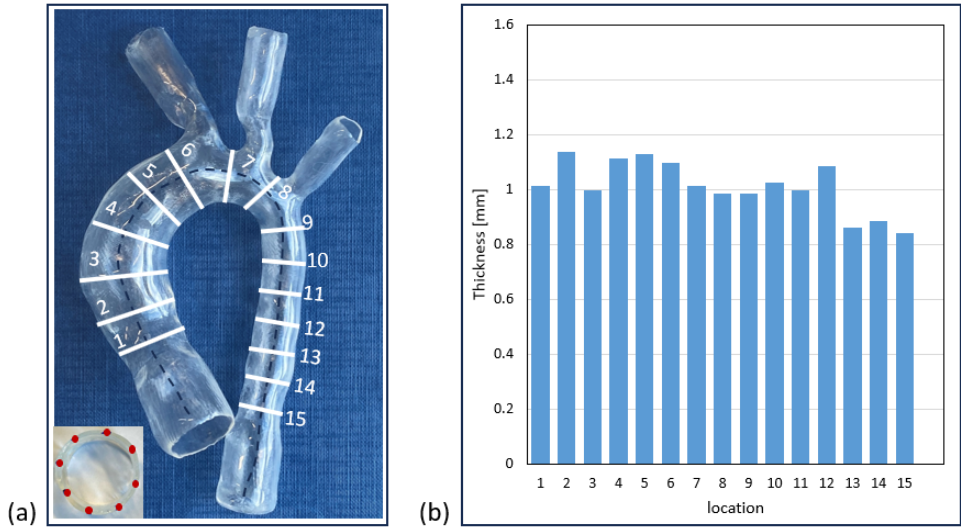


Figure 4.9: (a) Indication of 15 thickness detection positions along the pathline and 8 regularly distributed points for circumferential thickness measurements. (b) The circumferential averaged thickness of 15 silicone rings.

To quantify the thickness of the manufactured aorta, we cut the aorta along the pathline into 15 rings (1 cm long). The cut positions are indicated in Fig. 4.9a. For each ring, the thickness was measured by a caliper (accuracy of  $\pm 0.02$  mm) and averaged at 8 evenly distributed points, as indicated in Fig. 4.9a. The resulted thickness of each silicone ring are shown in Fig. 4.9b. As we mentioned in section 4.2.1, the average thickness of the compliant model was  $1 \pm 0.15$  mm.

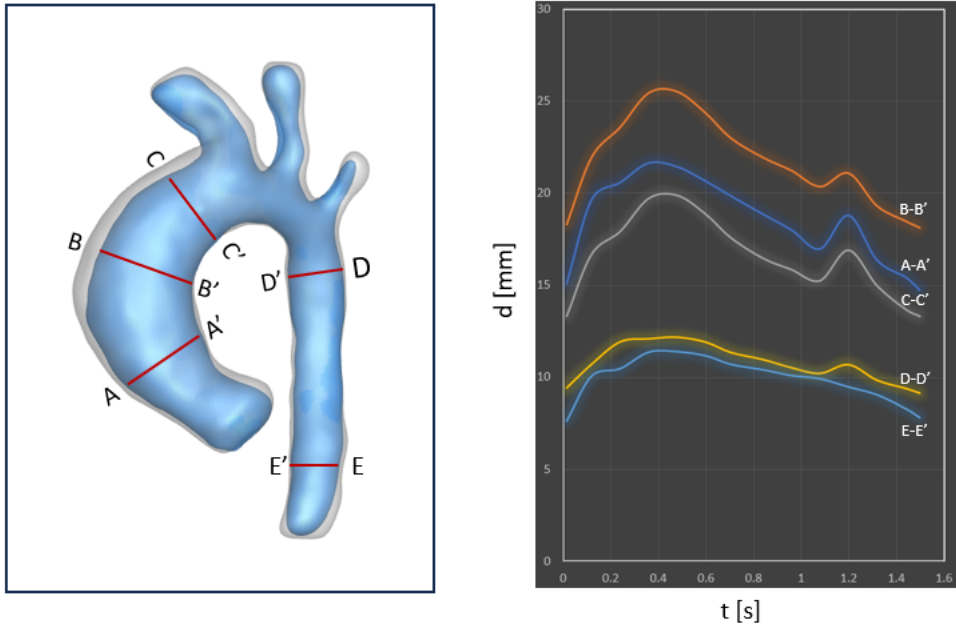
**APPENDIX C: TIME-EVOLUTION OF THE INTERNAL DIAMETER CHANGE OF FIVE REPRESENTATIVE CROSS-SECTIONS**

Figure 4.10: Time-evolution of internal diameters (right) at five representative cross-sections (left).

## APPENDIX D: RELATIVE PRESSURE OF THE AORTA

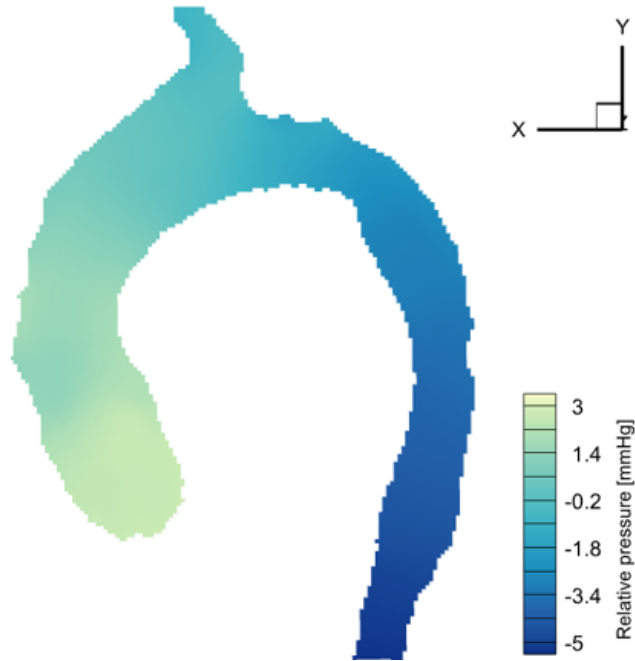


Figure 4.11: Relative pressure distribution at the central z-plane

Pressure gradients serve as a critical clinical indicator for assessing the severity of cardiovascular diseases, such as aortic valve stenosis and aortic coarctation [46], [47]. We reconstructed the 4D relative pressure in the aorta noninvasively based on the velocity field. Based on the obtained velocity, 4D pressure distribution in the aorta phantom was calculated using a Poisson equation-based pressure solver. Detailed information of the 4D pressure solver can be found in our previous publication [20]. A combination of Dirichlet boundary (an average zero value of the measured domain as a reference) and Neumann boundary conditions (pressure gradient at all boundary voxels) was prescribed. The resulted relative pressure contour of peak systole at a central plane is shown in Fig. 4.11. The peak pressure dropped by 7.5 mmHg between the cross-section A-A' (Fig. 4.10left) at ascending aorta and cross-section E-E' (Fig. 4.10left) at descending aorta. This is in a good agreement with previous *in vitro* MRI study (7 mmHg) [48] and *in vivo* MRI flow-based studies ( $4.7 \pm 1.8$  mmHg,  $5.3 \pm 2.37$  mmHg) [46], [47].

APPENDIX E: VELOCITY AT CROSS-SECTIONS PERPENDICULAR TO THE PATHLINE

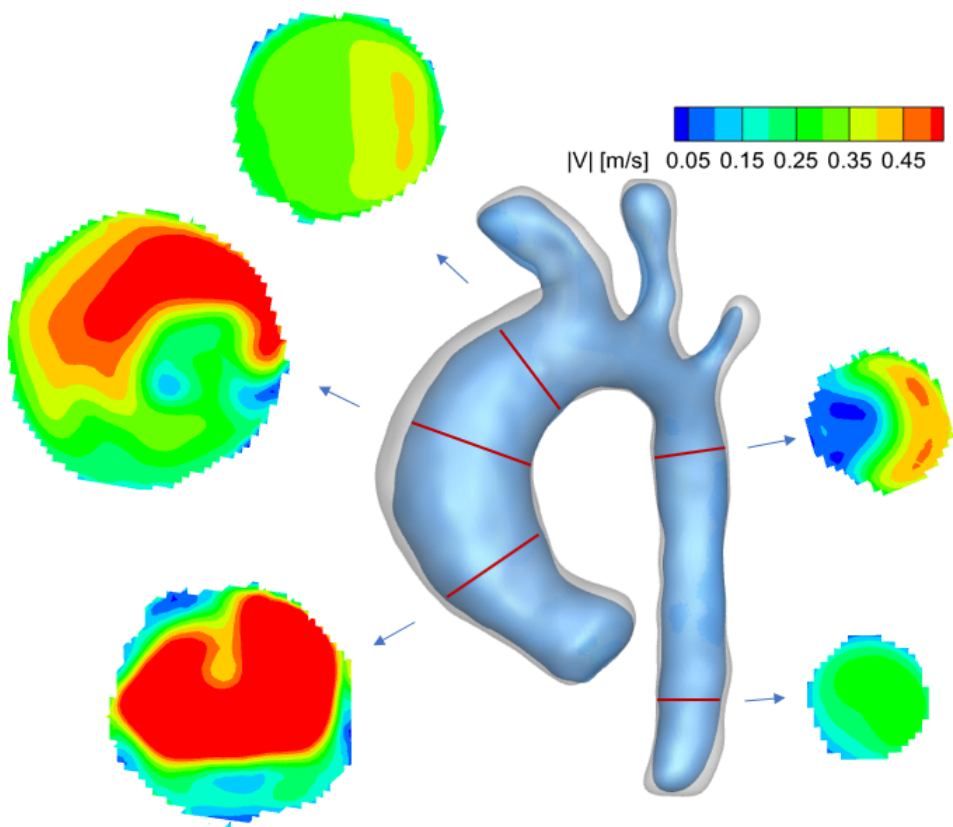


Figure 4.12: Contours of velocity magnitude in five cross-sections.

## APPENDIX E: WALL SHEAR STRESS AT FOUR KEY-FRAME

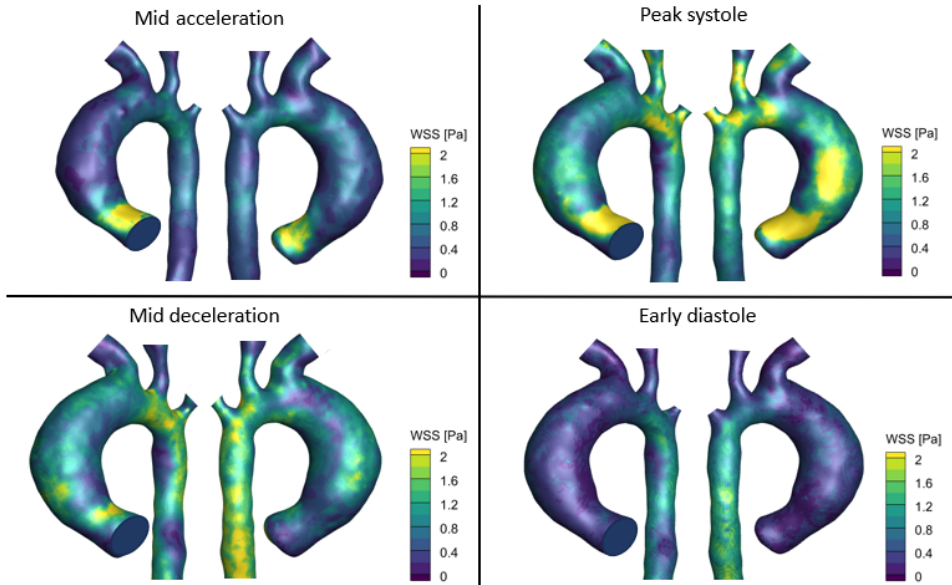


Figure 4.13: Wall shear stress of the aorta phantom at four key-frame (mid acceleration, peak systole, mid deceleration, and early diastole).

# REFERENCES

- [1] M. L. Brown, H. M. Burkhart, H. M. Connolly, *et al.*, “Coarctation of the aorta: Life-long surveillance is mandatory following surgical repair”, *Journal of the American College of Cardiology*, vol. 62, no. 11, pp. 1020–1025, 2013.
- [2] H. Jashari, A. Rydberg, P. Ibrahimi, G. Bajraktari, and M. Y. Henein, “Left ventricular response to pressure afterload in children: Aortic stenosis and coarctation: A systematic review of the current evidence”, *International Journal of Cardiology*, vol. 178, pp. 203–209, 2015.
- [3] G. Nigro, V. Russo, A. Rago, *et al.*, “Heterogeneity of ventricular repolarization in newborns with severe aortic coarctation”, *Pediatric Cardiology*, vol. 33, pp. 302–306, 2012.
- [4] C. Sinning, E. Zengin, R. Kozlik-Feldmann, *et al.*, “Bicuspid aortic valve and aortic coarctation in congenital heart disease—important aspects for treatment with focus on aortic vasculopathy”, *Cardiovascular Diagnosis and Therapy*, vol. 8, no. 6, p. 780, 2018.
- [5] A. Bocelli, S. Favilli, I. Pollini, *et al.*, “Prevalence and long-term predictors of left ventricular hypertrophy, late hypertension, and hypertensive response to exercise after successful aortic coarctation repair”, *Pediatric Cardiology*, vol. 34, no. 3, pp. 620–629, 2013.
- [6] A. D. Karaosmanoglu, R. D. A. Khawaja, M. R. Onur, and M. K. Kalra, “CT and MRI of aortic coarctation: Pre-and postsurgical findings”, *American Journal of Roentgenology*, vol. 204, no. 3, W224–W233, 2015.
- [7] S. Petersson, P. Dyverfeldt, and T. Ebbers, “Assessment of the accuracy of MRI wall shear stress estimation using numerical simulations”, *Journal of Magnetic Resonance Imaging*, vol. 36, no. 1, pp. 128–138, 2012.
- [8] A. F. Stalder, M. Russe, A. Frydrychowicz, J. Bock, J. Hennig, and M. Markl, “Quantitative 2D and 3D phase contrast MRI: Optimized analysis of blood flow and vessel wall parameters”, *Magnetic Resonance in Medicine*, vol. 60, no. 5, pp. 1218–1231, 2008.
- [9] N. Buchmann, C. Atkinson, M. Jeremy, and J. Soria, “Tomographic particle image velocimetry investigation of the flow in a modeled human carotid artery bifurcation”, *Experiments in Fluids*, vol. 50, pp. 1131–1151, 2011.
- [10] Z. Keshavarz-Motamed, J. Garcia, E. Gaillard, *et al.*, “Effect of coarctation of the aorta and bicuspid aortic valve on flow dynamics and turbulence in the aorta using particle image velocimetry”, *Experiments in Fluids*, vol. 55, pp. 1–16, 2014.

- [11] X. Wu, S. Gürzing, C. Schinkel, *et al.*, “Hemodynamic study of a patient-specific intracranial aneurysm: Comparative assessment of tomographic PIV, stereoscopic PIV, in vivo MRI and computational fluid dynamics”, *Cardiovascular Engineering and Technology*, pp. 1–15, 2021.
- [12] D. Lopes, H. Puga, J. C. Teixeira, and S. Teixeira, “Influence of arterial mechanical properties on carotid blood flow: Comparison of CFD and FSI studies”, *International Journal of Mechanical Sciences*, vol. 160, pp. 209–218, 2019.
- [13] M. Büsen, C. Arenz, M. Neidlin, *et al.*, “Development of an in vitro PIV setup for preliminary investigation of the effects of aortic compliance on flow patterns and hemodynamics”, *Cardiovascular Engineering and Technology*, vol. 8, pp. 368–377, 2017.
- [14] V. Deplano, Y. Knapp, E. Bertrand, and E. Gaillard, “Flow behaviour in an asymmetric compliant experimental model for abdominal aortic aneurysm”, *Journal of Biomechanics*, vol. 40, no. 11, pp. 2406–2413, 2007.
- [15] S. G. Yazdi, L. Huetter, P. D. Docherty, *et al.*, “A novel fabrication method for compliant silicone phantoms of arterial geometry for use in particle image velocimetry of haemodynamics”, *Applied Sciences*, vol. 9, no. 18, p. 3811, 2019.
- [16] P. Corso, U. Gülan, N. Cohrs, W. J. Stark, F. Duru, and M. Holzner, “Comprehensive in vitro study of the flow past two transcatheter aortic valves: Comparison with a severe stenotic case”, *Annals of biomedical engineering*, vol. 47, no. 11, pp. 2241–2257, 2019.
- [17] U. Gülan, H. Appa, P. Corso, *et al.*, “Performance analysis of the transcatheter aortic valve implantation on blood flow hemodynamics: An optical imaging-based in vitro study”, *Artificial organs*, vol. 43, no. 10, E282–E293, 2019.
- [18] D. Hasler and D. Obrist, “Three-dimensional flow structures past a bio-prosthetic valve in an in-vitro model of the aortic root”, *PloS one*, vol. 13, no. 3, e0194384, 2018.
- [19] D. Schanz, S. Gesemann, and A. Schröder, “Shake-the-box: Lagrangian particle tracking at high particle image densities”, *Experiments in Fluids*, vol. 57, pp. 1–27, 2016.
- [20] X. Wu, H. Saaid, J. Voorneveld, *et al.*, “4D flow patterns and relative pressure distribution in a left ventricle model by Shake-the-Box and proper orthogonal decomposition analysis”, *Cardiovascular Engineering and Technology*, vol. 14, no. 6, pp. 743–754, 2023.
- [21] H. Chen and L. P. Dasi, “An in-vitro study of the flow past a transcatheter aortic valve using time-resolved 3D particle tracking”, *Annals of Biomedical Engineering*, vol. 51, no. 7, pp. 1449–1460, 2023.
- [22] J. F. Juffermans, I. Nederend, P. J. van den Boogaard, *et al.*, “The effects of age at correction of aortic coarctation and recurrent obstruction on adolescent patients: MRI evaluation of wall shear stress and pulse wave velocity”, *European Radiology Experimental*, vol. 3, pp. 1–8, 2019.

- [23] R. M. Lang, B. P. Cholley, C. Korcarz, R. H. Marcus, and S. G. Shroff, "Measurement of regional elastic properties of the human aorta. a new application of transesophageal echocardiography with automated border detection and calibrated subclavian pulse tracings.", *Circulation*, vol. 90, no. 4, pp. 1875–1882, 1994.
- [24] D. Schanz, S. Gesemann, A. Schröder, B. Wieneke, and M. Novara, "Non-uniform optical transfer functions in particle imaging: Calibration and application to tomographic reconstruction", *Measurement Science and Technology*, vol. 24, no. 2, p. 024 009, 2012.
- [25] D. Schanz, A. Schröder, S. Gesemann, D. Michaelis, and B. Wieneke, "'Shake The Box': A highly efficient and accurate tomographic particle tracking velocimetry (TOMO-PTV) method using prediction of particle positions", in *PIV13; 10th International Symposium on Particle Image Velocimetry, Delft, The Netherlands, July 1-3, 2013*, Delft University of Technology, Faculty of Mechanical, Maritime, Material Engineering, and Faculty of Aerospace Engineering, 2013.
- [26] B. Wieneke, "Iterative reconstruction of volumetric particle distribution", *Measurement Science and Technology*, vol. 24, no. 2, p. 024 008, 2012.
- [27] A. Redheuil, W. C. Yu, C. O. Wu, *et al.*, "Reduced ascending aortic strain and distensibility: Earliest manifestations of vascular aging in humans", *Hypertension*, vol. 55, no. 2, pp. 319–326, 2010.
- [28] L. M. De Heer, R. P. Budde, W. P. T. M. Mali, A. M. de Vos, L. A. van Herwerden, and J. Kluin, "Aortic root dimension changes during systole and diastole: Evaluation with ecg-gated multidetector row computed tomography", *The International Journal of Cardiovascular Imaging*, vol. 27, pp. 1195–1204, 2011.
- [29] N. Grøndal, M. Bramsen, M. Thomsen, C. Rasmussen, and J. S. Lindholt, "The cardiac cycle is a major contributor to variability in size measurements of abdominal aortic aneurysms by ultrasound", *European Journal of Vascular and Endovascular Surgery*, vol. 43, no. 1, pp. 30–33, 2012.
- [30] M. N. Antonuccio, E. Gasparotti, F. Bardi, *et al.*, "Fabrication of deformable patient-specific AAA models by material casting techniques", *Frontiers in Cardiovascular Medicine*, vol. 10, 2023.
- [31] J. Lim, A.-R. Kim, S. Kim, *et al.*, "A new dip coating method using supporting liquid for forming uniformly thick layers on serpentine 3D substrates", *Advanced Materials Interfaces*, vol. 6, no. 24, p. 1 901 485, 2019.
- [32] S. Marconi, E. Lanzarone, G. H. van Bogerijen, *et al.*, "A compliant aortic model for in vitro simulations: Design and manufacturing process", *Medical Engineering & Physics*, vol. 59, pp. 21–29, 2018.
- [33] A. Moravia, S. Simoëns, M. El Hajem, *et al.*, "In vitro flow study in a compliant abdominal aorta phantom with a non-Newtonian blood-mimicking fluid", *Journal of Biomechanics*, vol. 130, p. 110 899, 2022.
- [34] S. G. Yazdi, P. D. Docherty, P. N. Williamson, *et al.*, "In vitro pulsatile flow study in compliant and rigid ascending aorta phantoms by stereo particle image velocimetry", *Medical Engineering & Physics*, vol. 96, pp. 81–90, 2021.

- [35] M. Bonfanti, G. Franzetti, S. Homer-Vanniasinkam, V. Díaz-Zuccarini, and S. Balabani, “A combined in vivo, in vitro, in silico approach for patient-specific haemodynamic studies of aortic dissection”, *Annals of Biomedical Engineering*, vol. 48, no. 12, pp. 2950–2964, 2020.
- [36] M. Y. Salmasi, S. Pirola, S. Sasidharan, *et al.*, “High wall shear stress can predict wall degradation in ascending aortic aneurysms: An integrated biomechanics study”, *Frontiers in Bioengineering and Biotechnology*, vol. 9, p. 750 656, 2021.
- [37] S. Schnell, D. A. Smith, A. J. Barker, *et al.*, “Altered aortic shape in bicuspid aortic valve relates influences blood flow patterns”, *European Journal of Echocardiography*, vol. 17, no. 11, pp. 1239–1247, 2016.
- [38] D. G. Cave, H. Panayiotou, and M. M. Bissell, “Hemodynamic profiles before and after surgery in bicuspid aortic valve disease—a systematic review of the literature”, *Frontiers in Cardiovascular Medicine*, vol. 8, p. 629 227, 2021.
- [39] J. Garcia, A. J. Barker, and M. Markl, “The role of imaging of flow patterns by 4D flow MRI in aortic stenosis”, *JACC: Cardiovascular Imaging*, vol. 12, no. 2, pp. 252–266, 2019.
- [40] T. H. Oechtering, M. M. Sieren, P. Hunold, *et al.*, “Time-resolved 3-dimensional magnetic resonance phase contrast imaging (4D flow MRI) reveals altered blood flow patterns in the ascending aorta of patients with valve-sparing aortic root replacement”, *The Journal of Thoracic and Cardiovascular Surgery*, vol. 159, no. 3, pp. 798–810, 2020.
- [41] K. Suwa, O. A. Rahman, E. Bollache, *et al.*, “Effect of aortic valve disease on 3D hemodynamics in patients with aortic dilation and trileaflet aortic valve morphology”, *Journal of Magnetic Resonance Imaging*, vol. 51, no. 2, pp. 481–491, 2020.
- [42] A. Guala, L. Dux-Santoy, G. Teixido-Tura, *et al.*, “Wall shear stress predicts aortic dilation in patients with bicuspid aortic valve”, *Cardiovascular Imaging*, vol. 15, no. 1, pp. 46–56, 2022.
- [43] P. F. Davies, “Hemodynamic shear stress and the endothelium in cardiovascular pathophysiology”, *Nature Clinical Practice Cardiovascular Medicine*, vol. 6, no. 1, pp. 16–26, 2009.
- [44] E. Faggiano, L. Antiga, G. Puppini, A. Quarteroni, G. B. Luciani, and C. Vergara, “Helical flows and asymmetry of blood jet in dilated ascending aorta with normally functioning bicuspid valve”, *Biomechanics and Modeling in Mechanobiology*, vol. 12, pp. 801–813, 2013.
- [45] A. J. Barker, M. Markl, J. Bürk, *et al.*, “Bicuspid aortic valve is associated with altered wall shear stress in the ascending aorta”, *Circulation: Cardiovascular Imaging*, vol. 5, no. 4, pp. 457–466, 2012.
- [46] J. Bock, A. Frydrychowicz, R. Lorenz, *et al.*, “In vivo noninvasive 4D pressure difference mapping in the human aorta: Phantom comparison and application in healthy volunteers and patients”, *Magnetic Resonance in Medicine*, vol. 66, no. 4, pp. 1079–1088, 2011.

- [47] K. Bouaou, I. Bargiotas, T. Dietenbeck, *et al.*, “Analysis of aortic pressure fields from 4D flow MRI in healthy volunteers: Associations with age and left ventricular remodeling”, *Journal of Magnetic Resonance Imaging*, vol. 50, no. 3, pp. 982–993, 2019.
- [48] J. Zimmermann, M. Loecher, F. O. Kolawole, *et al.*, “On the impact of vessel wall stiffness on quantitative flow dynamics in a synthetic model of the thoracic aorta”, *Scientific Reports*, vol. 11, no. 1, p. 6703, 2021.



# 5

## CONCLUSIONS AND OUTLOOK

### 5.1. CONCLUSIONS

Abnormal blood flow is closely associated with the formation and progression of cardiovascular diseases such as atherosclerosis, heart failure, and aneurysms. Blood flow visualization and analysis are critical for a better understanding of the underlying mechanism, as well as developing reliable flow-based biomarkers for the early diagnosis and treatment of cardiovascular diseases. However, a detailed and accurate blood flow analysis is still challenging due to the limitations in clinical imaging techniques such as their relatively low spatial and temporal resolution. Computational and experimental models have been developed to complement clinical techniques in blood flow assessment. Both modelling methods inevitably rely on simplifications and assumptions due to the difficulties in modelling the entirely physiological flow conditions, mechanical and geometric properties of the vessels, and the fluid properties of the blood. In this thesis, ***one of our research objectives is to overcome these difficulties in order to improve the fidelity of experimental blood flow modeling.***

Computational models and *in vitro* experimental models have great potential in providing patient-specific cardiovascular diseases interventions and management. Integrating clinical imaging, patient-specific CFD and *in vitro* models can reach a future of highly personalized medicine with surgical plan or treatment options tailored to the patients. Of course, there are still many steps before we finally arrive there. Continuous effort in advancing patient-specific cardiovascular flow modeling is necessary. For that reason, ***another objective of this thesis is to conduct patient-specific blood flow studies.***

In literature, many particle image-based techniques have been used to measure blood flow in *in vitro* experiments as a validation tool for numerical modeling and medical imaging, or as an alternative resource for studying relationships between lesions and blood flows. Most of these studies utilized 2D techniques conducting planar measurements, which is a simplification of the three-dimensional flow. Moreover, it cannot provide important information such as complete velocity gradient tensor and 3D distribution of wall shear stress. Therefore, ***our last research objective is to perform volumetric blood flow***

**measurements, offering an accurate and comprehensive estimation of hemodynamic metrics in a high-dimensional and high-resolution manner.** This was achieved by extending currently available advanced volumetric techniques to blood flow visualizations: multi-plane Stereo-PIV, Tomographic PIV, and Lagrangian particle tracking technique ‘Shake-the-Box’.

In **Chapter 2**, we developed a tomographic PIV (Tomo-PIV) setup, casted a rigid model of a patient-specific intracranial aneurysm, and built a steady flow controlling system. Tomo-PIV and multiplane Stereo-PIV measurements have been conducted. Stereo-PIV is a 2D technique but can be extended to 3D by performing multiple plane measurements. This is one of the methods to obtain 3D velocity data. Multiplane Stereo-PIV was compared to true volumetric techniques (Tomo-PIV, 4D-Flow MRI, and CFD). The multi-modality comparison results showed that the spatial resolution plays a major role in estimating the blood flow patterns, velocity, vorticity, and wall shear stress (WSS) magnitude. Due to its relatively low resolution, 4D-Flow MRI failed to capture the small-scale vortex structures in the core of the aneurysm, and gave a smaller value of velocity and WSS, especially the WSS magnitude was 2-4 times lower than CFD, Tomo-PIV, and Stereo-PIV estimations. The discrepancies were eliminated when down-sampling the CFD and PIV-based data to the same resolution as MRI. Stereo-PIV yielded lower WSS than Tomo-PIV, because of the 4 times lower spatial resolution in the depth direction than that of Tomo-PIV. Due to the planar measurements, the voxel sizes of the multiplane Stereo-PIV measurements in the depth dimension are constrained by the laser sheet thickness (1 mm), leading to pronounced averaging effects in the depth direction. Moreover, multiplane Stereo-PIV measurements and volume reconstruction are very time-consuming, especially for pulsatile flow investigation when multiple time-steps of volumetric data need to be reconstructed. Therefore, we concluded that the Tomo-PIV as an inherently 3D technique is a preferred method for the hemodynamic study compared to multiplane Stereo-PIV.

Even though Tomo-PIV has shown great potential in measuring complex blood flows, one of the limitations of Tomo-PIV is the amount of required processing time to resolve the velocity field from particle images. A novel 4D particle tracking velocimetry technique, the so-called Shake-the-Box (STB), was introduced in 2016 and has great improvements in the processing time (4-6 times faster than tomographic reconstruction) [1]. The key is that STB exploits the known flow information from the previous time steps to build an initial 3D particle distribution of the next time step, which greatly shortens the process time compared to reconstructing 3D particles at each time step like Tomo-PIV. There were also other advantages of STB, such as lower false reconstructed particles, higher position accuracy, and higher spatial resolution. Also, it has not been implemented in the bio-flow field. Therefore, in chapter 3, we were the first to introduce Shake-the-Box to *in vitro* blood flow measurement.

In **Chapter 3**, we applied the Shake-the-Box (STB) method to study the pulsatile flow in a realistic-shaped, dynamic left ventricle (LV) phantom with biological valves. The STB method resolved particles, particle tracks, 3D velocity fields, and pressure fields of the entire cardiac cycle. We observed a slight velocity magnitude difference (<5 %) between STB and Tomo-PIV results. However, because the velocity resolved from STB was particle-based instead of cross-relation based, STB provided higher spatial resolution

results than Tomo-PIV with the same particle images. Based on the velocity field, we estimated relative pressure through the use of the Poisson equation. Detailed spatial distribution of the relative pressure over the cardiac cycle was provided. In general, STB-resolved flow pattern, velocity, and pressure are in good agreement with those *in vivo* MRI studies from literature. Furthermore, the time-resolved, high-dimensional velocity data was decomposed into simpler datasets (spatial and temporal modes) by rapid Proper Orthogonal Decomposition (POD) analysis. The first six POD spatial modes (captured 95% of the kinetic energy) revealed the key features of the complex LV flow and provided a clear picture of different scales of vortices in the LV flow over the cardiac cycle. This highlights the potential of POD as an effective alternative for visualizing and analysing diverse-scale flow structures and their temporal behaviors in the LV. To summarize, this study illustrates that both Shake-the-Box and POD analysis are valuable tools for the accurate and efficient investigation of highly three-dimensional and time-varying cardiovascular flows. The novel features, such as particle tracks, 4D relative pressure field, and POD spatial/temporal modes, offer new insights into the LV flow and can also be used to validate for medical imaging software or CFD research.

So far, we have only focused on performing highly resolved blood flow *in vitro* measurements and analysis. However, another critical aspect of *in vitro* blood flow modeling is enhancing the bio-fidelity of the blood flow simulator. This involves incorporating realistic-shaped geometry, physiological wall properties, fluid properties, and pulsatile flow conditions. Therefore, in **Chapter 4**, we manufactured a transparent, compliant, and low-cost aorta phantom with patient-specific geometry using the brush-spin-heat coating method. We also created physiological flow conditions with a left ventricle assistant device and driving system. Finally, we conducted flow measurements using the STB technique. Based on the STB measurements, aortic flow information (particle tracks, velocity, WSS, and its time-derivatives), as well as wall movement (strain, strain rate, distensibility) were analysed. Our results showed that the mechanical properties of the phantom, such as wall thickness and Young's modulus, are well controlled and are within the physiological range of the human aorta. The wall movements were quantified by strain (maximum 5.4 mm), strain rate (42%), and distensibility ( $9.9 \times 10^{-3} \text{ mmHg}^{-1}$ ). They also closely matched with the ones reported in studies based on MRI measurements. We provided flow information which includes: particle tracks, flow patterns, peak WSS, time-averaged wall shear stress (TAWSS), and oscillatory shear index (OSI). These flow information aligned with *in vivo* patient-specific MRI measurements, as well as with previously reported similar cases. In summary, this work illustrated the feasibility of manufacturing a compliant patient-specific artery phantom that not only mimics the mechanical behavior of blood vessels but is also suitable for advanced optical flow measurements. This can increase the availability of high-fidelity experimental cardiovascular flow data.

## 5.2. FUTURE OPPORTUNITIES

### 5.2.1. NON-NEWTONIAN BLOOD ANALOGUES FOR *In vitro* BLOOD FLOW MODELING

Blood is known to be a non-Newtonian fluid exhibiting shear-thinning effect. However, studies have shown that it is generally accepted that the non-Newtonian effect of blood flow is not significant at where the shear rate is higher than  $100 \text{ s}^{-1}$  [2]. In most arteries, blood is normally exposed to high shear rates and appears as a homogeneous continuum medium. Hence, some studies found that the differences between the Newtonian and non-Newtonian flow in large vessels were not statistically significant, therefore Newtonian blood model can be a good approximation [3]–[5]. However, the shear rate can be low at the diastole phase and at regions of stenosis or bifurcation where flow became stagnated or recirculated [6]. Blood becomes much more viscous than in high shear-rate flows [7]. Therefore, taking the shear-thinning into consideration allows a more accurate analysis of hemodynamic characteristics.

Some experimental studies have been developing non-Newtonian blood analogues for optical *in vitro* imaging flow measurements [6], [8]. A mixture of water/glycerol with a ratio of approximately 60/40 (by weight) was typically adopted as Newtonian working fluid in PIV experiments. However, this recipe leads to a 3 times higher viscosity than blood. By adding a third component such as Urea and NaI, the three-component Newtonian fluid can mimic the density and viscosity of blood quite well. Non-Newtonian behavior can be introduced to this three-component Newtonian fluid by adding a small percentage (0.04-0.06% by weight) of Xanthan gum [8]. Therefore, mimicking the non-Newtonian effect of blood for *in vitro* optical flow measurements is possible. Future studies are recommended to integrate this important property of blood into experiments.

### 5.2.2. APPLY POD IN MULTIMODALITY STUDY, NEW BIOMARKERS DEVELOPMENT, AND REDUCED ORDER MODELING

As we showed in Chapter 4 of this thesis, Proper Orthogonal Decomposition (POD) analysis is computationally fast and complexity-reduced. It provides the dominant flow features of the entire time-resolved 3D data in a few linear spatial modes. Therefore, direct comparison of these dominant flow features from different datasets can be easily compared. Especially for comparing datasets from different modalities, POD has a big advantage of free from imaging registration (i.e. scaling, coordinates translation, etc.).

We also think that POD-based metrics can be explored as potential new biomarkers. Considering the POD modes are sorted by the percentage of kinetic energy they carry, and the dominant flow features of healthy and patient-specific cases can carry different amounts of energy, a specific threshold of the POD modes energy contribution can be developed for assisting diagnosis. For instance, it was reported in ascending aorta with a normal and dysfunctional bileaflet mechanical aortic valve, the corresponding energetic contributions of the 1st POD mode is approximately 74% and 60%, respectively [9]. The successful building of the POD mode energy content as biomarker of course relies on a large-scale patient cases analysis. However, the rapid characteristic of POD makes this goal very promising.

Full order models (FOMs), such as Finite Element and Finite Volume methods, are

commonly used for resolving blood flow dynamics numerically. However, FOMs are computationally very expensive and have a large degree of freedom. The data-driven reduced order models (ROMs) can enable fast but accurate computation of hemodynamic parameters. POD can offer sufficient yet small data basis for reduced order modeling. Combined with artificial neural networks (ANNs), hemodynamic parameters (velocity, wall shear stress, pressure) can be predicted in a fast and reliable way. Sino et al [10], [11] have demonstrated the great potential of the POD-ANN method by applying it in patient-specific coronary artery hemodynamic studies.

### 5.2.3. APPLICATION OF *In vitro* COMPLIANT ARTERIAL MODELING

*In vitro* blood vessel modeling was widely based on rigid walls, which limits its application mainly to blood flow analysis. As we showed in Chapter 4, the availability of transparent compliant arterial modeling in the laboratory opens opportunities for new applications. Apart from patient-specific hemodynamic analysis, other applications include: modeling surgical treatments (e.g. aneurysm clip-treatment, stent placement), medical device testing (e.g. stents or artificial heart valves), modeling fluid-structure interaction, and validating advanced numerical models and clinical imaging techniques.

### 5.2.4. MACHINE LEARNING FOR BLOOD FLOW MODELING

With the increasing availability of *in vitro*, *in silico*, and *in vivo* blood flow data, one of the interesting directions of blood flow modeling is machine learning (ML). A well-trained ML model is featured with its fast predictive capabilities. Theoretically, with sufficient amount of training data, ML models can learn the mapping between the input and output parameters. Therefore, ML models that have been trained with MRI and CFD hemodynamic data could predict blood flow, such as velocity, pressure, and shear stress [12]–[14]. However, there are still many challenges for machine learning replacing traditional computational physics-based models, especially in patient-specific applications. The large variability in patient-specific geometries, boundary conditions, and mechanical properties makes the generalization of input for ML models challenging. Moreover, learning from high-dimensional data and producing high-dimensional output data remains very challenging. But machine learning models can serve as a tool to enhance *in vitro/in silico* blood flow modeling by its great potential in medical image segmentation [15], image processing [16], uncertainty quantification [17], and interpretation of complex high spatiotemporal datasets [18]. For instance, we can use trained ML models to reduce the level of input uncertainties for image-based CFD simulations and *in vitro* experiments by effective and efficient ML image segmentation and ML denoising MRI flow data.

### 5.3. OUTLOOK

Despite the established connections between hemodynamics and cardiovascular diseases, the clinical translation of hemodynamics still faces some obstacles. Realizing the potential of hemodynamics in personalized medicine requires the development of precise, swift, and easily accessible patient-specific modeling and analysis, alongside the establishment of reliable biomarker thresholds and user-friendly flow visualization software. Achieving fast, accurate and patient-specific blood flow modeling relies on the continuous advancement of technologies in each modality, including medical imaging, CFD modeling, and *in vitro* modeling. In the meantime, the integration of these techniques is an important way of acquiring a comprehensive and detailed blood flow quantification, helping extend hemodynamic analysis to various other applications (e.g. provide insights into disease mechanisms, develop biomarkers, optimize medical device). Furthermore, more attention should be paid on exploring methods for easier and faster blood flow analysis, facilitating the clinical translation of hemodynamics. We would also like to point out that effective collaboration and good understanding among physicians, engineers, patients, and software developers are critical to realize the clinical use of hemodynamics. The availability of clinical database on physiological parameters and the consent of data usage from patients can lay a good foundation for the development of CFD and *in vitro* patient-specific modeling.

# REFERENCES

- [1] D. Schanz, S. Gesemann, and A. Schröder, “Shake-the-box: Lagrangian particle tracking at high particle image densities”, *Experiments in Fluids*, vol. 57, pp. 1–27, 2016.
- [2] F. J. Gijsen, F. N. van de Vosse, and J. Janssen, “The influence of the non-Newtonian properties of blood on the flow in large arteries: Steady flow in a carotid bifurcation model”, *Journal of Biomechanics*, vol. 32, no. 6, pp. 601–608, 1999.
- [3] K. Perktold, R. Peter, and M. Resch, “Pulsatile non-Newtonian blood flow simulation through a bifurcation with an aneurysm”, *Biorheology*, vol. 26, no. 6, pp. 1011–1030, 1989.
- [4] B. M. Johnston, P. R. Johnston, S. Corney, and D. Kilpatrick, “Non-Newtonian blood flow in human right coronary arteries: Transient simulations”, *Journal of Biomechanics*, vol. 39, no. 6, pp. 1116–1128, 2006.
- [5] U. Y. Lee, J. Jung, H. S. Kwak, *et al.*, “Patient-specific computational fluid dynamics in ruptured posterior communicating aneurysms using measured non-Newtonian viscosity: A preliminary study”, *Journal of Korean Neurosurgical Society*, vol. 62, no. 2, pp. 183–192, 2019.
- [6] V. Deplano, Y. Knapp, L. Bailly, and E. Bertrand, “Flow of a blood analogue fluid in a compliant abdominal aortic aneurysm model: Experimental modelling”, *Journal of Biomechanics*, vol. 47, no. 6, pp. 1262–1269, 2014.
- [7] O. K. Baskurt, M. R. Hardeman, and M. W. Rampling, *Handbook of hemorheology and hemodynamics*. IOS press, 2007, vol. 69.
- [8] M. C. Brindise, M. M. Busse, and P. P. Vlachos, “Density-and viscosity-matched Newtonian and non-Newtonian blood-analog solutions with PDMS refractive index”, *Experiments in Fluids*, vol. 59, pp. 1–8, 2018.
- [9] A. Darwish, G. Di Labbio, W. Saleh, and L. Kadem, “Proper orthogonal decomposition analysis of the flow downstream of a dysfunctional bileaflet mechanical aortic valve”, *Cardiovascular Engineering and Technology*, vol. 12, pp. 286–299, 2021.
- [10] P. Siena, M. Girfoglio, and G. Rozza, “Fast and accurate numerical simulations for the study of coronary artery bypass grafts by artificial neural networks”, in *Reduced Order Models for the Biomechanics of Living Organs*, Elsevier, 2023, pp. 167–183.
- [11] P. Siena, M. Girfoglio, F. Ballarin, and G. Rozza, “Data-driven reduced order modelling for patient-specific hemodynamics of coronary artery bypass grafts with physical and geometrical parameters”, *Journal of Scientific Computing*, vol. 94, no. 2, p. 38, 2023.

- [12] L. Liang, M. Liu, C. Martin, and W. Sun, “A deep learning approach to estimate stress distribution: A fast and accurate surrogate of finite-element analysis”, *Journal of The Royal Society Interface*, vol. 15, no. 138, p. 20 170 844, 2018.
- [13] G. Kissas, Y. Yang, E. Hwuang, W. R. Witschey, J. A. Detre, and P. Perdikaris, “Machine learning in cardiovascular flows modeling: Predicting arterial blood pressure from non-invasive 4D flow MRI data using physics-informed neural networks”, *Computer Methods in Applied Mechanics and Engineering*, vol. 358, p. 112 623, 2020.
- [14] G. Li, H. Wang, M. Zhang, *et al.*, “Prediction of 3D cardiovascular hemodynamics before and after coronary artery bypass surgery via deep learning”, *Communications Biology*, vol. 4, no. 1, p. 99, 2021.
- [15] J. A. Onofrey, L. H. Staib, X. Huang, *et al.*, “Sparse data-driven learning for effective and efficient biomedical image segmentation”, *Annual Review of Biomedical Engineering*, vol. 22, pp. 127–153, 2020.
- [16] H. Gao, L. Sun, and J.-X. Wang, “Super-resolution and denoising of fluid flow using physics-informed convolutional neural networks without high-resolution labels”, *Physics of Fluids*, vol. 33, no. 7, 2021.
- [17] C. M. Fleeter, G. Geraci, D. E. Schiavazzi, A. M. Kahn, and A. L. Marsden, “Multilevel and multifidelity uncertainty quantification for cardiovascular hemodynamics”, *Computer Methods in Applied Mechanics and Engineering*, vol. 365, p. 113 030, 2020.
- [18] T. B. Le, “Dynamic modes of inflow jet in brain aneurysms”, *Journal of Biomechanics*, vol. 116, p. 110 238, 2021.

# ACKNOWLEDGEMENTS

I would like to address my gratitude to the people who supported me during my PhD journey. First of all, **Sasa** and **Hildo**, thank you for being my promoters and giving me the opportunity to work on this interesting topic. **Sasa**, I appreciate all the meetings and discussions. You were always very enthusiastic and encouraging. Without your pushing, the last chapter of my thesis would be less fulfilling. Supervising students together was nice and I learned a lot from it. **Hildo**, thank you for being at the important moments of my PhD. It is a pity that I didn't manage to perform the *in vitro* MRI measurements. It would have been a very exciting experience.

During the years of my PhD, I worked mainly in the lab at the Transport Phenomena (TP) group. Firstly, I would like to extend my special gratitude to our technicians from the TP group. **Christiaan**, the success of my experiments would not have been possible without your proficient technical and practical support. You were always there to help – building setups, troubleshooting, and solving problems. You are also a good friend who I could talk to about many things. I really enjoyed our coffee breaks, the conference in Munich, and the Queen cover performance together. **Duco**, thank you for finding a nice solution of the heating sources for curing my compliant aorta model. Also, together with Christiaan, you made the ancient but critical equipment – the VAD driving system run again!

Thank my (pre-Covid) office mates **Manu**, **Sid**, and **Peng** for making the daily work environment nice, fun and safe. **Manu**, you were always there to answer all my beginner questions, sharing useful tips. We had many laughs. I also appreciated your honesty and directness. **Sid**, your relaxed and artistic vibe has made the intense PhD work much more soothing. I always liked it when you showing me your latest art creation. **Peng**, I appreciate you sharing your PhD experience openly and patiently. My (after-Covid) office mates **Aza**, **Christel**, **Yanyan**, **Andrey** and **Sacha**, thank you for creating a quiet and friendly atmosphere in the office. **Aza**, it was always fun talking about the PhD pressure with you, which reminds me a lot about my first year. Your generously sharing snacks with me gave me extra energy for working late in the afternoon. **Christel**, the office was more lively whenever you were there. You were also the person who knew how to offer the most comforting support. **Yanyan**, I enjoyed our hiking weekends and our trip together to Porto and Lisbon.

**Elin**, You were a very nice, supportive, helpful and responsive colleague and friend. Thanks for organizing all kinds of TP activities, making the PhD life more colorful. I also enjoyed our hotpot meals and the many talks we had. **Annekatrien**, I enjoyed our chats and the cakes you baked. **Fei**, thank you for the discussions we had about my topic and career choices. **Lorenz**, I always enjoyed our little chats about cats. Thank you for trying to help in the lab now and then. It was very nice chatting to you at Christiaan's house warming party. **Romana**, as a mountain lover, I really enjoyed hearing your travel and hiking stories. I also had good laughs with you about Kris's funny anecdotes and my

triplets students. **Jorrit**, you are always kind and sociable. Thank you for the fun and friendly atmosphere you brought. **Darry**, during lunch, we had many discussions about the PhD topics and the life in the Netherlands as a foreigner. Thanks for your accompanies and all your help. **Justin**, you always surprise me with small treats. Thank you! I enjoyed the Schlaf und Nerven Tee. **Matheus**, you have a way to tune the complains into humor, making them enjoyable to listen to. **Vojtech**, the second INTJ in TP, your laughs always lighten me up. **Yufan**, thank you for teaching me bouldering skills. The Chinese New celebration party was great! **Aiyu, Artem, Manas, Iman, Ruipeng, and the rest of TP members**, thank you all for making TP a nice group to be part of.

During my PhD, I have worked together with a couple of great students. It was a lot of fun to supervise ‘**the triplets**’ **Jonas, Jesper** and **Sweder**. **Aron**, nicely done for finding a new VAD for our experiments. It is a very important contribution. **Stefenie, Stijn, Diederik, Magda**, it was a pleasure to work with you.

From Leiden University Medical Center side, **Joe** and **Paul**, thank you for providing me the geometry and MRI measurements of the aorta patient.

Lastly, I want to thank my dear family and friends. **Ji Xun**, without your help, the journey to the Netherlands would be very difficult. **Rense**, I am so glad to have you as a nice friend during the first year of my PhD. I had many new and fun experiences with our small four person group. It was very memorable! **Xuan** and **Josh**, the talks about psychology was very interesting and inspiring. I liked our hiking in the Black forest together. **Xuan**, with you, I enjoyed many fun activities like skiing, bouldering, paddling, hiking, picking oysters. Thank **all my Friends who I met in the gym, Zumba dance and skiing club** for the funny, pleasant moments which energized me greatly. **Bouke**, thank you for always have faith on me finishing my PhD, and thank you for all the support you have provided throughout the years. Thanks the **Kaaks** family for welcoming me to the family. **Arjan** and **Ligia**, thank you for helping or offering your help on many occasions, and I am very grateful for all the beautiful trips. Thank my cousin **Ting** for the special friendship, her understanding, support and encouragement. Thank **my father**, his full acceptance of whom I am, his incredible patience, and continuous support have been the source of my strength.

# CURRICULUM VITÆ

## Xiaolin Wu

26-05-1991      Born in Hunan, China.

### EDUCATION

1996–2003      Primary School  
Hunan, China

2003–2010      Junior and Senior High School  
Hunan, China

2010–2015      Bachelor in Chemical Engineering and Machinery  
Faculty of Chemical Engineering, Dalian University of Technology  
Dalian, China

2016–2018      Master of Science in Safety Engineering  
Faculty of Chemical Engineering, Dalian University of Technology  
Dalian, China  
*Thesis:*          Numerical Simulation of Fluid-thermal-structural  
Coupling in a Submerged Combustion Vaporizer  
*Supervisor:*    Dr. Jintao Wu

2018–2024      Ph.D. candidate  
Faculty of Applied Sciences, Delft University of Technology  
Delft, The Netherlands  
*Thesis:*          Patient-specific Cardiovascular Flows Using Particle  
Image-based Velocimetry  
*Promotor(s):*   Prof. dr. Sasa Kenjeres, Dipl.-Ing. and Prof. dr. Hildo  
J. Lamb, MD (LUMC)



# LIST OF PUBLICATIONS

3. **X. Wu**, M. B. K. Jasen, J. J. Westenberg, J. H. Lamb, S. Kenjereš, *Aortic Strain, Flow Pattern and Wall Shear Stress in a Patient-specific Compliant Aorta Replica Using 4D Particle Tracking Velocimetry*, Medical Engineering and Physics, Under review, (2024).
2. **X. Wu**, H. Saaid, J. Voorneveld, T. Claessens, J. J. Westenberg, N. de Jong, G. J. Bosch, S. Kenjereš. *4D Flow Patterns and Relative Pressure Distribution in a Left Ventricle Model by Shake-the-Box and Proper Orthogonal Decomposition Analysis*, Cardiovascular Engineering and Technology, 14(6), pp. 743-754, (2023).
1. **X. Wu**, S. Gürzing, C. Schinkel, M. Toussaint, R. Perinajová, P. van Ooij, S. Kenjereš, *Hemodynamic Study of a Patient-Specific Intracranial Aneurysm: Comparative Assessment of Tomographic PIV, Stereoscopic PIV, In Vivo MRI and Computational Fluid Dynamics*, Cardiovascular Engineering and Technology, pp. 1-15, (2021).

